

ELECTRIC FIELD-INDUCED CONDUCTIVITY SWITCHING IN
VANADIUM SESQUIOXIDE NANOSTRUCTURES

A DISSERTATION

SUBMITTED TO THE DEPARTMENT OF APPLIED PHYSICS

AND THE COMMITTEE ON GRADUATE STUDIES

OF STANFORD UNIVERSITY

IN PARTIAL FULFILLMENT OF THE REQUIREMENTS

FOR THE DEGREE OF

DOCTOR OF PHILOSOPHY

Justin Brockman

June 2012

© 2012 by Justin Samuel Brockman. All Rights Reserved.
Re-distributed by Stanford University under license with the author.



This work is licensed under a Creative Commons Attribution-Noncommercial 3.0 United States License.

<http://creativecommons.org/licenses/by-nc/3.0/us/>

This dissertation is online at: <http://purl.stanford.edu/fn562jc3318>

I certify that I have read this dissertation and that, in my opinion, it is fully adequate in scope and quality as a dissertation for the degree of Doctor of Philosophy.

Stuart Parkin, Primary Adviser

I certify that I have read this dissertation and that, in my opinion, it is fully adequate in scope and quality as a dissertation for the degree of Doctor of Philosophy.

James Harris, Co-Adviser

I certify that I have read this dissertation and that, in my opinion, it is fully adequate in scope and quality as a dissertation for the degree of Doctor of Philosophy.

David Goldhaber-Gordon

Approved for the Stanford University Committee on Graduate Studies.

Patricia J. Gumport, Vice Provost Graduate Education

This signature page was generated electronically upon submission of this dissertation in electronic format. An original signed hard copy of the signature page is on file in University Archives.

Abstract

Strong interactions, or correlations, between the *d* or *f* electrons in transition metal oxides can lead to various types of metal-insulator transitions which may be triggered by external parameters such as temperature, pressure, doping and magnetic field. Recent theoretical and experimental reports have suggested that this transition can also be triggered by a threshold electric field. Fully realized, this effect could lead to an entirely new class of electronic switches based on materials with strongly correlated electron systems. However, significant questions remain about the detailed nature of the experimental results, especially the degree to which Joule heating plays a role.

In this work, we present an investigation of time-resolved, voltage-induced conductivity switching in the canonical metal-insulator transition system V_2O_3 . The main findings can be categorized into three parts: film growth, electrical measurement, and electro-thermal modeling. First we discuss the growth, optimization and characterization of high-quality epitaxial V_2O_3 films, including the effect of oxygen pressure, substrate temperature and substrate material on the film properties. Next we show experimental results on electric field-induced phase transitions in V_2O_3 nanostructures fabricated by electron beam lithography. We observe that a threshold electric field of approximately 10^7 V/m applied across two-terminal nanostructures causes a metallization of V_2O_3 's low-temperature Mott insulating state, preceded by a nanosecond-scale delay time. Lastly, we explore the feasibility of Joule heating as an explanation for the switching process. After fully accounting for temperature-related feedback and subthreshold nonlinear current-voltage characteristics, we find remarkably good agreement between the predicted and observed threshold voltages and switching delay times as a function of temperature, suggesting the switching mechanism is thermal in origin. We believe these findings have important implications for recent reports of voltage-induced switching in the related materials VO_2 and Fe_3O_4 and will also help to guide future research on this phenomenon.

Acknowledgements

This work would not be possible without the contributions of many amazing people. First and foremost, I would like to thank my primary research advisor Stuart Parkin for welcoming me into his team at the IBM Almaden Research Center. I am endlessly inspired by his genius, creativity, and unrelenting passion for discovery. I am also deeply indebted to my Stanford-based advisor James Harris for many years of patient guidance and support, and for originally suggesting the wonderful idea of carrying out my PhD research at IBM.

Mahesh Samant, Kevin Roche, and many members of the IBM Machine shop, especially Chris Lada and Robert Erickson, were responsible for designing, installing, programming, and maintaining the powerful deposition tools I had the privilege of using throughout this work.

Brian Hughes, Charles Rettner, and Rai Moriya deserve special acknowledgement for the fabrication of my films into switchable nanostructures, and Li Gao was instrumental in helping me with high-frequency electrical measurements of these devices. I would also like to thank Naga Phani Aetukuri, with whom I shared an office, a friendship, and many helpful discussions for more than half a decade. Other group members at IBM to whom I am extremely grateful for mentorship and/or direct contributions to this work include Xin Jiang, See-Hun Yang, Luc Thomas, Cheng-Han Yang, Ruisheng Liu, Aakash Pushp, Jae-Woo Jeong, Guenole Jan, Bastiaan Bergman, and Masamitsu Hayashi.

Thanks also go to Andrew Kellock for Rutherford backscattering analysis, and Teya Topuria and Leslie Krupp for transmission electron microscopy. Arturas Vailionis provided excellent training and assistance with the Stanford X-ray diffraction equipment.

I am also indebted to Prof. David Goldhaber-Gordon for serving on my reading committee, Prof. Ian Fisher for acting as an examiner during my thesis defense, and Prof. Paul McIntyre for chairing my defense. Paula Perron, Claire Nicholas, Yvonne Paxton, and Gail Chun-Creech provided invaluable administrative support.

Finally, I would like to thank my parents, my siblings, and all my friends for their patience, support and understanding over the years.

Table of Contents

| | |
|--|------|
| Abstract | v |
| Acknowledgments..... | vii |
| Table of Contents..... | ix |
| List of Figures | xiii |
| List of Tables | xxiv |
| | |
| Chapter 1: INTRODUCTION..... | 1 |
| 1.1 Motivation..... | 2 |
| 1.2 Overview of Work | 6 |
| 1.3 Dissertation Structure..... | 8 |
| | |
| Chapter 2: BACKGROUND..... | 11 |
| 2.1 Introduction..... | 12 |
| 2.2 Metal-Insulator Transitions..... | 12 |
| 2.2.1 The Hubbard Model..... | 12 |
| 2.2.2 Two Routes across the Metal-Insulator Transition..... | 13 |
| 2.2.3 Mott-Hubbard versus Charge-Transfer Insulators..... | 15 |
| 2.3 Field-Effect Switching in Correlated Insulators | 17 |
| 2.4 Introduction to V_2O_3 | 18 |
| 2.4.1 Phase Diagram | 18 |
| 2.4.2 Crystal Structure..... | 20 |
| 2.4.3 Band Structure | 21 |
| 2.4.4 Other Phases of Vanadium Oxide | 23 |
| 2.5 Notes on High-Field Transport in Insulators | 24 |
| 2.5.1 Dielectric Breakdown | 24 |
| 2.5.2 Poole-Frenkel and Schottky Emission..... | 25 |
| | |
| Chapter 3: EXPERIMENTAL PROCEDURES | 29 |
| 3.1 Introduction..... | 30 |

| | | |
|---|--|----|
| 3.2 | Film Deposition | 30 |
| 3.3 | Film Characterization..... | 33 |
| 3.3.1 | XRD..... | 33 |
| 3.3.2 | RBS..... | 34 |
| 3.3.3 | RHEED, TEM and AFM | 35 |
| 3.3.4 | XPS | 36 |
| 3.3.5 | Four-Point Resistivity Measurements..... | 37 |
| 3.4 | Device Fabrication | 38 |
| 3.4.1 | Mesa Structure Level | 41 |
| 3.4.2 | Isolation Pad Level | 41 |
| 3.4.3 | Nanogap Level..... | 42 |
| 3.4.4 | Contact Pad Level..... | 42 |
| 3.4.5 | Completed Structures..... | 43 |
| 3.5 | Device Testing | 45 |
| Chapter 4: THIN FILM GROWTH OF V_2O_3 ON UNANNEALED α - Al_2O_3 (0001) | | 47 |
| 4.1 | Introduction..... | 48 |
| 4.2 | Materials and Methods..... | 48 |
| 4.2.1 | Substrate Selection..... | 48 |
| 4.2.2 | Substrate Preparation | 50 |
| 4.2.3 | Growth Procedure | 50 |
| 4.3 | Optimal Film Properties..... | 51 |
| 4.3.1 | Electrical Characterization | 51 |
| 4.3.2 | Structural Characterization (RHEED, AFM, XRD, TEM) | 52 |
| 4.3.3 | Chemical Characterization (RBS, XPS) | 55 |
| 4.4 | Growth Temperature Dependence | 58 |
| 4.5 | Oxygen Pressure Dependence..... | 59 |
| 4.6 | Thickness Dependence..... | 64 |
| 4.7 | Summary | 64 |
| Chapter 5: GROWTH OF V_2O_3 ON OTHER SUBSTRATES..... | | 65 |

| | | |
|---|---|-----|
| 5.1 | Introduction..... | 66 |
| 5.2 | Growth on Annealed Sapphire(0001) | 66 |
| 5.3 | Growth on Unannealed Sapphire($11\bar{2}0$) | 74 |
| 5.4 | Growth on Annealed LiTaO ₃ (0001) | 78 |
| 5.5 | Growth on Cr ₂ O ₃ -Buffered Sapphire(0001) | 82 |
| 5.6 | Summary | 86 |
| Chapter 6: FIELD-EFFECT SWITCHING OF V ₂ O ₃ NANOSTRUCTURES | | 87 |
| 6.1 | Introduction..... | 88 |
| 6.2 | Experimental Setup..... | 88 |
| 6.3 | Direct-Current Switching..... | 90 |
| 6.3.1 | $V < V_{Th}$: Nonlinear Conduction | 95 |
| 6.3.2 | $V \sim V_{Th}$: Voltage-Controlled Oscillations | 97 |
| 6.3.3 | $V < V_{Th}$: Filamentary Behavior..... | 101 |
| 6.4 | High-Speed Switching | 102 |
| 6.5 | Summary | 104 |
| Chapter 7: THERMAL MODELING AND COMPARISON TO EXPERIMENT | | 105 |
| 7.1 | Introduction..... | 106 |
| 7.2 | The Failure of a Simple Model | 106 |
| 7.3 | Incorporating Feedback and Heat Dissipation..... | 109 |
| 7.4 | Results..... | 113 |
| 7.5 | Summary | 116 |
| Chapter 8: CONCLUSIONS AND SUGGESTIONS FOR FURTHER RESEARCH..... | | 117 |
| 8.1 | Conclusions..... | 118 |
| 8.2 | Suggestion for Future Research..... | 119 |
| Appendix A: LIST OF ABBREVIATIONS..... | | 130 |
| Appendix B: SAMPLE NUMBER REFERENCE | | 131 |

List of Figures

Chapter 1: Introduction

- Fig. 1.1 A simple picture of the gridlocked electrons in a Mott insulator. At an integer filling of electrons per site, conduction is blocked by the Coulomb repulsion energy U that must be provided for two electrons to occupy the same site.3
- Fig. 1.2 A generalized spectrum of condensed matter systems, sorted by degree of electron localization. Strongly correlated materials lie in the fertile middle ground between systems with mostly-free electrons and systems with tightly-bound electrons, and they are host to a number of materials with exotic and technologically useful properties.4
- Fig. 1.3 The conventional experimental setup for studying two-terminal electric field-induced switching in correlated insulators. (a) A circuit diagram showing a correlated insulator sandwiched between two electrodes under an applied bias, and (b) a typical I-V curve showing that a threshold voltage will cause the device to switch into a high-conductance state. Upon removal of the bias, the material reversibly returns to the insulating state with no memory effect.7

Chapter 2: Background

- Fig. 2.1 Reproduced from Ref[4], the phase diagram of a Mott-Hubbard system as a function of electron filling and U/W . Two routes of transitioning across the metal-insulator boundary are depicted. The metallic state in the shaded region is highly sensitive to disorder-induced localization.14
- Fig. 2.2 Adapted from Ref[4], energy level diagrams for the two different kinds of Mott insulators. The splitting energy U generated by the on-site coulomb repulsion can split the d-band in two distinct ways with respect to the p bands.15
- Fig. 2.3 Reproduced from Ref[40], the classic Zaanen-Sawatzky-Allen phase diagram plotting the boundary between CT-type and MH-type correlated

| | |
|---|----|
| insulators. The values of U and Δ are deduced from a combination of XPS and EELS data. | 16 |
| Fig. 2.4 Reproduced from Ref[36], the metal-insulator transition phase diagram of V_2O_3 showing the influence of temperature, pressure, and Cr and Ti doping on the MIT. The closed and open symbols are for increasing and decreasing pressure or temperature. | 19 |
| Fig. 2.5 Crystal structure diagrams for V_2O_3 . (a) The corundum unit cell of the high-temperature metallic V_2O_3 phase. (b) A topview along the c-axis showing 1 monolayer of vanadium and oxygen atoms. (c) A simplified sideview showing how two-thirds of the oxygen octahedra are occupied with vanadium atoms. | 21 |
| Fig. 2.6 Two competing energy level schematics for V_2O_3 . (a) A prediction of degenerate e_g orbitals reproduced from references[67-69]. (b) An empirically determined prediction of a_{1g} and e_g hybridization reproduced from reference[72]. | 22 |
| Fig. 2.7 Reproduced from Ref[77], the stoichiometric phase diagram of the various vanadium oxides. V_2O_3 is one of the lowest oxidation state phases, apart from VO and $V_{13}O_{16}$ | 24 |
| Fig. 2.8 A figure, reproduced from Ref[80], showing three different mechanisms of high-field conduction in an insulator: Poole-Frenkel emission, phonon-assisted tunneling, and direct tunneling. | 26 |
| Fig. 2.9 A comparison of the Poole-Frenkel and Schottky emission phenomena. In both cases, the energy barrier responsible for blocking conduction is lowered by a factor proportional to the square root of the applied electric field. | 27 |

Chapter 3: Experimental Procedures

| |
|--|
| Fig. 3.1 A cross-sectional schematic of the MBE deposition chamber. The sample platter and two of the effusion cell clusters can be easily seen. The blue area is the liquid nitrogen cryopanel. Various measurement tools including RHEED imaging and QCM flux monitors are located around the outside of the |
|--|

| | |
|---|----|
| chamber. For scale, the diameter of this cylindrical chamber is approximately 34 inches. | 31 |
| Fig. 3.2 A picture of our multichamber deposition tool. The V_2O_3 films were deposited in the large MBE chamber on the right-hand-side labeled in green. All samples were inserted into the various chambers via the central robotics chamber and a common load lock. | 33 |
| Fig. 3.3 (a) A picture of the Physical Property Measurement System (PPMS) cryostat system by Quantum Design that we used for 4-point resistivity measurements of V_2O_3 . (b) A schematic of the sample puck showing a typical wirebonding arrangement. | 38 |
| Fig. 3.4 The V_2O_3 nanogap design. The top image shows two large contact pads used for landing probes, and the zoomed-in image shows the small, active area of the device between the two electrodes. Also visible are the Al_2O_3 pads used to isolate the contact lines from the sidewalls of the V_2O_3 mesa, which can become conducting during the mesa structure etch. Not visible is an adjacent grounding strip used during the high-speed transmission measurements. | 39 |
| Fig. 3.5 The device fabrication process. Step A is the mesa structure definition, Step B is the isolation pad deposition, Step C is nanogap deposition, and Step D is the contact pad deposition. Steps A, B and C are patterned with electron-beam lithography, and step D is patterned with optical lithography. | 40 |
| Fig. 3.6 Pictures of a fully processed wafer and devices at various levels of magnification. (a) V_2O_3 devices on a 1" sapphire substrate taken with a handheld camera. (b) Optical microscope image at the contact pad scale. (c) SEM image of the contact pads. (d,e) SEM images of a 125 nm gap device. | 43 |
| Fig. 3.7 A figure comparing, as a function of temperature, the device resistance that would be predicted by V_2O_3 's blanket film resistivity to the actual resistance of a fully patterned device measured at low bias. | 44 |
| Fig. 3.8 A figure showing several of the most frequent yield-related issues that we encountered during the fabrication of the V_2O_3 nanostructures. (a) A shorted device. (b) A thinning of the contact line over a step edge, resorting in a high | |

| | |
|---|----|
| resistance point that breaks open upon testing. (c) Fence edges around the nanogap contact lines, a mostly cosmetic issue that should not affect the performance of the device. | 45 |
| Fig. 3.9 (a) A picture of the Lakeshore variable-temperature probestation chamber. (b) A closer view of the RF probes and a sample placed on the stage. | 46 |
| | |
| Chapter 4: Thin Film Growth of V_2O_3 on Unannealed α-$Al_2O_3(0001)$ | |
| Fig. 4.1 A typical resistivity versus temperature plot for a 38 nm V_2O_3 film grown under optimal conditions. | 52 |
| Fig. 4.2 Typical RHEED and AFM data for V_2O_3 films grown on c -plane sapphire under optimal conditions. This particular film is approximately 38 nm in thickness, was grown at a substrate temperature of 700 °C, an oxygen pressure of 2.3×10^{-7} Torr, and displays 2.9 Å rms. The RHEED data were collected along the $[11\bar{2}0]$ azimuth. | 53 |
| Fig. 4.3 A TEM image of a 38 nm V_2O_3 film deposited at 850 °C along with selected-area fast Fourier transforms of the film and substrate, showing that the film grew epitaxially with the relationship $(0001) V_2O_3 // (0001) Al_2O_3$ and $[11\bar{2}0] V_2O_3 // [11\bar{2}0] Al_2O_3$ | 53 |
| Fig. 4.4 Coupled θ - 2θ X-ray diffraction scan. Reciprocal lattice of the $(10\bar{1}10) V_2O_3$ and Al_2O_3 Bragg peaks. Thickness fringes were only visible in roughly half of the grown films, and especially those grown in higher oxygen pressures. | 54 |
| Fig. 4.5 (a) RBS data showing the effect of using a gold backcoating to provide thermal absorption stability during deposition. (b) The same plot rescaled to show the gold contamination level. | 55 |
| Fig. 4.6 (a) A satellite-subtracted XPS spectrum for a nominally 40 nm thick film of V_2O_3 deposited on unannealed c -plane sapphire at 700 °C. The inset shows fits to the O(1s) and V(2p) peaks that are used for a rough calculation of | |

- stoichiometry. (b) A comparison of our V_2O_3 spectrum with various known spectra from previous work[104].56
- Fig. 4.7 Resistivity versus temperature sweeps for V_2O_3 deposited on unannealed c -plane sapphire at several temperatures between 600 and 850 °C and an oxygen partial pressure greater than 2×10^{-7} Torr. The electrical properties were extremely robust and reproducible within a growth window of 600 to 750 °C.59
- Fig. 4.8 (a) Resistivity versus temperature sweeps, and (b) symmetric θ - 2θ XRD scans collected from V_2O_3 films grown on unannealed c -plane sapphire substrates. The dotted lines indicate the bulk crystal values for $d_{(0006)}$ V_2O_3 and $d_{(111)}$ VO, taken from JCPDS references 00-034-0187 and 03-065-4054, respectively.60
- Fig. 4.9 (a) The rocksalt structure of VO, along with a planar cut of one of the (111) planes. (b) A straight-on view showing the triangular lattice of the vanadium atoms in a (111) plane of VO, the base-to-height distance of this particular triangle is 5.013 Å. (c) The VO(111) triangles nested into one monolayer of V_2O_3 , as viewed along V_2O_3 's (0001) axis. (d) A comparison of the RHEED patterns for VO and V_2O_3 , showing the disappearance of every 2nd and 3rd line. The black arrows in (c) show the RHEED beam diffraction spacing for V_2O_3 incident along the $[11\bar{2}0]$ direction. The green arrows in (c) show how this diffraction spacing shrinks by one-third, consistent with the RHEED streak spacing expanding by a factor of three in reciprocal space.61
- Fig. 4.10 Out-of-plane d-spacing parameters calculated from symmetric θ - 2θ XRD scans, and MIT temperatures extracted from the warming and cooling resistivity versus temperature curves. T_{MIT} is defined as the point of inflection, i.e. the temperature value showing the maximum derivative of $\log(\rho)$ with respect to temperature.62
- Fig. 4.11 (a) Activation energy and (b) insulating state resistivity ρ_{MIT} at T_{MIT} (filled shapes) and room-temperature resistivity ρ_{RT} (hollow shapes) plotted against T_{MIT} . The non-triangular data points represent data from previous studies on

V-deficiencies, Cr-doping and Ti-doping extracted from references[57, 59]. The triangular data points are from the V_2O_3 films in this study, with ρ_{MIT} being the resistivity value at T_{MIT} given by a functional fit to the insulating state, and ρ_{RT} being the resistivity value at 295 K. The ρ_{RT} data for $(Ti_xV_{1-x})_2O_3$ could not be accurately obtained and are omitted. It should be noted that sample doping levels and stoichiometries are implicitly expressed on the x-axis in terms of T_{MIT}63

Chapter 5: Growth of V_2O_3 on Other Substrates

Fig. 5.1 Atomic force microscopy images of (a) a *c*-plane NA-sapphire substrate, (b) a 38 nm V_2O_3 film grown on NA-sapphire, (c) a *c*-plane AN-sapphire substrate annealed at 1050 °C for 90 minutes to produce an ultra-smooth surface, and (d) a 43 nm V_2O_3 film grown on AN-sapphire. The root-mean square roughnesses of these four surfaces are 1.2 Å, 2.9 Å, 0.9 Å and 2.4 Å, respectively.68

Fig. 5.2 (a,b,c) RHEED patterns taken along the $[11\bar{2}0]$ azimuth before, during, and after deposition of a 38 nm V_2O_3 film onto NA-sapphire. (d,e,f) Equivalent images taken before, during, and after deposition of 43 nm of V_2O_3 onto AN-sapphire. (g) Examples of specular spot intensity oscillations and streak spacing as a function of time for two different V_2O_3 films deposited on AN-sapphire under similar conditions. The discontinuous jumps in the oscillation data between 2 and 3 minutes are due to manual readjustment of the electron beam's grid voltage. The period of oscillation is approximately 48 seconds, corresponding to a deposition rate of 0.05 Å/s, or 0.3 nm/min. No oscillations occurred for films grown on NA-sapphire.70

Fig. 5.3 (a) Typical θ - 2θ X-ray diffraction scans showing the (0006) out-of-plane peaks for V_2O_3 films on both NA- and AN-sapphire. The expected peak position for bulk V_2O_3 was taken from JCPDS reference 00-034-0187. (b) A plot versus thickness of the extracted FWHM of V_2O_3 's (0006) peak for films deposited on both NA- and AN-sapphire. Also plotted is the FWHM

that would exist purely due to thickness broadening as predicted by the Scherrer equation[111]. The inset cartoon depicts how good epitaxy might lead to island-like growth and various types of peak broadening.71

Fig. 5.4 Four-point probe resistivity measurements versus temperature for a representative selection of V_2O_3 film thicknesses deposited onto (a) NA-sapphire and (b) AN-sapphire.73

Fig. 5.5 (a) An AFM image of a nominally 40 nm thick V_2O_3 film on *a*-plane sapphire grown at 700 °C in the highest O_2 growth pressure tested, 3.8×10^{-7} Torr. The RMS roughness of this film is 7 Å, much higher than for films grown on *c*-plane sapphire. (b,c) Typical RHEED images taken before and near the end of deposition for films on *a*-plane sapphire. A very faint 3x1 pattern exists in (c), perhaps indicating the formation of a second phase. ...75

Fig. 5.6 (a,b) Resistivity versus temperature and coupled θ - 2θ XRD scans for V_2O_3 films nominally 40 nm in thickness deposited at 700 °C on *a*-plane sapphire substrates. (c,d) Resistivity versus temperature and coupled θ - 2θ XRD scans for various thicknesses of V_2O_3 deposited on *a*-plane sapphire in partial pressures held between 4×10^{-8} and 6×10^{-8} Torr. The V_2O_3 peak positions are consistently shifted to smaller 2θ angles corresponding to a 0.2%-0.4% out-of-plane expansion along the $[11\bar{2}0]$ axis which is generally more pronounced in the thinner films.76

Fig. 5.7 (a,b) RHEED and AFM data for a *c*-plane $LiTaO_3$ substrate prior to deposition. (c,d) RHEED and AFM data for a nominally 24 nm thick V_2O_3 film on *c*-plane $LiTaO_3$. The film appears to grow very two-dimensionally. The RMS roughnesses of images (b) and (d) are 1.3 Å and 1.1 Å, respectively.79

Fig. 5.8 RHEED streak relaxation data for a V_2O_3 film deposited at 700 °C on an annealed $LiTaO_3$ substrate compared with data for a V_2O_3 film deposited under similar conditions on an annealed *c*-plane sapphire substrate. 5 minutes of growth corresponds to roughly 2 nm of V_2O_3 thickness. The film on sapphire relaxes in approximately 2 nm. The film on $LiTaO_3$ however, relaxes

| | | |
|-----------|---|----|
| | much more slowly, implying the film is more coherently strained. This could occur either due to the slightly smaller lattice mismatch afforded by LiTaO ₃ or a greater ability for the film to accommodate tensile strain rather than compressive strain. | 80 |
| Fig. 5.9 | (a) Resistivity versus temperature sweeps, and (b) symmetric θ - 2θ XRD scans collected from V ₂ O ₃ films grown to various thicknesses on annealed <i>c</i> -plane LiTaO ₃ substrates at 700 °C. The dotted line indicates the bulk crystal value for $d_{(00012)}$ LiTaO ₃ taken from JCPDS reference 00-029-0836. | 81 |
| Fig. 5.10 | AFM images of the surfaces of Cr ₂ O ₃ buffer layers grown to approximately 40 nm in thickness at a growth temperature of 700 °C. | 82 |
| Fig. 5.11 | The RMS roughness of Cr ₂ O ₃ buffer layers grown to approximately 40 nm in thickness at a growth temperature of 700 °C. | 83 |
| Fig. 5.12 | Coupled θ - 2θ XRD scans for nominally 40 nm thick Cr ₂ O ₃ films deposited on annealed <i>c</i> -plane sapphire substrates at various growth temperatures. (Note: these data were collected on a low-resolution general area diffractometer in a coupled-scan mode with no calibration. The spectra were shifted post-measurement to align the substrate peaks to the theoretical bulk values for α -Al ₂ O ₃ (0006)). | 84 |
| Fig. 5.13 | Resistivity versus temperature sweeps for nominally 6 nm thick V ₂ O ₃ thin films deposited at 700 °C onto four different surfaces: AN-sapphire, AN-LiTaO ₃ , a 10 nm buffer layer of Cr ₂ O ₃ deposited at 500 °C, and a 5 nm buffer layer of Cr ₂ O ₃ deposited at 800 °C. | 85 |

Chapter 6: Growth of V₂O₃ on Other Substrates

| | | |
|----------|---|----|
| Fig. 6.1 | (a) SEM image of a nominally 125 nm x 470 nm device. (b) An optical microscope view of two high-speed probes landing on the device and an adjacent grounding strip. (c) A cross-sectional schematic of the V ₂ O ₃ devices showing the two different types of measurements: direct-current and pulsed-voltage. | 90 |
|----------|---|----|

- Fig. 6.2 (a) A simple circuit diagram showing the difference between the circuit voltage and the device voltage. Circuit voltages were experimentally measured and converted to device voltages by subtracting the voltage drop across the known external load resistance. (b) Current-voltage sweeps with a 10 k Ω load resistance from a nominally 125 nm x 470 nm device at a range of different temperatures between 10 K and 290 K. (c) Selected sweeps from same device plotted in terms of resistance versus voltage.92
- Fig. 6.3 (a) Threshold voltage, (b) threshold current, and (c) threshold power plotted against temperature for a 125 nm x 470 nm device. The data points and error bars represent mean and standard deviations taken from six repeated measurements at each temperature.93
- Fig. 6.4 Threshold switching voltages versus nominal gap size extracted from I-V staircase sweeps on V₂O₃ nanostructures at an ambient temperature of 10 K. The data and error bars represent mean and standard deviations from a sample of five different devices at each gap size of 75 nm, 125 nm, 175 nm, and 225 nm. The linear behavior suggests a threshold electric field of approximately 1.9×10^7 V/m at 10 K.94
- Fig. 6.5 The three different regimes of device behavior. A) The low-temperature and low-bias insulating state, B) unstable circuit behavior near the threshold voltage, and C) the high-temperature and high-bias conducting state. These data were collected on a 125 nm gap V₂O₃ nanostructure at an ambient temperature of 10 K with a series load resistance of 10 k Ω95
- Fig. 6.6 Current plotted against the square root of the device voltage. The resulting linear behavior is a strong indication of a Poole-Frenkel type conduction mechanism with a relatively constant device temperature. The data are from a 125 nm x 470 nm device.96
- Fig. 6.7 Voltage-controlled oscillations in a 75 nm x 870 nm device at 10 K. The plots on the left show the current-voltage data as measured by a Keithley source-measure unit, and the plots on the right show the time-dependence of the voltage drop across the V₂O₃ device, deduced from oscilloscope measurements of the voltage drop across the load resistance.98

- Fig. 6.8 (a) A phase diagram showing the load resistances and voltages required to induce oscillations in the circuit. (b) Oscilloscope traces for a 50 k Ω load resistance. (c) FFTs of the traces at 4V and 5V, demonstrating how we extracted the frequency of oscillation. (d) The frequency of oscillation plotted against circuit voltage for a 50 k Ω load, along with the predicted fit from a simple capacitive charging model.99
- Fig. 6.9 (a) A current-voltage sweep, plotted on a log scale, for a nominally 75 nm x 470 nm device. (b) The same data plotted in terms of resistance, which has been normalized to the room-temperature resistance of the device. In the high-voltage state, increasing voltages cause discrete jumps in resistance that cease to occur once the device has a resistance roughly equal to its high-temperature resistance. This is strong evidence for expansion of a hot conducting filament.101
- Fig. 6.10 (a,b) High-speed oscilloscope traces taken at 40 K, and (b) experimentally measured incubation times extracted from many of these types of traces at various temperatures. The data points and error bars correspond to mean and standard deviations taken from a sample of five repeated measurements at each temperature.103

Chapter 7: Thermal Modeling and Comparison to Experiment

- Fig. 7.1 A plot of V₂O₃'s specific heat versus temperature calculated from the Debye equation for a characteristic Debye temperature of 600 K.107
- Fig. 7.2 The incubation times predicted from a simple model for the 125 nm x 470 nm device presented in Chapter 7. A constant threshold power of 2 μ W was used to calculate the time to heat a V₂O₃ volume of $\Omega = (50nm) \times (125nm) \times (470nm)$ from various starting ambient temperatures to V₂O₃'s metal-insulator transition temperature of 160 K. This model includes V₂O₃'s temperature-dependent specific heat, but ignores Poole-Frenkel-type conductivity enhancements, temperature-related feedback effects, and also heat dissipation.108

- Fig. 7.3 Plots of the current-voltage fitting parameters γ and η , as a function of temperature, extracted from a fit of the equation $\ln(I(V,T)) = \gamma(T) + \eta(T)\sqrt{V}$ to experimental data. The data correspond to the mean and standard deviation of γ and η values extracted from six independent staircase sweeps. The red curves are fits, as described in the text, to be used for smoothly parameterizing these data for use in a numerical Joule heating model.110
- Fig. 7.4 (a) The current-voltage data for a 125 nm x 470 nm device presented in Chapter 7, and (b) our parameterized fit for $I(V,T)$112
- Fig. 7.5 A current-voltage sweep for the 125 nm x 470 nm device presented in chapter 7, showing the condition used to calculate the heat dissipation parameter λ . At the circled point, it is assumed that the device has a temperature $T > 160$ K. The observed input power of 0.404 mW then corresponds to a maximum possible heat dissipation parameter of $\lambda = 2.82 \times 10^{-6}$ W/K.113
- Fig. 7.6 Joule heating simulation results for the 125 nm x 470 nm device presented in chapter 7: (a) The steady-state device temperature reached for voltages below threshold, and (b) device temperature versus time predictions for voltages near the threshold voltage. These two types of plots allow us to generate threshold voltage and switching time predictions as a function of temperature to compare to experimental data. These curves were generated using a heat dissipation parameter of $\lambda = 2.00 \times 10^{-7}$ W/K. Also, note the effect of the 390 ps pulse rise time in plot (b).114
- Fig. 7.7 (a) Experimental threshold voltage data compared with predictions from our numerical modeling for two different values of λ . (b) Experimental switching time data compared with predictions from our numerical modeling for a heat dissipation value of $\lambda = 2.0 \times 10^{-7}$. The dotted lines in (b) correspond to an instantaneously fast voltage pulse, and the solid lines correspond to a voltage pulse that turns on with a rise time of 390 picoseconds.115

List of Tables

Chapter 4: Thin Film Growth of V_2O_3 on Unannealed $\alpha-Al_2O_3(0001)$

- Table. 4.1 The in-plane and out-of plane lattice parameters for the most-common corundum-type rhombohedral oxides. These parameters are taken from the Joint Committee on Powder Diffraction Standards (JCPDS) database.49
- Table 4.2 A table showing the binding energies for the O(1s) and V(2p_{3/2}) peaks of various different phases of vanadium oxide extracted from Ref[104], along with experimental values from the present work measured by XPS on a 40 nm V_2O_3 film grown by oxygen plasma-assisted thermal evaporation. The energy difference between the peaks, Δ , that we observe is consistent with the previously reported values for bulk samples of V_2O_357
- Table 4.3 A table showing the binding energies for various XPS peaks from a 40 nm film of V_2O_3 . The O(1s) and V(2p_{3/2}) peak areas can be used to obtain a rough estimate of the surface stoichiometry based on atomic sensitivity factors provided in Ref[108].....58

Chapter 5: Growth of V_2O_3 on Other Substrates

- Table 5.1 A table, reproduced from Ref[99], showing the thermal expansion coefficients of the a-axes and c-axes of V_2O_3 and Al_2O_3 . The negative c-axis thermal expansion is most likely responsible for the out-of-plane d-spacing expansion we observe for films grown on a-plane sapphire.....77

Chapter 7: Thermal Modeling and Comparison to Experiment

- Table. 7.1 Fitting parameters extracted from a least-squares fit of $\gamma(T)$ and $\eta(T)$ based on Eq. 7.6 and Eq. 7.7.....111

Chapter 1

INTRODUCTION

1.1 Motivation

The field-effect transistor, discovered at Bell Laboratories more than sixty years ago, is now an essential part of modern life. By many estimates, the world now manufactures more than ten quintillion, or 10^{19} , of these devices every year to serve as building blocks for the integrated circuits we use to control our computers, telephones, vehicles and households. For this reason, fundamental research on new transistor materials and field-effect switching phenomena is very easily justified. Due to the tremendous scale of production involved, even a marginal improvement in performance for a niche operating condition could lead to very significant total savings in energy and cost.

Historically, technological development of silicon-based transistors has been guided by “Moore’s Law,” an observation that, largely to reduce manufacturing costs, the number of transistors per chip has doubled roughly every two years[1], accompanied by lockstep improvements in efficiency and speed associated with traditional device scaling[2]. However, as the critical dimensions of the transistor have approached today’s minuscule size of just 22 nm, these benefits have become more and more difficult to realize, requiring such ingenuities as high-K dielectric gate oxides to reduce leakage currents, strained silicon to improve the channel mobility, and three-dimensional gates to reduce operating voltages. We are now at a point where the path forward is becoming less and less clear. The continued exponential growth of the semiconductor industry, if at all possible, will likely deviate from traditional scaling methods and move to the use of a different channel material. This dissertation is an investigation of two-terminal field-effect switching in an unconventional class of materials: Mott insulators. Specifically, we explore the physical mechanism responsible for reversible, electric field-induced conductivity switching in the low-temperature insulating state of V_2O_3 , a well-known Mott insulator that displays metal-insulator transitions as a function of temperature, chemical doping, and pressure.

A Mott insulator can be generally characterized as a material whose conduction electrons are gridlocked into a traffic jam that impedes the normal flow of current. This gridlock is created because the material has one valence band electron per atomic site, and Coulomb repulsion forces make the double occupation of these sites energetically

unfavorable, as depicted in Fig. 1.1. In the framework of solid-state physics, electron-electron interactions are responsible for opening up an energy gap U that splits what would otherwise be a metallic, half-filled conduction band into a filled Lower Hubbard Band and an empty Upper Hubbard Band[3, 4]. Since this insulating state requires exactly one electron per site, the transport properties should be extremely sensitive to even incremental changes in carrier density. This property of Mott insulators is what makes them an appealing candidate for field-effect experiments[5, 6].

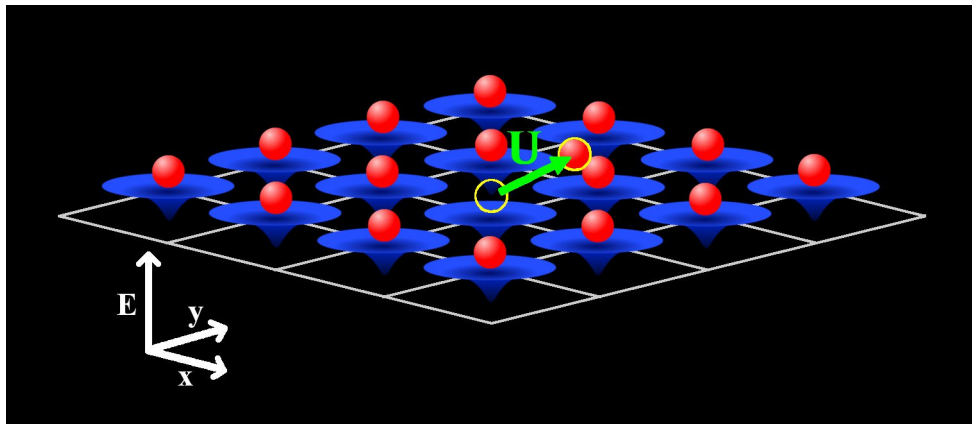


Fig. 1.1 A simple picture of the gridlocked electrons in a Mott insulator. At an integer filling of electrons per site, conduction is blocked by the Coulomb repulsion energy U that must be provided for two electrons to occupy the same site.

It should be noted that Mott insulators such as V_2O_3 are members of a much broader class known as strongly correlated electron materials, which includes any material having emergent physical properties that are strongly influenced by the interactions between its electrons. The electron-electron interactions need not always be Coulomb repulsion in nature, and they can involve spin, lattice and orbital coupling as well. To appreciate the strongly correlated material's place in the universe, it is instructive to consider the full spectrum of possible crystalline condensed matter systems, sorted by the degree to which their electrons' probability density functions are localized, as depicted in Fig. 1.2. In one extreme, electrons are tightly bound to their donor nuclei and have spatially localized wave functions. These states have discrete energy levels,

just as they would in an isolated atom. In the other extreme, nearly free electrons exist as delocalized Bloch waves. The energy levels of these states form continuous bands, and the filling of these bands determine whether the system is insulating or conducting. Strongly correlated electron materials exist in the middle ground between these two extremes, and they can demonstrate a multitude of exotic and technologically useful properties such as high-temperature superconductivity[7, 8], ferroelectricity[9], half-metallicity[10], colossal magnetoresistance[11], and metal-to-insulator transitions[4]. Furthermore, these properties can be highly sensitive to carrier concentration, opening up the possibility for a whole new class of proposed field-effect devices[12, 13]. Typically, strongly correlated electron materials are transition metal oxides, and the electron-electron interactions arise between spatially expansive d or f orbitals that are separated by oxygen atoms. The result is that the system forms relatively narrow energy bands with electrons just on the cusp of localization. An elementally pure transition metal like iron or copper, by comparison, has very large overlap integrals, wide bands and fully delocalized electrons due to their increased proximity to one another.

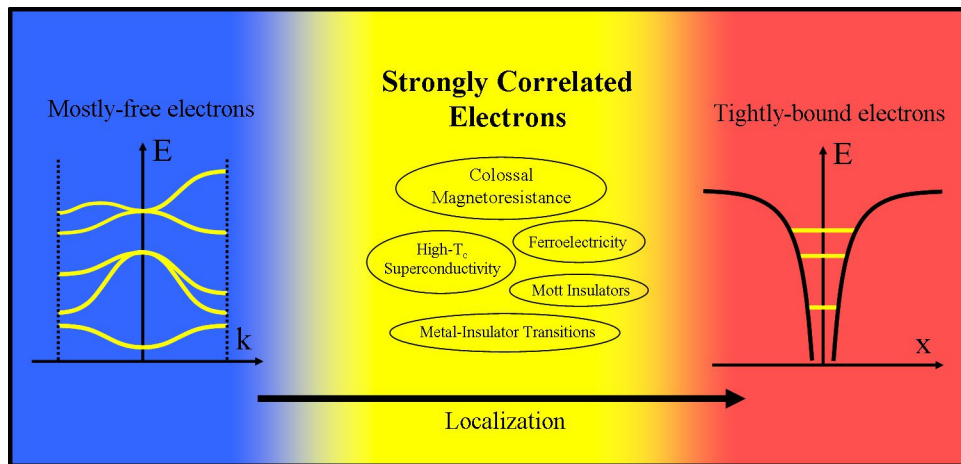


Fig. 1.2 A generalized spectrum of condensed matter systems, sorted by degree of electron localization. Strongly correlated materials lie in the fertile middle ground between systems with mostly-free electrons and systems with tightly-bound electrons, and they are host to a number of materials with exotic and technologically useful properties.

One novel example of an electric field effect in a strongly correlated material, first demonstrated in 2004, is that a high-mobility two-dimensional electron gas exists at the interface between the transition metal oxides SrTiO₃ and LaAlO₃[14]. The precise details of this system are still under debate, but it is generally believed that an internal electric field, arising from a discontinuity in crystalline charge polarity, draws charges to the interface where they become mobile. In 2006, it was shown that in a three unit cell thick LaAlO₃ film on STO, one monolayer shy of the four unit cells needed to create the two-dimensional electron gas, the metallicity of the interface could be controlled with a gate voltage[15]. After these seminal discoveries, the search for gate voltage-induced effects in oxides and nitrides intensified with the help of a new technique known as electric double-layer ionic gating, resulting in discoveries of gate voltage-induced metallicity in ZnO[16], superconductivity in STO[17] and ZrNCl[18], and ferromagnetism in Co-doped TiO₂[19], to name several examples. An electric double-layer transistor device differs from a conventional metal-oxide-semiconductor transistor in that the gate voltage is applied across a liquid electrolyte rather than a simple dielectric. In this configuration, charged ions are driven very close to the surface of the channel, leading to oppositely charged layers on both sides of the electrolyte-channel interface. These layers typically have a separation less than 1 nm, and they can support electric fields as strong as 10 MV/cm[20].

In traditional experiments on two-terminal devices, which we study in this dissertation, it has been discovered that a number of different correlated insulators show threshold-type switching behavior that appears to be electronic in nature. These materials include VO₂[21-23], V₂O₃[24, 25], Pr_{1-x}Ca_xMnO₃[26], La_{2-x}Sr_xNiO₄[27], Sr_nCuO_{n+1}[28], and Fe₃O₄[29]. Indeed, recent theoretical work[30-32] has suggested that Mott insulators might have a lowered dielectric breakdown strength due to a tunneling-assisted delocalization process. Adding to the excitement, ultra-high-speed, laser-induced switching experiments on VO₂ have shown that the switching process can occur in as fast as 80 femtoseconds[33, 34]. Significant questions remain, however, about the true nature of the observed experimental results on two-terminal devices, especially concerning the degree to which Joule heating plays a role. The conclusion will have important implications on the ultimate usefulness of any devices based on these materials. It is the

goal of this dissertation to help answer that question for V_2O_3 , one of the clearest and most well-known examples of a Mott insulator. Fortunately, new advances in high-speed electronics, film growth techniques, and lithographic resolution allow us to study this phenomenon with previously unachievable film time scales, device sizes, and film quality.

1.2 Overview of Work

When cooled to approximately 155 K, V_2O_3 undergoes a first-order phase transition from a paramagnetic metal to an antiferromagnetic insulator, accompanied by a monoclinic distortion of its rhombohedral structure[35]. In bulk crystals, the conductivity change across this transition can be more than seven orders of magnitude. This metal-insulator transition has a very rich phase diagram as a function of external pressure, doping, and stoichiometry[36]. In this work, we grow high quality epitaxial films of V_2O_3 onto *c*-plane sapphire substrates, fabricate two-terminal nanogap devices from these films, and then study V_2O_3 's transport properties at low temperature and under high electric fields in search of clear evidence for an electronic switching process. A simplified version of the basic experimental setup involved can be seen in Fig. 1.3.

The fundamental difficulty in determining whether thermal or electronic processes are responsible for triggering insulator-to-metal transitions in correlated insulators is primarily due to uncertainty about the volume of the initial switching region. Avalanche effects, positive feedback via Joule heating, and material inhomogeneities may all lead to a nonuniform current flow that can be confined to a small and difficult-to-estimate volume. There are three main ways to minimize these effects. The first is to study field-induced switching in very small devices to obtain a more accurate estimate of the switching volume. The second is to prepare smooth, single-crystalline, and epitaxial films to make the switching process as homogeneous as possible. The third is to perform the experiments at low temperature on very resistive materials to greatly reduce the magnitude of the leakage current and heating. In this work, we have attempted to take full advantage of all three of these techniques. We fabricate two-terminal nanogap devices of V_2O_3 with electrode-to-electrode spacings as small as 75 nm on top of ultra-

smooth, epitaxial V_2O_3 films. We also test these devices at temperatures as low as 10 K, where the two-terminal resistances are greater than $10^{10} \Omega$. If any correlated insulator is to show unambiguous evidence of electric field-induced switching that is not directly caused by Joule heating, we believe it would most likely be V_2O_3 measured under these conditions.

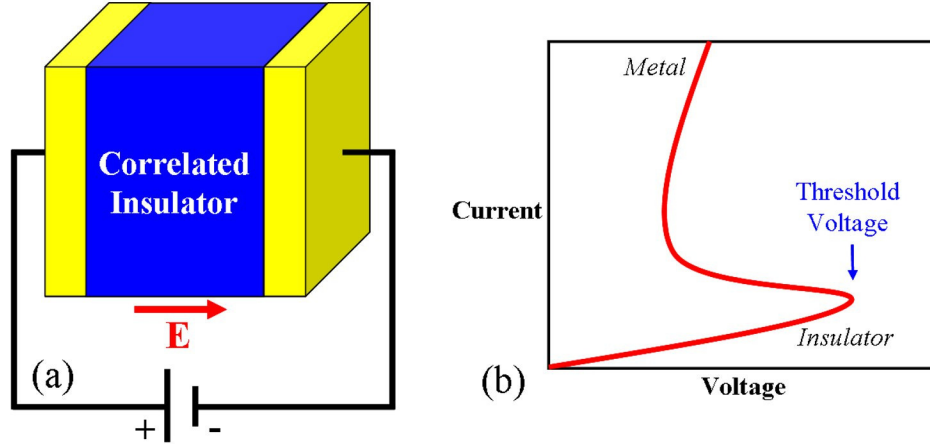


Fig. 1.3 The conventional experimental setup for studying two-terminal electric field-induced switching in correlated insulators. (a) A circuit diagram showing a correlated insulator sandwiched between two electrodes under an applied bias, and (b) a typical I - V curve showing that a threshold voltage will cause the device to switch into a high-conductance state. Upon removal of the bias, the material reversibly returns to the insulating state with no memory effect.

The main findings can be categorized into three parts: film growth, electrical measurement, and electrothermal modeling. In the first part, we discuss the growth, optimization, and characterization of high-quality epitaxial V_2O_3 films, including the effect of oxygen pressure, substrate temperature and substrate material on the film properties. In the second part, we show experimental results on electric field-induced phase transitions in V_2O_3 nanostructures fabricated by electron beam lithography. We observe that a threshold electric field of approximately 10^7 V/m applied across two-terminal nanostructures causes a metallization of V_2O_3 's low-temperature Mott insulating state, preceded by a nanosecond-scale delay time. In the final part, we explore the feasibility of Joule heating as an explanation for the switching process. After fully accounting for temperature-related feedback and subthreshold nonlinear current-voltage characteristics, we find remarkably good agreement between the predicted and observed

threshold voltages and switching delay times as a function of temperature, suggesting the switching mechanism is thermal in origin. We believe these findings suggest that other recent observations of electric field switching in the related materials VO_2 and Fe_3O_4 are thermal in nature as well, and we hope our work will guide future research on this phenomenon.

1.3 Dissertation Structure

Chapter 2 provides a collection of relevant background information. We begin with an introduction to metal-insulator transition physics, followed by a review of previous experimental and theoretical work on field-induced switching experiments in correlated insulators. We also cover the basic physical properties of V_2O_3 , including its phase diagram and band structure. Lastly, we provide some important details about charge transport phenomena commonly found in insulators.

Chapter 3 provides an overview of the experimental apparatus and procedures used in this work. We discuss our film growth and characterization techniques. We also present a detailed description of the device fabrication process. Lastly, we describe the equipment used to electrically measure the direct-current and high-speed switching characteristics of the V_2O_3 devices.

Chapter 4 begins the presentation of experimental results with details on the optimization and characterization of V_2O_3 films grown on unannealed *c*-plane sapphire substrates. We discuss the role of the substrate, the growth temperature, and the growth oxygen pressure on the chemical, structural and electrical properties of the films. Decreasing oxygen pressure present in the chamber during growth is shown to systematically increase V_2O_3 's metal-insulator transition temperature in a manner consistent with doping experiments in bulk crystals. Under optimized conditions, we show that V_2O_3 can be grown smoothly and epitaxially onto *c*-plane sapphire substrates with good electrical properties, namely a strong 4-5 order of magnitude metal-to-insulator transition that occurs upon cooling the films down to below 150 K. The films discussed in this chapter are identical to those ultimately used for the fabrication of nanostructures for the field-effect switching experiments.

In chapter 5, we explore the growth of V_2O_3 on other substrates, namely, annealed c -plane sapphire, unannealed a -plane sapphire, annealed $LiTaO_3$ substrates, and Cr_2O_3 buffer layers. For example, we show that annealing the c -plane sapphire substrates prior to deposition to produce ultra-smooth terraced surfaces with atomic-scale step heights ultimately degrades the quality of the V_2O_3 films due to a higher level of epitaxy and strain transfer at the interface. Although these films were not used in our switching experiments, we present this work here because we believe it will offer valuable insight for future attempts to produce even higher quality V_2O_3 films and interfaces.

In Chapter 6, we present electrical transport measurements performed on the V_2O_3 nanostructures at various temperatures ranging between 10 K and 300 K. These experiments consist of both direct current (DC) current-voltage (I-V) sweeps and time-resolved high-speed pulses measured in a transmission geometry. We discuss the DC behavior of the devices in each of three regimes: voltages below threshold, voltages near threshold, and voltages above threshold. Below threshold, we see nonlinear Poole-Frenkel-type conduction, near threshold we observe voltage-controlled oscillations, and above threshold we see evidence of a hot, conducting, filament that expands in size. Most importantly, we extract data about threshold conditions as a function of temperature to gain insight into the triggering mechanism. The high-speed, pulsed measurements provide a direct measurement of the time required for the V_2O_3 to transform to the conducting state for a given applied electric field above the threshold voltage. The switching is revealed to occur in a two-step process consisting of a delay time, or incubation time, before any measurable conduction occurs followed by the actual metallization process, both of which occur on the nanosecond timescale. The extracted threshold voltages and incubation times as a function of ambient temperature comprise the most important experimental data that we will use, in Chapter 7, to evaluate the feasibility of Joule heating as an explanation for the switching process.

In Chapter 7, we hypothesize that a simple thermal model might account for the observed experimental data collected on V_2O_3 's electric field-induced switching process. We compare models calculated from various different starting assumptions and conclude that, when the effects of positive feedback, heat dissipation, and Poole-Frenkel conductivity enhancements are all properly taken into account, the estimated switching

voltages and incubation times match experimental data extremely well. In other words, we find no strong evidence to discard a Joule heating hypothesis, and we conclude that a feedback-enhanced change in device temperature is the most likely triggering mechanism for the electric field-induced switching of V_2O_3 's low-temperature insulating state.

In chapter 8, we summarize our work and discuss the implications of our findings on the field of threshold switching. To conclude, we present some ideas for future work in this field.

Chapter 2

BACKGROUND

2.1 Introduction

In this chapter, we provide a collection of relevant background information pertaining to electric field-driven metal-insulator transitions. We begin with a general introduction to metal-insulator transition physics. This is followed by a review of recent theoretical and experimental reports of electric field-driven switching in two-terminal devices. Next, we cover the basic properties of V_2O_3 , including its phase diagram, crystal structure and band structure. We conclude with an overview of high-field charge transport phenomena in insulators.

2.2 Metal-Insulator Transitions

2.2.1 The Hubbard Model

The most fundamental difference between a metal and an insulator is the existence of a Fermi surface, or a partially filled valence band. This simple distinction allows one to easily predict *a priori* whether or not many materials will be conducting or insulating. Magnesium oxide, for example, should be an insulator because it has filled p bands, whereas iron should be a good conductor because it has partially filled d bands. Some materials, however, do not follow this convention, with the insulator NiO being one of the most well-known examples. The reason for this disagreement is that conventional band theory largely ignores the effects of electron-electron interactions on a material's band structure. One of the simplest models that can appropriately capture this type of behavior is the single-band Hubbard model:

$$H = -t \sum_{\langle i,j \rangle, \sigma} (c_{i,\sigma}^\dagger c_{j,\sigma} + h.c.) + U \sum_{i=1}^N n_{i\uparrow} n_{i\downarrow}, \quad (2.1)$$

where H is system's Hamiltonian operator, t is the hopping integral, $c_{i,\sigma}^\dagger$ and $c_{i,\sigma}$ are the creation and annihilation operators for an electron on site i with a spin σ , U is the Coulomb repulsion energy, and $n_{i,\sigma}$ is the number operator[37]. In this model, the electron filling and the ratio U/W between the Coulomb repulsion energy and the electron

band width both turn out to be very critical parameters that can drive metal-insulator transitions.

Consider the Hubbard model applied to an infinite, one-dimensional chain of hydrogen atoms with lattice spacing δ . The electrons around these atoms occupy ground-state 1s orbitals with two available states: spin up and spin down. Regardless of the value of δ , there will always be a nonzero overlap integral between two adjacent electron wavefunctions. The available electron energies will therefore form a band with a width W that depends on δ . Furthermore, this band will be half-filled since there are two degenerate states available to each electron. Ignoring electron-electron interactions, this system should be metallic for any value of δ . This result, however, is wrong, because in reality the system will become insulating as the hydrogen atoms are pulled farther and farther apart. This shortcoming is resolved when the electron-electron interaction term U is included. The Hubbard model predicts that when U/W is large enough, which will occur for large values of δ , the half-filled band will split into an upper and lower Hubbard band. The lower band will be fully occupied and the upper band will be empty, which is the recipe for an insulator. The physical picture corresponding to this mathematical description is that the electrons become gridlocked into a traffic jam, one per each atomic site. No electron can move to any other site because it would have to pay an extra energy U to accommodate the double occupation.

2.2.2 Two Routes across the Metal-Insulator Transition

Note that in the Hubbard model, a higher value of U leads to insulating behavior, and a higher value of W (or t) leads to metallic behavior. The competition between U and W can cause metal-insulator transitions. In the case of the one-dimensional hydrogen chain, a metal-insulator transition will occur as a function of the spacing between hydrogen atoms. This type of transition is a band-width-controlled metal-insulator transition, or BC-MIT. Alternately, if the band filling is changed, by adding extra electrons to the system, or taking some away, the condition of gridlock will no longer apply and the system will become metallic. This type of transition is a filling-controlled metal-insulator transition, or FC-MIT. These two different routes to a metal-insulator transition in a correlated electron system are depicted in Fig. 2.1.

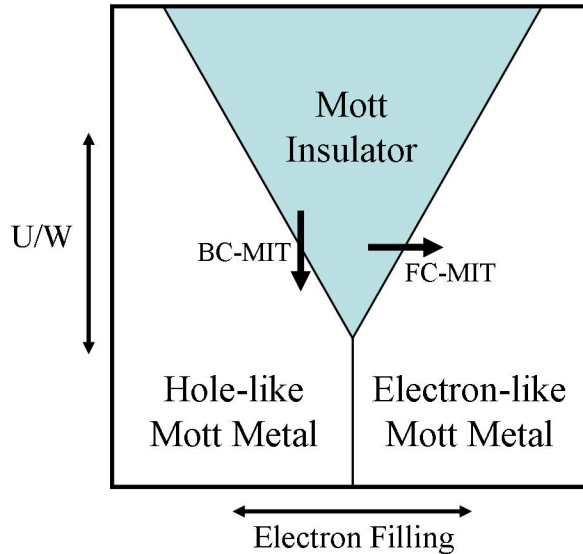


Fig. 2.1 Reproduced from Ref[4], the phase diagram of a Mott-Hubbard system as a function of electron filling and U/W . Two routes of transitioning across the metal-insulator boundary are depicted. The metallic state in the shaded region is highly sensitive to disorder-induced localization.

The distinction between these two types of metal-insulator transitions will be useful when we consider the various metal-insulator transitions of V_2O_3 that can occur with changes in temperature, doping, and external pressure. All of these MITs can be attributed, at least qualitatively, to changes in band filling and band structure, as predicted by the Hubbard model. It should be noted, however, that the precise details of any real system are vastly more complex than the simple Hubbard Model. Spin, orbital, and lattice interactions can all add additional degrees of freedom to the system that greatly complicate first-principles calculations. We direct the interested reader to Ref[4] for an excellent discussion of this topic.

The field-induced switching phenomenon in V_2O_3 that we investigate in this thesis, if electronic, would fall into the FC-MIT category. Carrier injection from the electrodes or electric field-assisted tunneling can both theoretically change the density of ground state electrons and collapse the separated Hubbard bands back into a single, half-filled metallic band.

2.2.3 Mott-Hubbard vs. Charge-Transfer Insulators

Based on the energy separation Δ between the d and p bands, correlated insulators can be classified as either Mott-Hubbard (MH) insulators or Charge-Transfer (CT) insulators[38]. The difference between these two situations is depicted in Fig.2.2. When $U > \Delta$, we get the normal case of a Mott-Hubbard insulator where the partially filled d band is split by the Coulomb repulsion energy U . However, when $U < \Delta$, the resulting conduction gap is decreased to Δ and lies between the Upper Hubbard Band and the filled p band. This type of insulator is referred to as a Charge-Transfer insulator. Following the convention of Ref[4], we will refer to both types of these insulators as Mott insulators throughout this text.

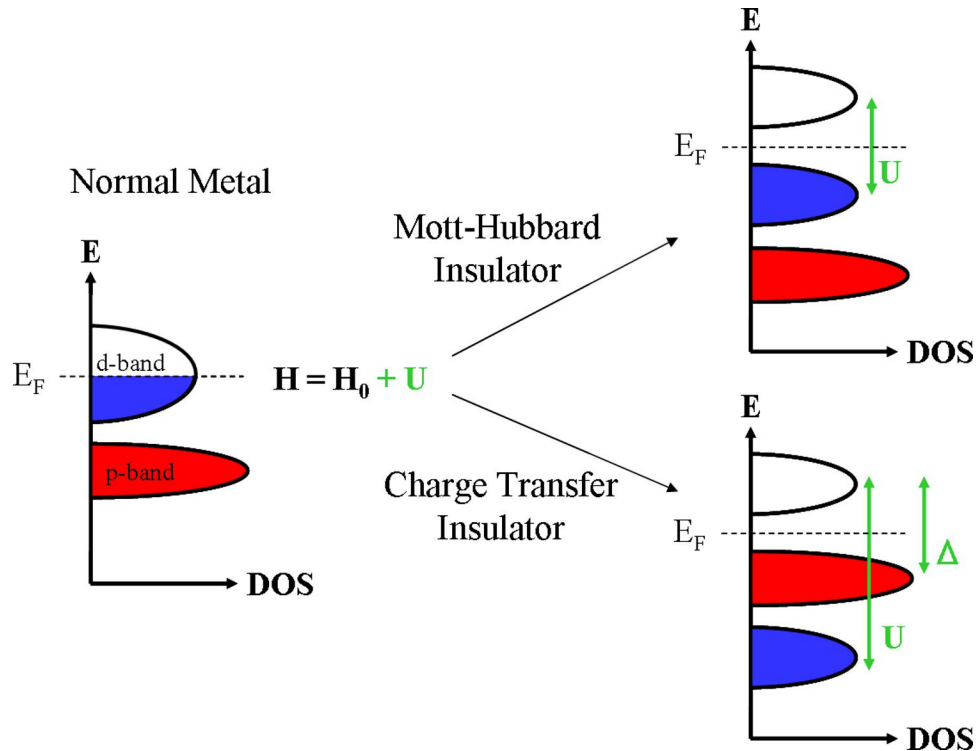


Fig. 2.2 Adapted from Ref[4], energy level diagrams for the two different kinds of Mott insulators. The splitting energy U generated by the on-site coulomb repulsion can split the d -band in two distinct ways with respect to the p bands.

Fig. 2.3 shows a compilation of various correlated insulators plotted on a phase diagram with axes proportional to U and Δ . It is immediately clear that most materials are CT-type rather than MH-type, meaning that the electrical transport properties are

determined by Δ rather than the full Mott-Hubbard gap U . In fact, true MH-type insulators are rare, and even rarer are ones that display large changes in conductivity across the MIT like V_2O_3 . The distinction is an important one, because to unambiguously identify that some type of electric field effect can cause the collapse of the MH gap U , it is desirable to minimize leakage currents. Thus, for a fixed MH gap U , an MH-type insulator will generally have less leakage current than a CT-type. Another report[39], has suggested that V_2O_3 is a good example of an MH-type insulator, whereas materials like VO_2 and the rare earth nickelates are CT-type insulators. We believe that this information, combined with V_2O_3 's very dramatic change in conductivity at the MIT and its known sensitivity to doping, suggests that V_2O_3 is one of the best possible testing grounds for unambiguously identifying any Mott-related electric field-induced switching phenomena that might exist.

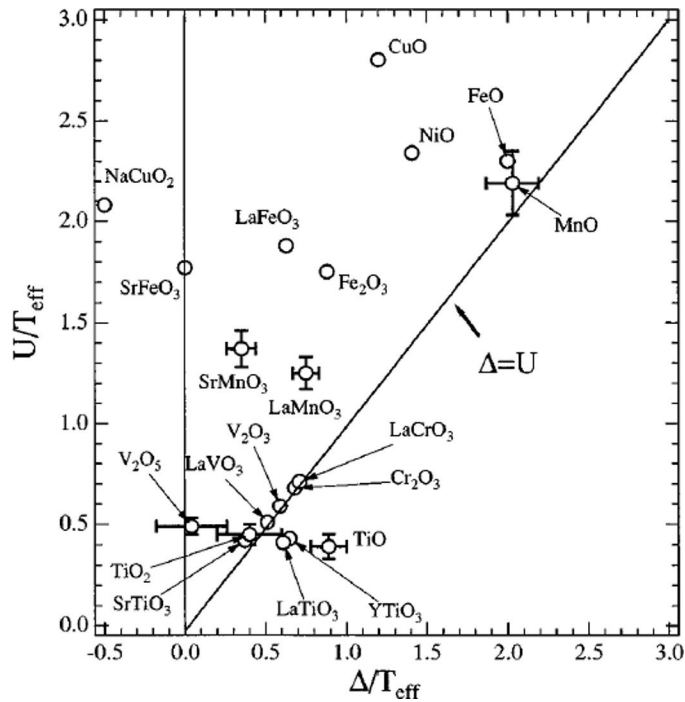


Fig. 2.3 Reproduced from Ref[40], the classic Zaanen-Sawatzky-Allen phase diagram plotting the boundary between CT-type and MH-type correlated insulators. The values of U and Δ are deduced from a combination of XPS and EELS data.

2.3 Field-Effect Switching in Correlated Insulators

Research on electric field-induced switching in correlated insulators dates back to early work performed on VO_2 around 1970[21, 41-43]. These reports find good agreement between experimental switching data and a thermal triggering process. In 1980, however, subsequent authors[44, 45] claim to find experimental data inconsistent with a simple thermal model. These authors report that the threshold power needed to trigger VO_2 's conducting state is independent of the ambient device temperature in the range between 220 K and 320 K, and they postulate that either channel inhomogeneities or an additional electronic effect is necessary to explain this and other trends. A similar controversy appeared at roughly the same time concerning threshold switching in amorphous chalcogenide semiconducting films[46]. Strong arguments were made for both an inhomogeneous thermal mechanism[47] and an electronic mechanism[48] that involves injection of charge carriers from the electrodes which then fill all the available trapping sites. To this author's knowledge, the argument was never definitively settled, and interest in the phenomenon appears to have faded in the 1980's and 1990's.

In 2000, work on electric field-induced switching in VO_2 re-emerged with a study[22] that claimed to show that the electric field-induced switching phenomenon in VO_2 was clearly Mott-Hubbard in origin, based on the speed with which the process occurs. Using electroformed channels of VO_2 , these authors reported that VO_2 can switch in 1.5 ns, given a sufficiently large driving voltage, whereas a simple thermal model of their device predicts a much slower 900 ns. Around the same time, reports of electrical switching in other materials started to appear as well, including V_2O_3 [25], $\text{Pr}_{1-x}\text{Ca}_x\text{MnO}_3$ [26], $\text{La}_{2-x}\text{Sr}_x\text{NiO}_4$ [27], and $\text{Sr}_n\text{CuO}_{n+1}$ [28]. These reports were then followed by many more studies on VO_2 [23, 49-52] that claimed to corroborate the electronic nature of the voltage-induced switching. Recently the phenomenon has been reported in the metal-insulator transition material Fe_3O_4 as well[29]. Nearly all of these studies, however, disregard the possibility of both channel inhomogeneities and feedback effects. Indeed, a more recent calculation[53] of switching times in microscale, single-crystal VO_2 devices has found that nanosecond-scale switching times are possible solely due to thermal effects, once self-accelerating effects are taken into account. The idea that thermal processes can play a very significant role in electric field-induced switching in

VO_2 is also supported by recent heating simulations that show appreciable temperature rises are possible using equilibrium sub-threshold input powers[54]. Because V_2O_3 is a clearer example of a Mott insulator and it also has much smaller leakage currents below the transition, we believe that its study will help to resolve the ongoing debate over the degree to which Joule heating plays a role in these types of switching experiments.

Recent theoretical work has also focused on the phenomenon of electric field-induced breakdowns in Mott insulators. It has been proposed[31, 55, 56] that in a strong enough electric field, electrons localized within a correlated insulator can tunnel across an energy barrier to doubly occupy a nearby site. The required Coulomb repulsion energy for this double occupation is gained directly from the electric field. This process would generate mobile electrons and holes within the system which, at a sufficient density, could trigger screening of the intersite Coulomb repulsion and cause an abrupt insulator-to-metal transition. Similar calculations have been put forward by other groups[30, 32] as well, and all appear to agree that a strong enough electric field should create dielectric breakdown in an ideal Mott insulator. There is uncertainty, however, over the required strength of this field and the nonequilibrium charge transport dynamics that lead to the phase transformation. The field strength required is extremely important, because regardless of whether or not an electronic breakdown mechanism exists in Mott insulators, the process will only be observable if a competing switching process does not occur first. Ionic breakdown, Zener breakdown, and a thermally triggered MIT should all occur at some electric field strength. In this dissertation we attempt to experimentally observe the dynamics of the field-induced switching process in V_2O_3 and identify the mechanism responsible.

2.4 Introduction to V_2O_3

2.4.1 Phase Diagram

Vanadium sesquioxide (V_2O_3) undergoes a first-order phase transition from a metallic paramagnet to an insulating antiferromagnet when cooled to below ~ 155 K. The change in resistivity across this MIT can be more than seven orders of magnitude, and the properties of the transition are sensitive to external pressure, stoichiometry, and chemical

doping[36, 57-59]. Some of these dependencies are revealed in V_2O_3 's classic phase diagram, shown in Fig. 2.4. Titanium doping and vanadium vacancies in bulk samples of $(Ti_xV_{1-x})_2O_3$ and $V_{2(1-y)}O_3$ both decrease T_{MIT} until the insulating phase is fully suppressed for $x > \sim 0.05$ and $y > \sim 0.01$ [36, 58, 59]. Alternately, chromium doping in bulk samples of $(Cr_xV_{1-x})_2O_3$ increases T_{MIT} and creates a paramagnetic insulating state near room temperature for $0.005 < x < 0.018$ [36, 57].

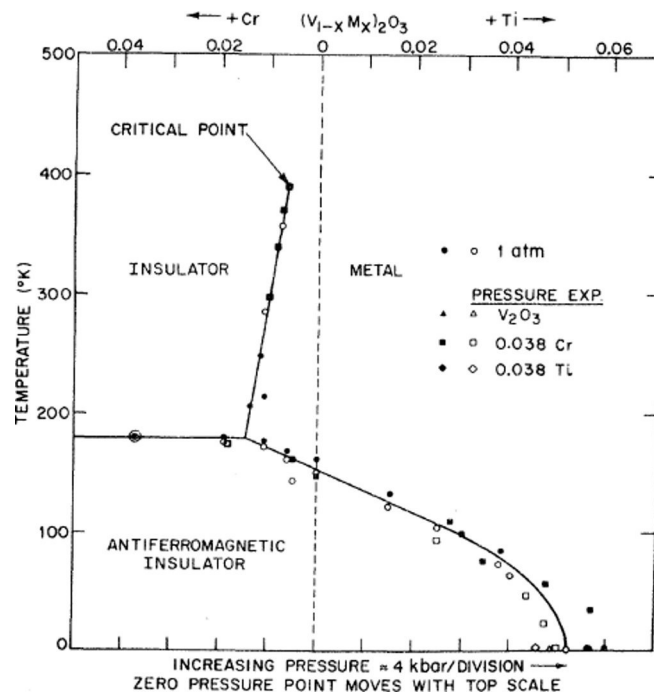


Fig. 2.4 Reproduced from Ref[36], the metal-insulator transition phase diagram of V_2O_3 showing the influence of temperature, pressure, and Cr and Ti doping on the MIT. The closed and open symbols are for increasing and decreasing pressure or temperature

Although precise understanding of V_2O_3 's rich phase diagram is still a topic of debate[60-62], the interplay between electron-electron interactions, band-width, and band filling, as described by the Mott-Hubbard model, is of critical importance. As can be seen in Fig. 2.4, increasing pressure stabilizes the metallic state of V_2O_3 . This makes sense for two reasons. First, in the Mott-Hubbard framework, a shrinking inter-atomic distance will mean more orbital overlap between adjacent vanadium atoms, which in turn

will give rise to a broader band-width W . Since the metal-to-insulator transition in V_2O_3 arises due to a competition between U and W , a large W will decrease the temperature at which a thermally expanding lattice crosses through the transition point. Second, there is a crystal symmetry change at the MIT temperature in V_2O_3 accompanied by a change in volume of about 1%, with the metallic phase having a smaller volume[63]. An increased external pressure should therefore stabilize the smaller crystal structure of the metallic phase.

Concerning V_2O_3 's response to chemical doping, one proposed explanation is that the stable 3+ chromium dopant sites act as a charged impurity whose d electrons are all tightly bound. This essentially deletes a state from the valence band, thereby narrowing it[36]. The case of titanium doping, however, is somewhat more complicated. As Mott[3] points out, the Ti^{3+} d orbitals will be slightly larger than the V^{3+} orbitals, therefore causing an increase in the band-width due to an increased orbital overlap, thus stabilizing the metallic state. However, more recent authors[4] claim that because the titanium sites can easily have a mixed valence between Ti^{3+} and Ti^{4+} , Ti-doping might be stabilizing the metallic state via a change in band filling. The effects of chromium doping and titanium doping therefore may be completely different in nature, with the former being a BC-MIT and the latter being a FC-MIT.

2.4.2 Crystal Structure of V_2O_3

At temperatures above the metal-to-insulator transition, V_2O_3 has a corundum-type structure identical to that of Al_2O_3 , as depicted in Fig. 2.5. This crystal structure can best be envisioned as two separate sublattices of oxygen and vanadium atoms. To a first approximation, the oxygen atoms form sheets of close-packed hexagonal lattices along the (0001) planes, and the vanadium atoms fill two-thirds of interstitial sites between these sheets. Each vanadium atom is therefore octahedrally coordinated within surrounding oxygen atoms. When cooling V_2O_3 to below the metal-insulator phase transition, this crystal structure undergoes a monoclinic distortion. Pairs of vanadium atoms dimerize in such a way as to double the unit cell. The volume of the low-temperature phase also expands by approximately 1%, as mentioned previously.

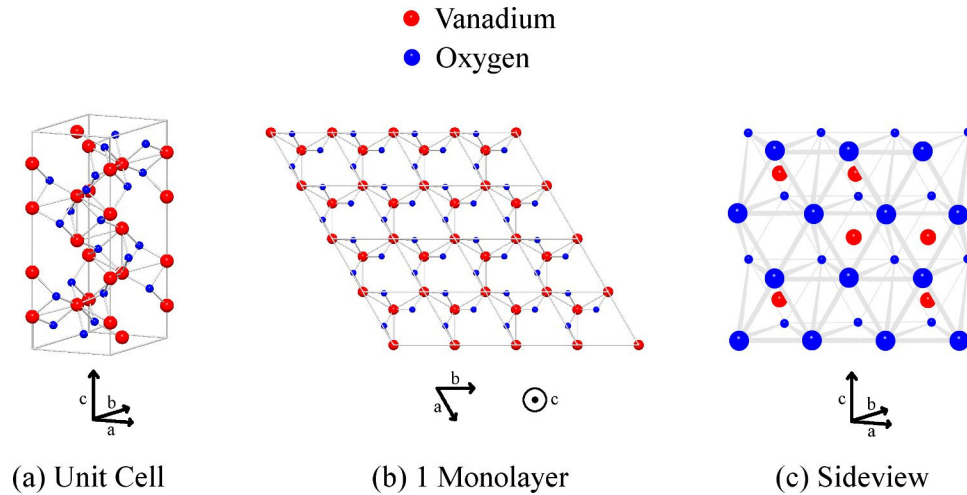


Fig. 2.5 Crystal structure diagrams for V_2O_3 . (a) The corundum unit cell of the high-temperature metallic V_2O_3 phase. (b) A topview along the c -axis showing 1 monolayer of vanadium and oxygen atoms. (c) A simplified sideview showing how two-thirds of the oxygen octahedra are occupied with vanadium atoms.

2.4.3 Band Structure

There remains a significant degree of controversy surrounding the mechanism responsible for the structural and electronic changes that happen in V_2O_3 (and also VO_2) at the metal-to-insulator transition temperature. It is not even known, for example, if the electronic transition induces the structural change or if the structural change induces the electronic transition. It is clear, however, that electron correlations play a key role. Electron-electron interactions included via LDA+U calculations have been shown to be necessary for recovering the basic electronic properties of the metallic and insulating phases of V_2O_3 [64, 65].

A one-band Hubbard model has been shown to be relatively successful in describing various properties of V_2O_3 's metal-insulator transition, such as optical conductivity[66]. Specifically, it has been proposed by Castellani[67-69] that the crystal field generated by V_2O_3 's oxygen sublattice splits the d band into a_{1g} and e_g orbitals, as seen in Fig. 2.6(a). Since each vanadium atom has three electrons involved in covalent $2p$ orbitals with the surrounding oxygen atoms, this would leave one d electron in a fully-filled a_{1g} band and a second d electron in a half-filled band composed of two degenerate e_g orbitals. The Hubbard model can then be applied to this singly-occupied, half-filled e_g

band to explain the existence of V_2O_3 's 0.6 eV band gap at low temperature due to correlation effects. It should be noted that this simple description ignores important orbital ordering effects associated with the monoclinic structural distortion that occurs during V_2O_3 's metal-insulator transition[70, 71].

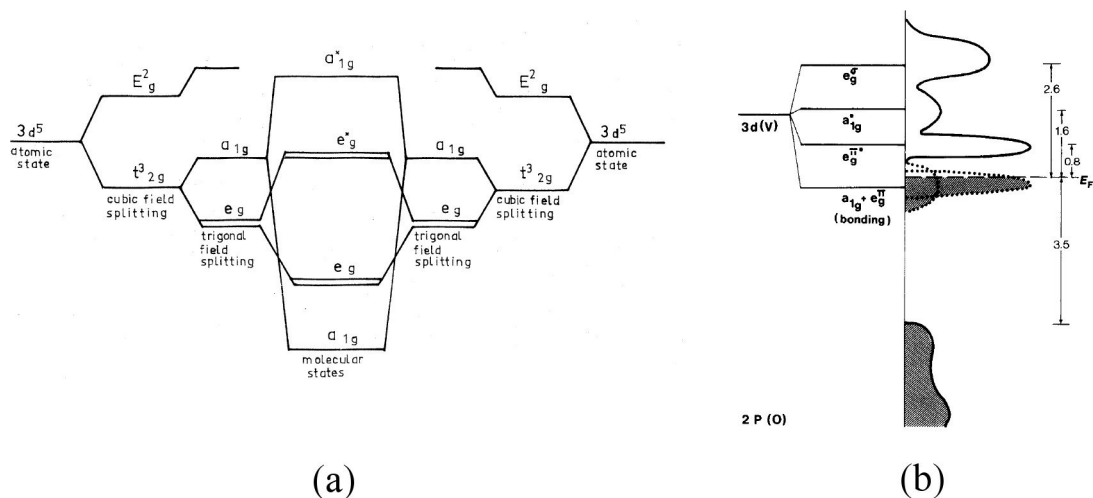


Fig. 2.6 Two competing energy level schematics for V_2O_3 . (a) A prediction of degenerate e_g orbitals reproduced from references[67-69]. (b) An empirically determined prediction of a_{1g} and e_g hybridization reproduced from reference[72].

Before Castellani's description, an alternate model of V_2O_3 's band structure was posited by Goodenough[73] and later supported by XPS experiments[72, 74]. This model, seen in Fig. 2.6(b), is similar to Castellani's model with the difference that the a_{1g} and e_g orbitals overlap in energy. Note that the 2p orbital lies several electron volts below the vanadium 3d bands, consistent with V_2O_3 's description as an MH-type correlated insulator rather than a CT-type.

2.4.4 Other Phases of Vanadium Oxide

V_2O_3 is just one of many different phases of vanadium oxide. These phases can be classified as either Magneli or Wadsley phases. The Magneli phases have the formula V_nO_{2n-1} , including VO, V_2O_3 , V_3O_5 , V_4O_7 , V_5O_9 , etc., and terminating with VO_2 for $n = \infty$. The Wadsley phases have the formula $V_{2n}O_{5n-2}$, including V_2O_3 , V_4O_9 , V_6O_{13} , etc., and terminating with V_2O_5 for $n = \infty$. Remarkably, these phases can accommodate a wide range of different vanadium valences: V^{2+} in VO, V^{3+} in V_2O_3 , V^{4+} in VO_2 , and V^{5+} in V_2O_5 . Even more remarkably, many of these phases undergo metal-insulator transitions as a function of temperature. For nice discussions of some of these metal-insulator transitions, we refer the interested reader to references [75] and [76]. Interestingly, V_2O_3 is the only vanadium oxide that undergoes a metal-insulator transition at its Neel temperature, which has long been taken as further evidence of the Mott-like nature of the transition. Fig. 2.7 shows a binary phase diagram of all of the various vanadium oxides plotted against their oxygen content. It should be immediately obvious that the growth of any particular vanadium oxide might not be an easy task. The growth temperature, the oxygen pressure, and the underlying substrate must all be very carefully chosen to avoid contamination by other phases. Furthermore, post-deposition characterization must be performed to ensure that the material does not change phase upon exposure to the atmosphere or during any characterization or device fabrication procedures. Fortunately, as one of the lowest oxidation states of the various vanadium oxide, it turns out V_2O_3 is particularly well-suited for MBE deposition. It is also quite stable in air.

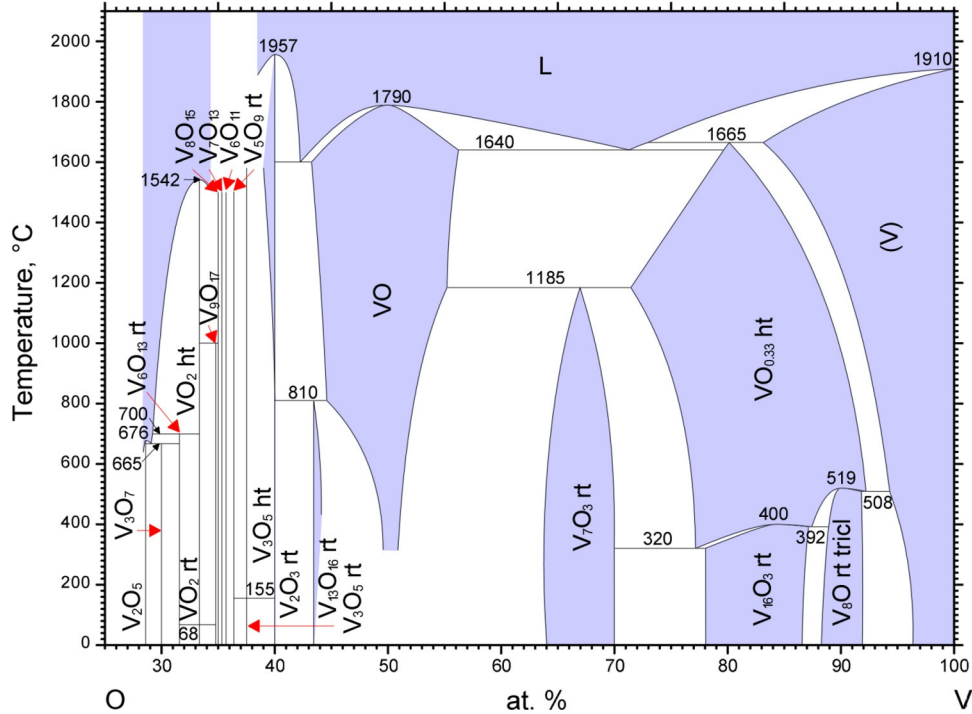


Fig. 2.7 Reproduced from Ref[77], the stoichiometric phase diagram of the various vanadium oxides. V_2O_3 is one of the lowest oxidation state phases, apart from VO and $V_{13}O_{16}$.

2.5 Notes on High-Field Transport in Insulators

2.5.1 Dielectric Breakdown

Under a large enough electric field, any material will undergo a structural or electronic breakdown. Even the vacuum of space, for example, should spontaneously separate into electron-positron pairs and conduct electricity when the field strength reaches a value $E_{Th} \approx 2 \times 10^{17} V/m$. This is known as a Schwinger[78] breakdown process, and it is roughly defined by the condition $E_{Th} \lambda_c e \approx m_e c^2$, where λ_c is the Compton wavelength of an electron. Of course, such strong electric fields are not achievable in the laboratory, and even the strongest dielectrics such as MgO or SiO₂ break down at an electric field strength of approximately $E_{Th} \approx 1 \times 10^9 V/m$.

Two common breakdown mechanisms in insulators are the Zener[79] breakdown and the ionic breakdown. A Zener breakdown is a nondestructive process that is due to the quantum mechanical tunneling of carriers through a material's band gap. An ionic breakdown is a destructive process in which individual atoms ionize and undergo

electromigration. In air, ionic breakdown occurs at roughly 3×10^6 V/m. For this reason, electric field experiments searching for new Mott-related switching effects must necessarily be done in vacuum.

In correlated insulators that display temperature-driven metal-insulator transitions, two additional breakdown mechanisms are possible. First, a thermal breakdown caused by the Joule heating from leakage current can trigger the metal-insulator transition. Second, as discussed in Section 2.3, a Mott-related breakdown is predicted to be possible due to carrier injection from the electrodes or due to the spontaneous generation of an electron/hole, both of which can alter the critical integer filling that is required for the gridlocked insulating state of a Mott insulator.

2.5.2 Poole-Frenkel and Schottky Emission

Prior to any electric field-induced breakdown in an insulator, there is universally a non-linear relationship between the subthreshold leakage current I and the applied electric field E . The nature of this relationship can reveal information about the conduction mechanism. For example, as discussed in Ref[80], a relationship of $\ln(I) \propto E^2$ suggests phonon-assisted tunneling is responsible, and a relationship of $\ln(I) \propto \sqrt{E}$ suggests Poole-Frenkel emission[81] is responsible. A schematic of these two conduction mechanisms, as well as simple direct tunneling, is presented in Fig. 2.8. Later in this dissertation, we will show that the subthreshold current-voltage relationship that we observe for our V_2O_3 nanostructures is extremely well-described by Poole-Frenkel emission.

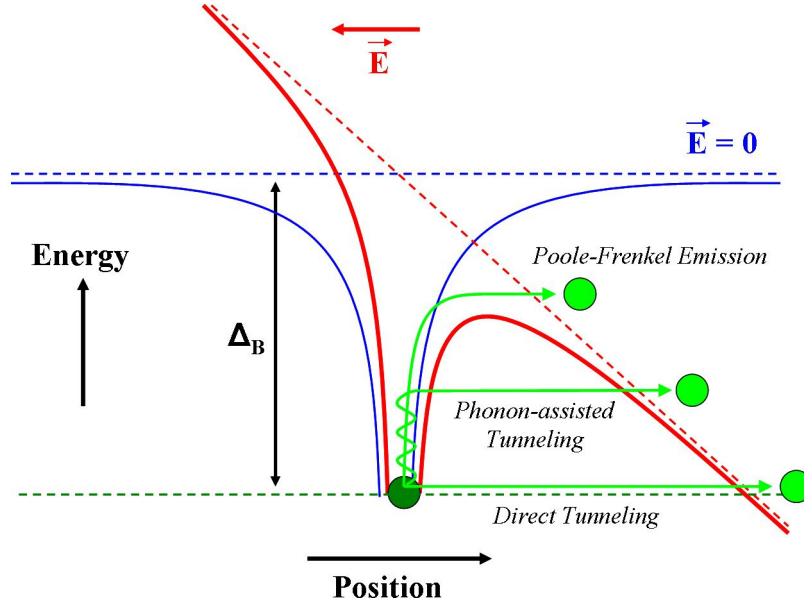


Fig. 2.8 A figure, reproduced from Ref[80], showing three different mechanisms of high-field conduction in an insulator: Poole-Frenkel emission, phonon-assisted tunneling, and direct tunneling.

In Poole-Frenkel emission, a strong electric field tilts the energy landscape within a material and effectively decreases the trapping potential Δ_B that is responsible for holding the electrons in place. It is a relatively straightforward algebraic exercise to show that this decrease in barrier height will be proportional to the square root of the electric field when starting with a $1/r$ Coulombic trapping potential. Because the high-field leakage current should be proportional to the thermally-assisted escape probability which is in turn proportional to the exponent of the trapping potential, this leads to the relationship $\ln(I) \propto \sqrt{E}$. Eq. 2.2 shows a more formal presentation of the relationship between Poole-Frenkel current and electric field[82, 83]:

$$I_{PF} = Ae^{\frac{-(\Delta_B - \beta_{PF} \sqrt{E})}{kT}}, \text{ where } \beta_{PF} = \left(\frac{e^3}{\pi \epsilon_r \epsilon_0} \right)^{\frac{1}{2}}. \quad (2.2)$$

As discussed in Ref[82], there is disagreement over whether I or I/V should be proportional to electron escape probability. Various authors use fits with slight

modifications such as this to obtain the Poole-Frenkel exponent. These differences might partially stem from variations in electron mobility. In a high-mobility system, an escaping electron should travel a distance proportional to the electric field, and therefore the conductivity, or I/V , should be proportional to escape probability. In a low-mobility system, an escaping electron will simply be recaptured at the next trapping site, and therefore only the current should be proportional to the escape probability. Note that the derivation of the Poole-Frenkel relationship inherently assumes that the participating electrons are spatially localized at charged defects, not in bands. This conduction model is frequently applied to amorphous semiconductors and insulators, but it has also often been cited as the conduction mechanism responsible for leakage currents in VO_2 [84-86].

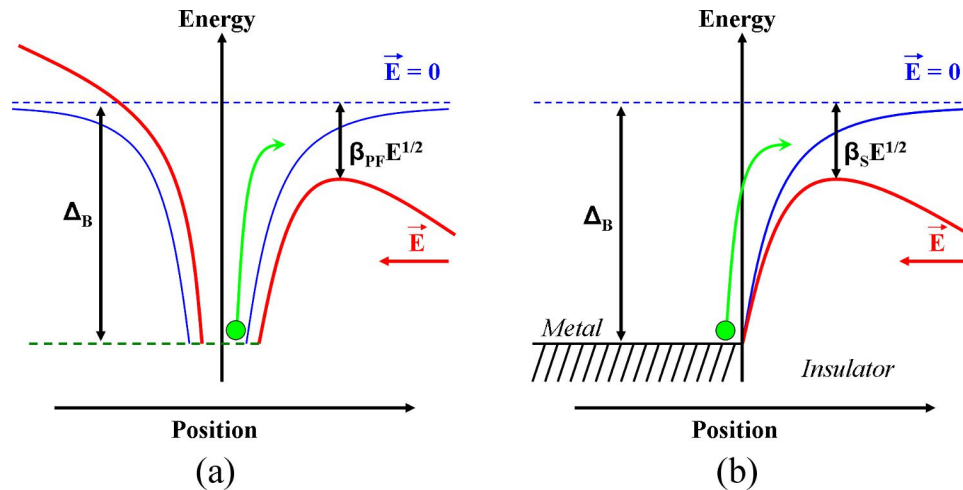


Fig. 2.9 A comparison of the Poole-Frenkel and Schottky emission phenomena. In both cases, the energy barrier responsible for blocking conduction is lowered by a factor proportional to the square root of the applied electric field.

As a caveat, when a material displays an $\ln(I) \propto \sqrt{E}$ relationship consistent with the Poole-Frenkel conduction mechanism, it is notoriously difficult to distinguish this from Schottky Emission[87], which also has the same relationship. The reason for the similarity is shown in Fig. 2.9. In both cases, the barrier that must be overcome for

conduction is lowered by an amount proportional to the square root of the electric field. In the case of Poole-Frenkel emission, this barrier is a trapping potential responsible for localizing electrons. In the case of Schottky emission this barrier is essentially the band gap of the material.

Chapter 3

EXPERIMENTAL PROCEDURES

3.1 Introduction

In this chapter, we provide an overview of the experimental apparatus and procedures used in this work. First we discuss our film growth equipment and characterization methods. Next, we present a detailed description of the process used to fabricate devices from these films. Last, we describe the equipment used to electrically measure the direct-current and high-speed switching characteristics of the V_2O_3 devices.

3.2 Film Deposition

The deposition of our V_2O_3 films was performed at the IBM Almaden Research Center in San Jose, CA using an ultra-high vacuum (UHV) molecular beam epitaxy (MBE) chamber. This cylindrical chamber, a schematic of which is pictured in Fig. 3.1, was approximately 34 inches in both lateral diameter and height, and it was equipped with sample rotation, three silicon carbide heater-based furnaces, *in situ* RHEED analysis, two electron-beam evaporation guns, sixteen water-cooled Knudsen cells, four oxygen and nitrogen plasma sources, six quartz crystal microbalances, and an ion gauge and residual gas monitor for measuring gas pressures within the chamber. These tools were arranged into six independent deposition “clusters,” or stations. The source-to-sample distance, defined by the focal point of each of the effusion cell clusters and the RHEED beam geometry, was approximately 18 inches. The sample carriers were loaded into wafer holders and robotically transferred into the chamber via an external load lock. The wafer holders were designed for 1” round wafers, but sample inserts were commonly used to accommodate smaller wafers. A turbopump, a helium cryopump, and a liquid nitrogen-filled cryopanel were all used in combination to pump the chamber. The unbaked chamber base pressure was approximately 1×10^{-9} Torr, and baking the chamber for several days improved this to as low as 5×10^{-11} Torr. Most of the vanadium oxide growth presented in this thesis was performed at the unbaked base pressure of 1×10^{-9} Torr.

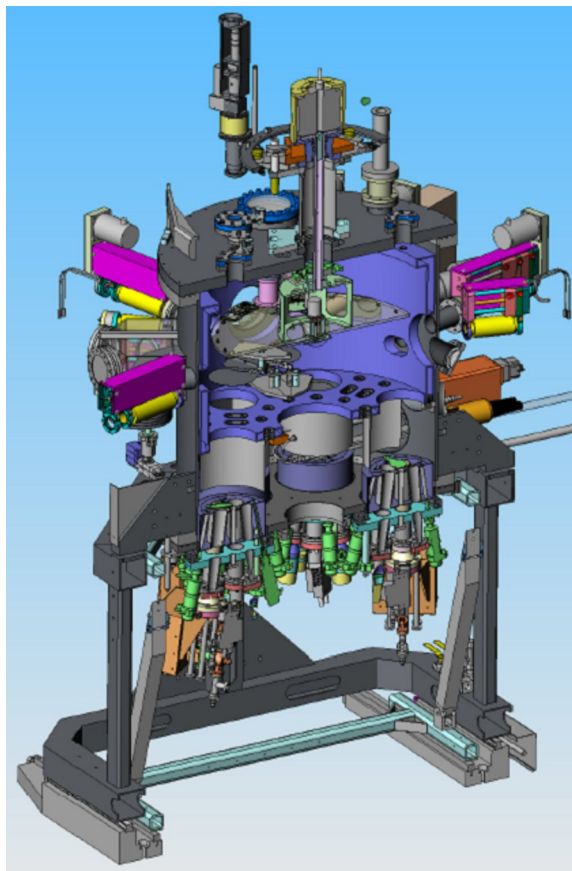


Fig. 3.1 A cross-sectional schematic of the MBE deposition chamber. The sample platter and two of the effusion cell clusters can be easily seen. The blue area is the liquid nitrogen cryopanel. Various measurement tools including RHEED imaging and QCM flux monitors are located around the outside of the chamber. For scale, the diameter of this cylindrical chamber is approximately 34 inches.

During our work on V_2O_3 , one of the deposition clusters was fully dedicated to vanadium oxide growth and equipped with four high-temperature Knudsen cells and a quartz cavity oxygen plasma source, both purchased from the company Addon. Solid pellets of 99.8% purity served as the vanadium source, and were vaporized within a molybdenum-lined Knudsen cell held at temperatures between 1700 to 1800 °C. The plasma source operated at 270 watts of forward power and was supplied with a fixed flow of ultra high purity oxygen through a differentially pumped inlet. Molecular oxygen pressures were monitored during growth with a residual gas analyzer located near the sample, and the oxygen flow rate into the plasma cavity was varied so as to give chamber pressures during growth in the range between 1×10^{-8} and 5×10^{-7} Torr. Gradual increases

and decreases in the oxygen chamber pressure as large as 10% were commonly observed during film growth, likely due to gettering effects. All oxygen pressures reported in this dissertation are values recorded at the end of deposition. During deposition, the samples were heated to growth temperatures ranging between 600 and 850 °C. Heating and cooling was carried out in the absence of oxygen at rates not exceeding 15°C/min.

One of the most challenging aspects of this method for depositing V_2O_3 was that the Knudsen cell filaments were vulnerable to breaking at the very high temperatures between 1700 and 1800 °C required for vanadium sublimation. We found that the tungsten filaments in our Addon Knudsen cells typically only survived between 60 and 100 hours of deposition before breaking, despite being rated to operate at 2000 °C. To avoid having to frequently vent the chamber, we often loaded multiple cells with vanadium before pumping out the chamber to begin deposition, and switched from cell to cell as the filaments broke. For future MBE deposition of V_2O_3 , electron beam evaporation would be our preferred method. The downside of electron beam evaporation, however, is that co-evaporation of multiple materials is more difficult, and the deflection coils used for rastering the electron beam can degrade the RHEED imaging.

The MBE chamber we used to deposit V_2O_3 was part of a much larger multi-chamber deposition system, shown in Fig. 3.2, that consisted of a variety of chambers capable of magnetron sputtering, ion beam sputtering, pulsed-laser deposition, and surface analysis. For our work on V_2O_3 , in addition to the MBE chamber we used the surface analysis chamber to collect X-ray photoelectron spectroscopy, and we used magnetron sputtering to deposit 1 nm capping Al_2O_3 capping layers on V_2O_3 prior to device fabrication.

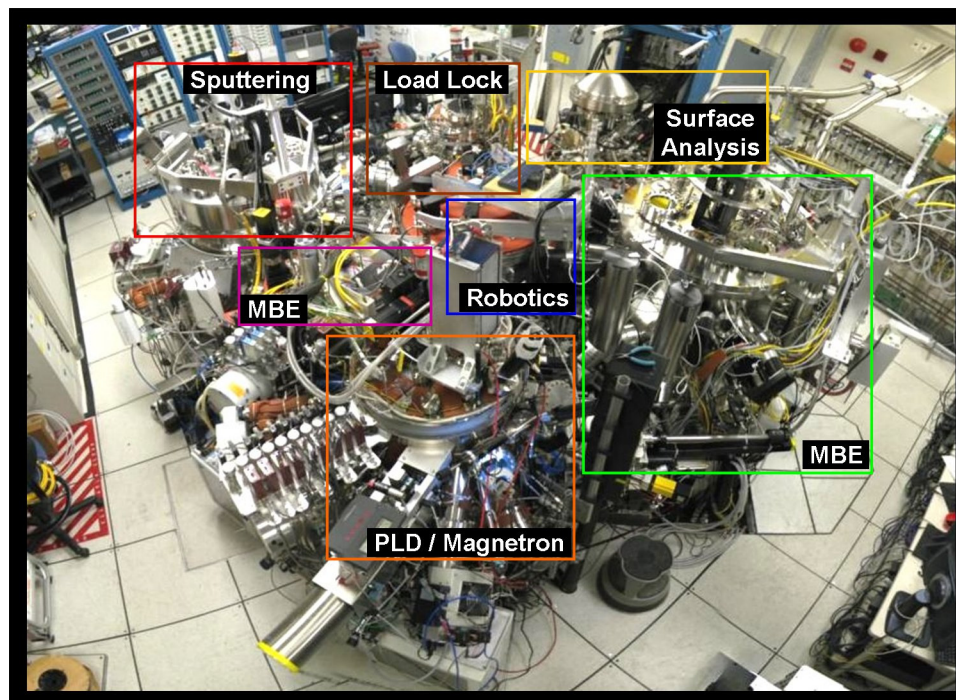


Fig. 3.2 A picture of our multichamber deposition tool. The V_2O_3 films were deposited in the large MBE chamber on the right-hand-side labeled in green. All samples were inserted into the various chambers via the central robotics chamber and a common load lock.

3.3 Film Characterization

A wide array of different film characterization techniques were employed in this work including X-ray diffraction (XRD), Rutherford backscattering (RBS), reflection high-energy electron diffraction (RHEED), transmission electron microscopy (TEM), atomic force microscopy (AFM), X-ray photoelectron spectroscopy (XPS), and four-point resistivity measurements. All of these techniques are very comprehensively discussed elsewhere, so we limit our brief discussion here to the specific ways in which these techniques were applied in this work.

3.3.1 XRD

Perhaps the most useful and versatile tool at our disposal for film characterization is X-ray diffraction (XRD). XRD can be used for measuring crystal lattice parameters, strain relaxation, film thickness, grain size, roughness and texture, among other things. In this work, we have used XRD primarily for measuring the out-of-plane d -spacing

values of our V_2O_3 thin films by performing symmetric θ - 2θ scans. The value of this d -spacing, compared to bulk values for V_2O_3 , tells us about the level of macrostrain present in our films. This measurement is based on the constructive interference of the X-ray waves scattering off of atomic planes within the crystalline lattice. According to Bragg's law, this constructive interference will occur when the angle of incidence and the angle of reflection are both equal to θ , and θ satisfies the equation

$$n\lambda = 2d \sin(\theta), \quad (3.1)$$

where n is a positive integer representing the order of the refraction, λ is the wavelength of the X-ray source, and d is the distance between planes that must be perpendicular to the vector difference between the incoming and outgoing X-ray momentum vectors. This simple rule allows us to convert measured XRD spectra, traditionally plotted as a function of 2θ , into a physically significant number for the spacing between sets of atomic planes in our films. The width of the XRD peaks also has physical significance and the full-width at half-maximum (FWHM) of the peaks can tell us information about film thickness, crystallite size, mosaic broadening and microstrain. We will address these latter issues in more detail when we encounter them in Chapter 5.

3.3.2 RBS

Rutherford backscattering is a technique for deducing the elemental composition of a material by bombarding it with high-energy alpha particles, or helium nuclei. Each individual alpha particle that collides with an atomic nucleus in the material being investigated will scatter off-axis to some angle θ . Conservation of energy and momentum dictates if the collision is elastic, the resulting energy of the alpha particle will be $E_1 = kE_0$, where k is known as the kinematical factor and it is given by the following expression:

$$k = \left(\frac{m_1 \cos \theta \pm \sqrt{m_2^2 - m_1^2 \sin^2 \theta}}{m_1 + m_2} \right)^2. \quad (3.2)$$

E_0 is the incident beam energy, m_1 is the mass of the alpha particles in the incident beam, m_2 is the mass of the scattering element, and θ is the scattering angle to the detector as measured in the laboratory's frame of reference. Therefore, by measuring the energy of the alpha particles deflected to a detector a given value of θ , one can solve for the mass of the scattering element. In this way, the energy spectrum of the scattered alpha particles provides a direct measurement of the elemental composition of the material being investigated. It should be noted that an additional thickness-dependent energy loss occurs due to collisions with electrons in both the material being investigated and also a protective coating on the detector. We use this powerful technique to roughly obtain the composition and thickness of our films, and also to identify any possible sources of contamination.

3.3.3 RHEED, TEM and AFM

Reflection high-energy electron diffraction (RHEED) is an *in situ* technique for monitoring crystal structure and surface texture before, during, or after a deposition. The measurement works by directing a columnated beam of high-energy electrons (in our case 35 keV) at the sample with a low angle of incidence (in our case 3 degrees). The electrons scatter off individual atoms on the crystalline surface of the film and create an interference pattern that is imaged on a phosphor screen located on the opposite side of the vacuum chamber using a standard visual light camera. The interference pattern allows us to deduce information, in reciprocal space, about the crystalline properties of the film or substrate in a manner analogous to X-ray diffraction. If the film is amorphous, only a diffuse background will appear. If the film is polycrystalline, a ring-like pattern will form. And if the film is single-crystalline, or highly textured, a first order Laue circle of spots will be visible, and any surface roughness or lateral decoherence will cause the spots to smear into streaks, or rods. The structure of these spots and rods provides valuable real-time information about a film's phase, epitaxy, strain evolution, and roughness during the growth process. It is also possible to use RHEED to gain information about the growth model. If the reflected specular spot oscillates in intensity during the growth process, it is a sign of layer-by-layer, with each

completed layer enhancing the reflection of the RHEED beam onto the phosphor screen. If oscillations are not observed, either island-like growth or step-flow growth might be occurring, and these two modes can be easily distinguished from one another by *ex situ* atomic force microscopy measurements of the film surface.

Transmission electron microscopy (TEM) and atomic force microscopy (AFM) are both imaging techniques that can be used to generate real-space images of a film's structure. TEM uses electron beam diffraction, and atomic force microscopy measures the changes in resonance of a nanometer-sized tip due to Van der Waals forces while being dragged across the surface of a wafer. We use cross-section TEM to look for grain structure and also identify the epitaxial relationship between our V_2O_3 films and the α - Al_2O_3 substrate underneath, whereas we use AFM primarily to measure the surface roughness of our films for various deposition conditions.

3.3.4 XPS

X-Ray photoelectron spectroscopy (XPS) is a technique for measuring a material's electronic structure and chemical composition. In XPS, an X-ray source is used, in vacuum, to excite bound electrons within a material into free space, where they can be collected in an energy-sensitive detector. We use an aluminum anode as the excitation source, which generates electrons at a fixed energy of 1486.6 eV, and for detection we use a Thermo Fisher Scientific hemispherical analyzer that can be swept between 0 and 1500 eV. The result of a scan is a spectrum of peaks located at various kinetic energies (KE) that correspond to atomic orbitals of various binding energies (BE) within the material according to the following simple energy conservation equation:

$$E_{Source} = KE + BE . \quad (3.3)$$

Because every element has a unique fingerprint of atomic binding energies, XPS can be used to identify chemical composition and stoichiometry. To do this for a compound with an arbitrary number of different elements, one must simply integrate an intense core level peak for each of the element, divide the result by a known atomic

sensitivity factor, and calculate the compositional fraction of that element according to the following equation:

$$f_x = \frac{Area_x / ASF_x}{\sum_i Area_i / ASF_i}. \quad (3.4)$$

In addition, the core level binding energies of a material can shift with atomic valence due to shielding effects. This is a second way in which the stoichiometry of a material can be identified. We use both of these XPS techniques to confirm the composition and phase of our V_2O_3 thin films.

3.3.5 Four-Point Resistivity Measurements

Ultimately, the best qualification of high-quality V_2O_3 films is perhaps the strength and transition temperature of its metal-insulator transition. To study this, we wirebond contacts onto our V_2O_3 films in the classic four-point geometry and load them into a Quantum Design PPMS cryostat. Fig. 3.3 shows a picture of this cryostat along with a schematic of a typical wirebonding configuration. Once in the cryostat, the sample temperature is swept between 300 K and 50 K and back again to 300 K at a sweep rate of 5 K/min, and Keithley source-measure units are used to apply a current to the outer two contacts and measure a voltage and the inner two contacts. The applied voltages and currents can then be converted into a film resistivity using the following equation:

$$\rho = \frac{\pi t V}{\ln(2) I}, \quad (3.5)$$

where t is the film thickness, I is the voltage sourced across the outer two leads, and V is the voltage measured across the inner two leads. This formula works best when the wafer thickness is less than half the probe spacing, the four probes are not located near a wafer edge, and the probes are spaced far enough apart that the probe size can be neglected.

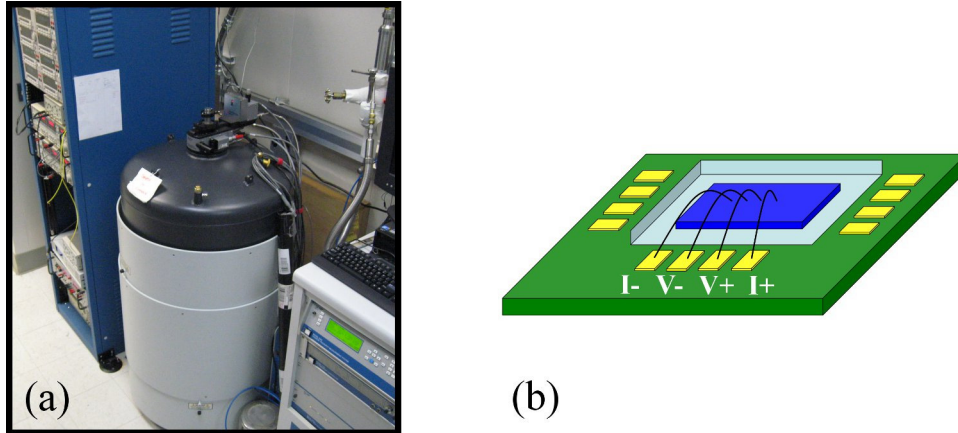


Fig. 3.3 (a) A picture of the Physical Property Measurement System (PPMS) cryostat system by Quantum Design that we used for 4-point resistivity measurements of V_2O_3 . (b) A schematic of the sample puck showing a typical wirebonding arrangement.

The huge resistivity change that occurs as the samples are cooled presents a small technical challenge. It was not feasible to measure a resistivity change eight or nine orders in magnitude with either a fixed current or a fixed voltage across the outer two leads using the electronics available to us, so instead we sourced 10 V across the outer two leads with a current limit of 1 mA. In V_2O_3 's metallic state, the measurement was therefore current-limited, and in V_2O_3 's insulating state, the measurement smoothly transitioned to a voltage-limited regime. This technique essentially expands the resistivity measurement range by applying a larger voltage when the resistance is higher and a lower voltage when the resistance is lower, and it relies on having a current-voltage dependence that is linear in the range of applied voltages.

3.4 Device Fabrication

We used a combination of electron beam and optical lithography to pattern coplanar, two-terminal nanodevices onto the surface of V_2O_3 films with optimized temperature-driven metal-insulator transitions. A computer-assisted drawing of the V_2O_3 nanostructure design can be seen in Fig. 3.4. The final device consisted of four major components: an isolated mesa of V_2O_3 , insulating pads of Al_2O_3 to avoid contact with potentially damaged V_2O_3 sidewalls, a gold nanogap structure on the surface of V_2O_3

with electrode separations ranging between 75 nm and 1200 nm, and large contact pads used for landing both direct-current and high-speed probes onto the device for electrical testing.

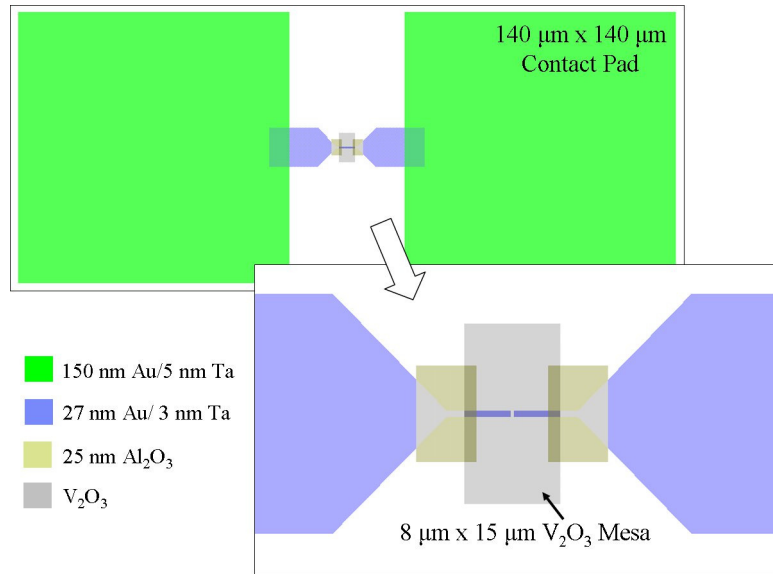


Fig. 3.4 The V₂O₃ nanogap design. The top image shows two large contact pads used for landing probes, and the zoomed-in image shows the small, active area of the device between the two electrodes. Also visible are the Al₂O₃ pads used to isolate the contact lines from the sidewalls of the V₂O₃ mesa, which can become conducting during the mesa structure etch. Not visible is an adjacent grounding strip used during the high-speed transmission measurements.

There are three reasons for making such small devices. The first is that it requires a very narrow electrode gap to apply large electric fields ($\sim 10^7$ V/m) using a modest voltage. The second is that a small active volume of V₂O₃ will dissipate heat very quickly, hopefully minimizing the effects of Joule heating. And the third reason is that a smaller cross-sectional area of the device will minimize the possibility of inhomogeneous current flows which can undermine the accuracy of Joule heating estimations. The nanogap contacts are deposited onto the surface of the V₂O₃, rather than etched in and refilled, because the high resolutions involved require a very thin electron beam lithography resist which has a very limited etching budget.

The procedure that we used to fabricate two-terminal V_2O_3 nanogap devices consisted of four main parts: A) mesa structure definition, B) isolation pad deposition, C) nanogap deposition, and D) contact pad deposition. Fig. 3.5 shows a schematic of the individual steps involved in each of these parts, including cross-sectional and top-view diagrams of the device at each stage. In the following sections, we describe the steps of this procedure in more detail.

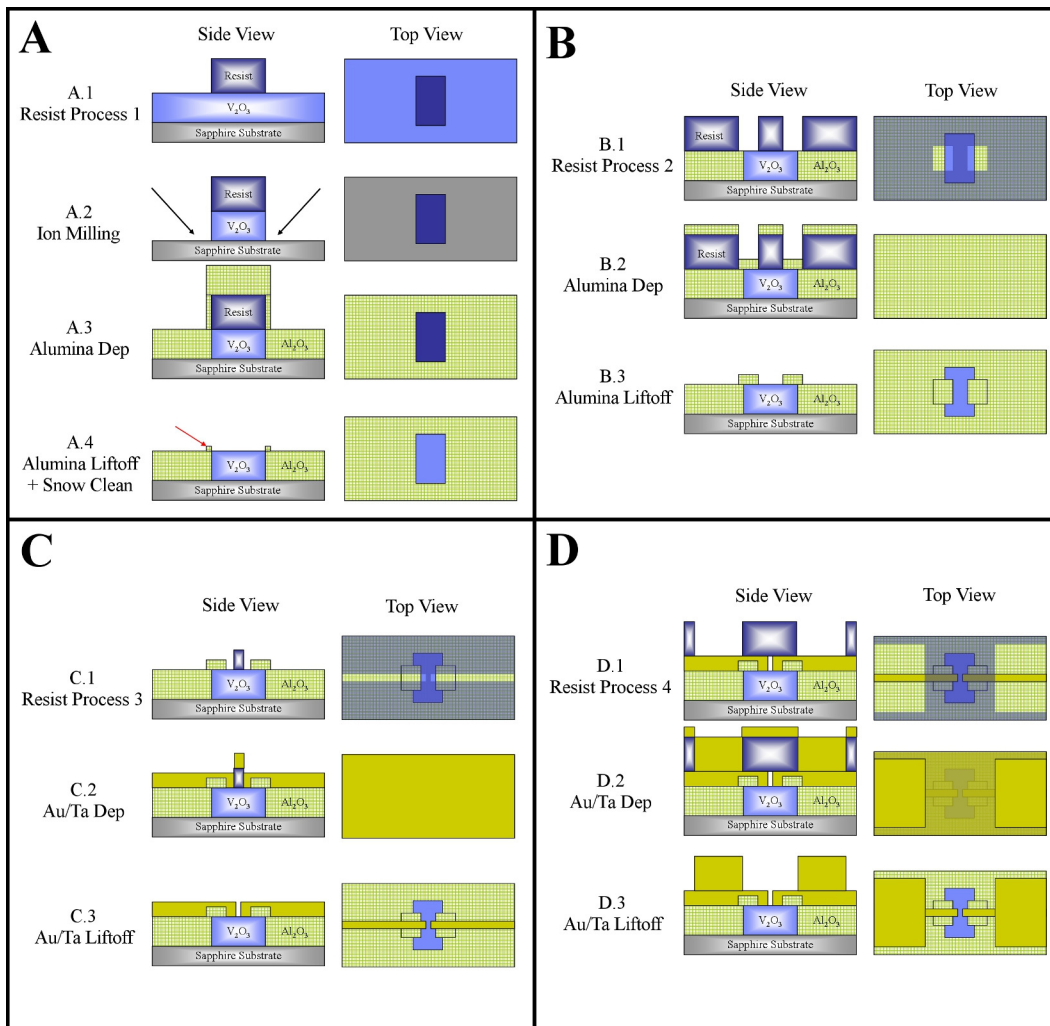


Fig. 3.5 The device fabrication process. Step A is the mesa structure definition, Step B is the isolation pad deposition, Step C is nanogap deposition, and Step D is the contact pad deposition. Steps A, B and C are patterned with electron-beam lithography, and step D is patterned with optical lithography.

3.4.1 Mesa Structure Level

Electron beam lithography (A.1) was used to pattern $8\ \mu\text{m} \times 15\ \mu\text{m}$ rectangular mesas into a bilayer coating of 150 nm of the negative e-beam resist HSQ and 200 nm of Duramide. After development of the HSQ, the pattern was transferred to the Duramide layer by an oxygen plasma etch. The exposed areas of V_2O_3 were then etched at an angle of 45° by Ar-ion milling (A.2) all the way down to the sapphire substrate, with a 10% over-etch. SIMS was used to monitor the vanadium signal during this etch and identify the endpoint. The removed volume was then refilled, in the same process chamber, with an equal amount of Al_2O_3 deposited by IBD (A.3). The purpose of this step is to maintain a flat, planar surface upon which the thin nanogap contact lines can be deposited without a break in continuity. Finally, liftoff (A.4) was performed in an ultrasonic bath of NMP held at $60\ ^\circ\text{C}$. The Al_2O_3 refill process left significant ‘fences’ around the edges of the V_2O_3 mesas that could break the continuity of the nanogap metal contacts. CO_2 snow cleaning was used to reduce the height of these fences as much as possible.

3.4.2 Isolation Pad Level

A second electron beam lithography step (B.1) was used to pattern $5\ \mu\text{m} \times 8\ \mu\text{m}$ rectangular holes into approximately 100 nm of the positive e-beam resist PMMA. After development, a brief plasma etch was used to clean the surface prior to the alumina deposition. Approximately 25 nm of alumina were deposited (B.2) into the PMMA holes by IBD to create an isolation barrier between the damaged V_2O_3 sidewalls and the nanogap contact lines deposited in the next step. If any thicker than 25 nm, these pads will create step edges on the surface tall enough to break the continuity of the nanogap contact lines. For liftoff (B.3), the wafer was soaked in acetone for approximately 1 hour, followed by a snow clean, and then a dip in an ultrasonic bath of acetone for approximately one minute.

3.4.3 Nanogap Level

A third electron beam lithography step (C.1) on a thinned PMMA resist was used to pattern the fine nanogap metal contact level. The resolution of this lithography was optimized with respect to beam dosage and resist thickness, as this is the most critical part of fabrication process. After development, a brief plasma etch was used to clean the surface. At this point, the wafers were loaded into the etch/dep process chamber. There, a 60 second Ar-ion mill angled at 10° from the surface normal was used to further clean the surface. Next, 3 nm of tantalum followed by 27 nm of gold were deposited (C.2) into the open trenches to form the metallic nanogaps on the surface of the V_2O_3 mesas. The interfacial tantalum layer was used for increased adhesion. For liftoff (C.3), the wafer was soaked in acetone for approximately 1 hour, followed by a few minutes of ultrasonic treatment. It was important not to perform any snow cleaning at this point, or any later point, as it could delaminate the fragile fine contacts from the surface of the wafer.

3.4.4 Contact Pad Level

Contact-mask optical lithography (D.1) was used to pattern holes for the large contact pads into a bilayer resist of SPR670-1.3 and PMMA. A grounding strip, not pictured in Fig. 3.4 and Fig. 3.5, was also placed next to the devices to accommodate high-speed testing. Following development and a brief ion mill cleaning, 5 nm of tantalum followed by 150 nm of gold were deposited (D.2) into the exposed areas. Liftoff (D.3) was performed by a 130° post-deposition bake for a few minutes, an hour-long soak in acetone, and finally three minutes of ultrasonic treatment in acetone.

3.4.5 Completed Structures

Fig. 3.6 shows a fully processed 1" wafer, at various levels of magnification. Each wafer has approximately 400 independent devices and groundlines, as can be seen in Fig. 3.6(b) and Fig. 3.6(c). Although a range of devices were made between 75 nm and 1200 nm, the most important devices for testing turned out to have nominal gap sizes of 75 nm, 125 nm, 175 nm and 225 nm, as measured by scanning electron microscopy (SEM). Devices with larger gaps required a much higher switching voltage that commonly broke the device or caused large irreversible changes. Although even in the smallest devices, it was not uncommon to see the first switching event occur with a forming voltage that was up approximately 10% larger than all subsequent threshold voltages.

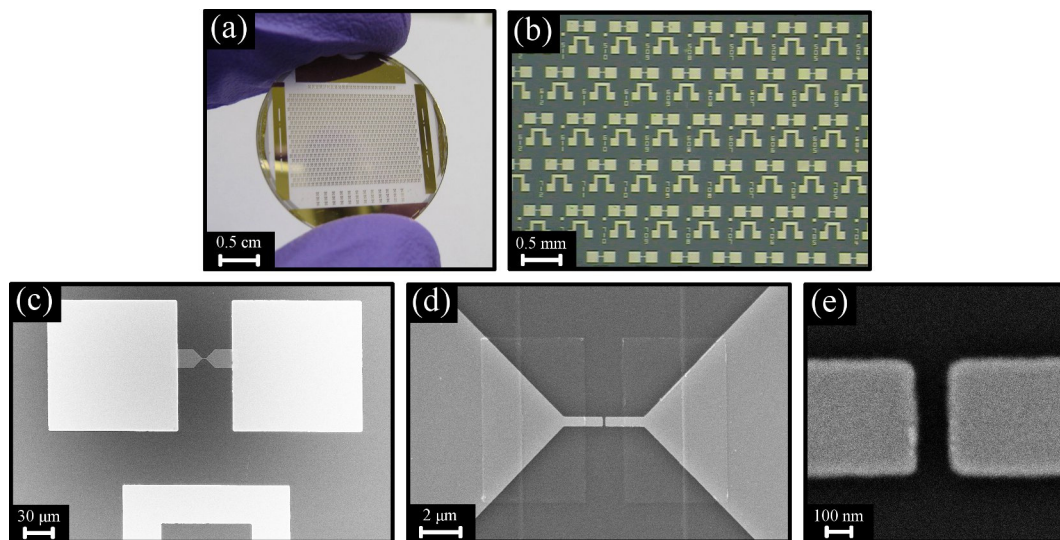


Fig. 3.6 Pictures of a fully processed wafer and devices at various levels of magnification. (a) V_2O_3 devices on a 1" sapphire substrate taken with a handheld camera. (b) Optical microscope image at the contact pad scale. (c) SEM image of the contact pads. (d,e) SEM images of a 125 nm gap device.

We also confirmed the integrity of the devices by performing low-bias resistivity-versus temperature measurements of large devices that did not undergo voltage-induced switching. A comparison between the experimentally measured device resistance and the device resistance predicted based on experimentally measured blanket film resistivities is shown in Fig. 3.7.

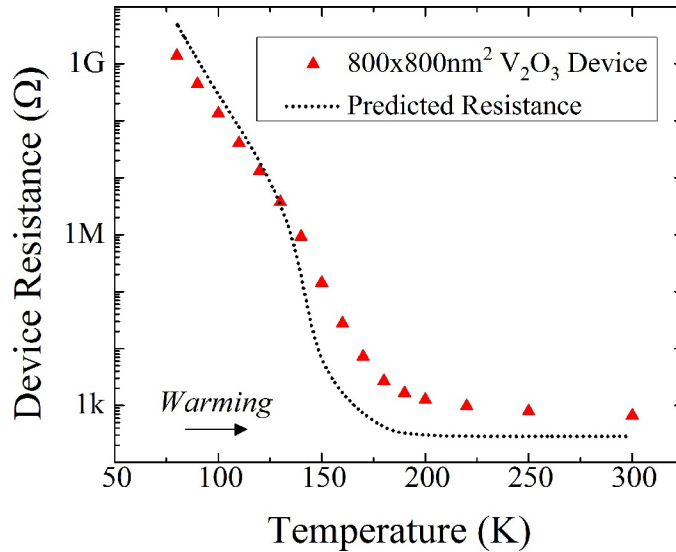


Fig. 3.7 A figure comparing, as a function of temperature, the device resistance that would be predicted by V_2O_3 's blanket film resistivity to the actual resistance of a fully patterned device measured at low bias.

Although device yields were generally acceptable (>50%), the most common failure modes were 1) delamination of the fine gold contacts during ultrasonic or SNO-cleaning leading to an open circuit, or 2) the bridging of gold across the nanogap structure leading to a short. In the second case, this could either be due to a mechanical destruction of the e-beam resist island during the gold deposition or the failure to lift off the gold sitting on top of this resist. These problems were accentuated for smaller and wider devices, where the most shorts were observed. An additional failure sometimes occurred during testing where the device would break open along a mesa or isolation pad step edge. Fig. 3.8 shows an SEM image of both of these closed-circuit and open-circuit failure modes.

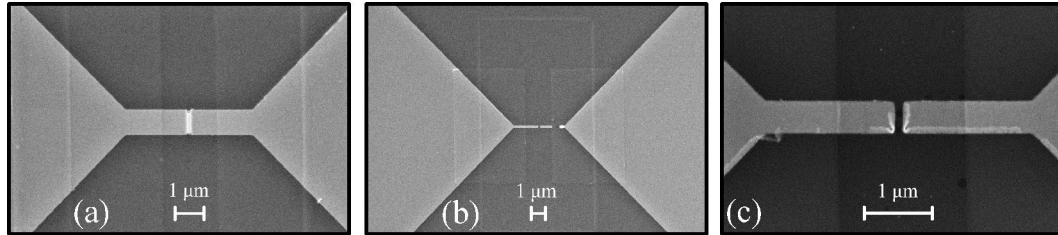


Fig. 3.8 A figure showing several of the most frequent yield-related issues that we encountered during the fabrication of the V_2O_3 nanostructures. (a) A shorted device. (b) A thinning of the contact line over a step edge, resorting in a high resistance point that breaks open upon testing. (c) Fence edges around the nanogap contact lines, a mostly cosmetic issue that should not affect the performance of the device.

3.5 Device Testing

A variable-temperature cryostat equipped with six probe arms was used to measure the I-V characteristics of our V_2O_3 devices as a function of temperature. A picture of this system is shown in Fig. 3.9. The thermally anchored probes could operate in a frequency range between DC and 40 GHz, and they could be moved from device to device. The temperature of the sample stage could be varied between 10 K and 300 K. Additional pictures of the circuit diagram and two high-speed probes making contact to a device can be found in the beginning of Chapter 6.

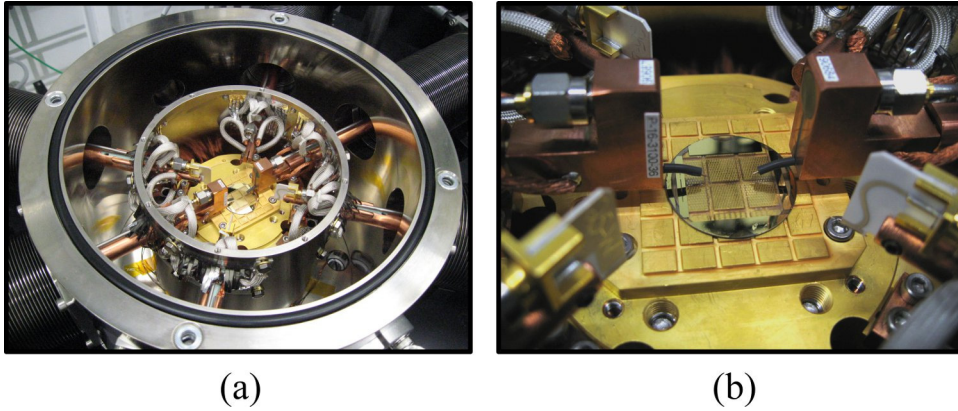


Fig. 3.9 (a) A picture of the Lakeshore variable-temperature probestation chamber. (b) A closer view of the RF probes and a sample placed on the stage.

For the DC measurements, a load resistor was connected in series with the V_2O_3 device, and a continuous voltage was applied in a staircase sweep using a Keithley 6430 Sourcemeter. For the high-speed measurements, the load resistor was removed and a 10300B Picosecond Pulse Labs pulse generator with an intrinsic pulse rise time of 250 ps was used to apply 20 ns long square-wave pulses in a transmission geometry using a digital 12 GHz DSO81204A Agilent oscilloscope.

Chapter 4

THIN FILM GROWTH OF V_2O_3 ON UNANNEALED α - Al_2O_3 (0001)

4.1 Introduction

In this chapter, we begin the presentation of experimental results. We show details on the optimization and characterization of V_2O_3 films grown on unannealed *c*-plane sapphire substrates. We discuss the role of the substrate, the growth temperature, and the growth oxygen pressure on the chemical, structural and electrical properties of the films. Under optimized conditions, we show that V_2O_3 can be grown smoothly and epitaxially onto *c*-plane sapphire substrates with good electrical properties, namely a strong 4-5 order of magnitude metal-to-insulator transition that occurs upon cooling the films down to below 150 K. The growth conditions discussed in this chapter are identical to those ultimately used for the fabrication of nanostructures for the field-effect switching experiments covered in Chapter 6.

Over the last two decades, a number of different techniques have been employed to prepare thin films of V_2O_3 , including reactive sputtering[88, 89], electron-beam evaporation[90-93], thermal evaporation[94, 95], sol-gel deposition[96], and pulsed laser deposition[97-100]. The reported electronic and structural properties of V_2O_3 films vary widely, particularly for thinner films that should be more strongly influenced by substrate-film interactions. Indeed, several authors report the growth of various different “types” of V_2O_3 with metal-insulator transitions whose properties can be correlated with film thickness[95, 100] and the level of compressive strain present along the *c*-axis[91, 93]. Stoichiometry is also an important factor. In studies on bulk crystals of $V_{2(1-y)}O_3$, for example, it is known that a vanadium deficiency corresponding to just $y \sim 0.01$ can completely suppress V_2O_3 's metal-insulator transition[58, 59]. Later in this chapter we will present details from one of our publications[101] that demonstrates the inverse effect, in which growing V_2O_3 films in reduced oxygen environments leads to a stabilization of the insulating phase.

4.2 Materials and Methods

4.2.1 Substrate Selection

For the majority of our work, we have chosen to use the substrate (0001)-oriented α - Al_2O_3 , also known as *c*-plane sapphire. The present chapter focuses on growth

using this substrate. Sapphire has an identical crystal structure to V_2O_3 , and is commercially available in extremely high quality and purity due to its popularity as a substrate for III-V compounds like gallium nitride and II-VI compounds like zinc selenide. However, as can be seen in Table 4.1, there is a significant 4% lattice mismatch to V_2O_3 at room-temperature, which is exacerbated by V_2O_3 's large thermal expansion coefficient which can be up to 5% at growth temperatures near 700 °C. A further advantage of Al_2O_3 is that there is a very robust and well-known annealing recipe that can be used to produce smooth and atomically flat surfaces on polished substrates[102].

| Material | <i>a</i>-axis parameter | <i>c</i>-axis parameter | RT V_2O_3 Mismatch | JCPDS Reference |
|----------------------|------------------------------------|------------------------------------|--|----------------------------|
| α - Al_2O_3 | 4.7587 | 12.9929 | -4.1% | 00-046-1212 |
| V_2O_3 | 4.9540 | 14.0083 | N/A | 00-034-0187 |
| Cr_2O_3 | 4.9588 | 13.5942 | 0.1% | 00-038-1479 |
| α - Fe_2O_3 | 5.0356 | 13.7489 | 1.6% | 00-033-0664 |
| Ti_2O_3 | 5.1390 | 13.6590 | 3.6% | 00-010-0063 |
| $LiTaO_3$ | 5.1530 | 13.7550 | 3.8% | 00-029-0836 |

Table 4.1 The in-plane and out-of plane lattice parameters for the most-common corundum-type rhombohedral oxides. These parameters are taken from the Joint Committee on Powder Diffraction Standards (JCPDS) database.

We also used *a*-plane sapphire substrates, Cr_2O_3 buffer layers, and *c*-plane $LiTaO_3$ substrates to grow V_2O_3 . There has been work published on the preparation of ultra-smooth $LiTaO_3$ surfaces[103], however, we had limited success with the method. For this reason, we never fully adopted the use of this substrate, despite it producing V_2O_3 films with better epitaxy and a more clearly metallic high-temperature phase. Concerning Cr_2O_3 , the lattice constants presented in Table 4.1 suggest that it would be an ideal choice for V_2O_3 . Unfortunately, however, Cr_2O_3 is not commercially available as a substrate. As a substitute, we attempted to use thin films of Cr_2O_3 on α - Al_2O_3 as a buffer layer, to keep any portion of the V_2O_3 film from directly experiencing the full 4% mismatch between V_2O_3 and Al_2O_3 . We discuss all these results in Chapter 5.

4.2.2 Substrate Preparation

All substrates were exposed to a chemical cleaning prior to deposition to help remove organic residue from the surface. This process consisted of a 30 second dip in a (1:1:150) solution of $\text{H}_2\text{O}_2/\text{NH}_4\text{OH}/\text{H}_2\text{O}$ to remove organics, a 30 second rinse in deionized H_2O , 30 seconds of cleaning in an IPA vapor bath, followed by 5 minutes of drying in hot nitrogen gas. During our initial work, these substrates also received a back-coating of gold prior to the chemical cleaning to improve and stabilize their radiative heat transfer characteristics. During this process the front surface was protected by photoresist that was stripped afterwards by acetone. Later, to prevent the diffusion of any gold to the front surface of the wafer during the high-temperature deposition process, the gold back-coating step was eliminated. The substrates were instead pressed against a silicon wafer during deposition to assist with heat transfer and temperature stability. In separate experiments, we determined that neither the gold back-coating nor the sample mounting technique noticeably altered the MIT properties of V_2O_3 films grown on NA-sapphire.

4.2.3 Growth Procedure

Thin films of V_2O_3 were deposited by oxygen plasma-assisted molecular beam epitaxy onto *c*-plane sapphire substrates in various partial pressures of oxygen and at different substrate temperatures. Solid pellets of 99.8% purity served as the vanadium source, and were vaporized within a molybdenum-lined Knudsen cell held at temperatures between 1700 to 1800 °C. For oxidation, a radio-frequency atomic oxygen plasma was generated within a perforated quartz cavity directed at the sample. The plasma source operated at 270 watts of forward power and was supplied with a fixed flow of ultra high purity oxygen through a differentially pumped inlet. The unbaked chamber base pressure was approximately 1×10^{-9} Torr. Molecular oxygen pressures were monitored during growth with a residual gas analyzer located near the sample, and the oxygen flow rate into the plasma cavity was varied so as to give chamber pressures during growth in the range between 1×10^{-8} and 5×10^{-7} Torr. Gradual increases and decreases in the oxygen chamber pressure as large as 10% were observed during film

growth, likely due to gettering effects. All oxygen pressures reported here are values recorded at the end of a 90 minute deposition.

During deposition the samples were heated with a SiC substrate heater to growth temperatures ranging between 600 and 850 °C. Heating and cooling was carried out in the absence of oxygen at rates not exceeding 15°C/min. Film growth was studied *in situ* with reflection high-energy electron diffraction (RHEED) and *ex situ* with atomic force microscopy (AFM), high-resolution x-ray diffraction (XRD), transmission electron microscopy (TEM), and four-point resistivity measurements. All films were grown to a thickness of $\sim 350 \pm 30$ Å at a rate of 0.06-0.07 Å/s. These thicknesses were determined by both Rutherford backscattering analysis and a vertical step-height profilometer. All films displayed temperature-driven MITs with transition temperatures strongly dependent on the amount of oxygen supplied during deposition, except for the film grown in the lowest amount of oxygen pressure which, as we shall show, formed as VO rather than V₂O₃.

4.3 Optimal Film Properties

After preparing V₂O₃ films using various different substrates, oxygen pressures, and growth temperatures we concluded that the optimal and most reproducible way to grow films was to deposit V₂O₃ on unannealed Al₂O₃(0001) at a substrate temperature of 700 °C and an oxygen pressure between than 2×10^{-7} and 5×10^{-7} Torr. In this section, we will present chemical, structural, and electrical characterization of these films. These are also the types of films that we chose to use for the electric field-induced switching experiments. Later in chapter 4, we will demonstrate how the film properties change with different choices of the oxygen growth pressure and substrate temperature.

4.3.1 Electrical Characterization

A typical resistivity versus temperature sweep for an optimal V₂O₃ film deposited on unannealed *c*-plane sapphire is shown in Fig. 4.1. This particular film was deposited at a growth temperature of 700 °C and an oxygen partial pressure of 2.3×10^{-7} Torr. These data were collected in a classic 4-point probe configuration by wirebonding to the sample and then cooling it in a Quantum Design PPMS cryostat. The data show that a strong

metal-insulator transition, at least four orders of magnitude, occurs at approximately 130 K upon cooling. (We define the transition temperature as the point of inflection, or the maximum rate of resistance change with temperature on a log scale.) Upon warming the sample back up to room temperature, the metallic state returns hysteretically at approximately 142 K. We infer that the broadening of the MIT and its shifting to lower temperature are due to the substrate-film interaction and residual strain in the films.

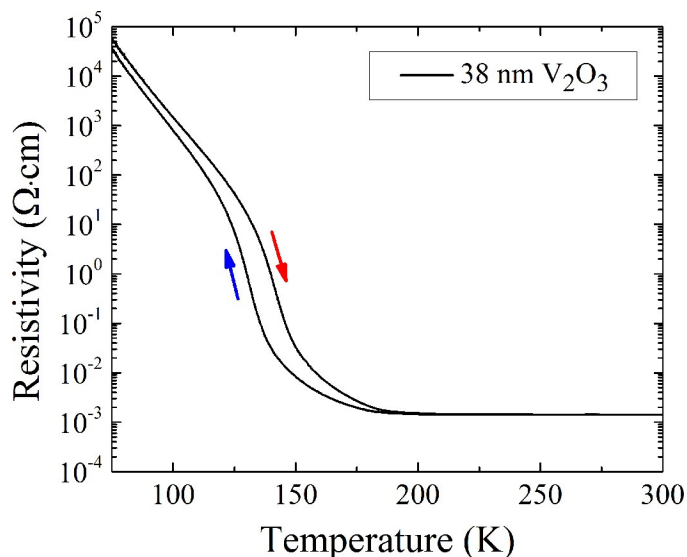


Fig. 4.1 A typical resistivity versus temperature plot for a 38 nm V₂O₃ film grown under optimal conditions.

4.3.2 Structural Characterization (RHEED, AFM, XRD, TEM)

Typical RHEED and AFM data for an optimal V₂O₃ film can be seen in Fig. 4.2. The continuous RHEED streaks indicate that V₂O₃ grew smoothly and epitaxially with the relationship (0001) V₂O₃ // (0001) Al₂O₃ and $[11\bar{2}0]$ V₂O₃ // $[11\bar{2}0]$ Al₂O₃. These conclusions are further supported by a clear TEM zone axis simultaneously visible in both the film and substrate, as seen in Fig. 4.3. In all films that displayed a temperature-driven MIT, the RHEED streak spacing contracted very quickly during the first 10-20 Å of growth and then stabilized at a streak spacing ~4% smaller than that seen for the Al₂O₃ substrate. Note that there is a 4.1% lattice mismatch within the *c*-plane between the isosymmetric bulk crystals of V₂O₃ and Al₂O₃. No RHEED oscillations were observed for any of these samples.

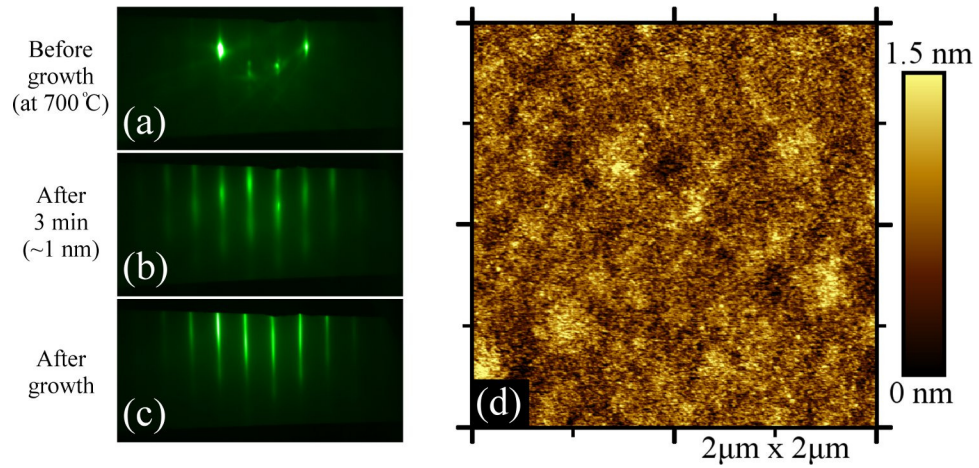


Fig. 4.2 Typical RHEED and AFM data for V_2O_3 films grown on c -plane sapphire under optimal conditions. This particular film is approximately 38 nm in thickness, was grown at a substrate temperature of 700 °C, an oxygen pressure of 2.3×10^{-7} Torr, and displays 2.9 Å rms. The RHEED data were collected along the $[11\bar{2}0]$ azimuth.

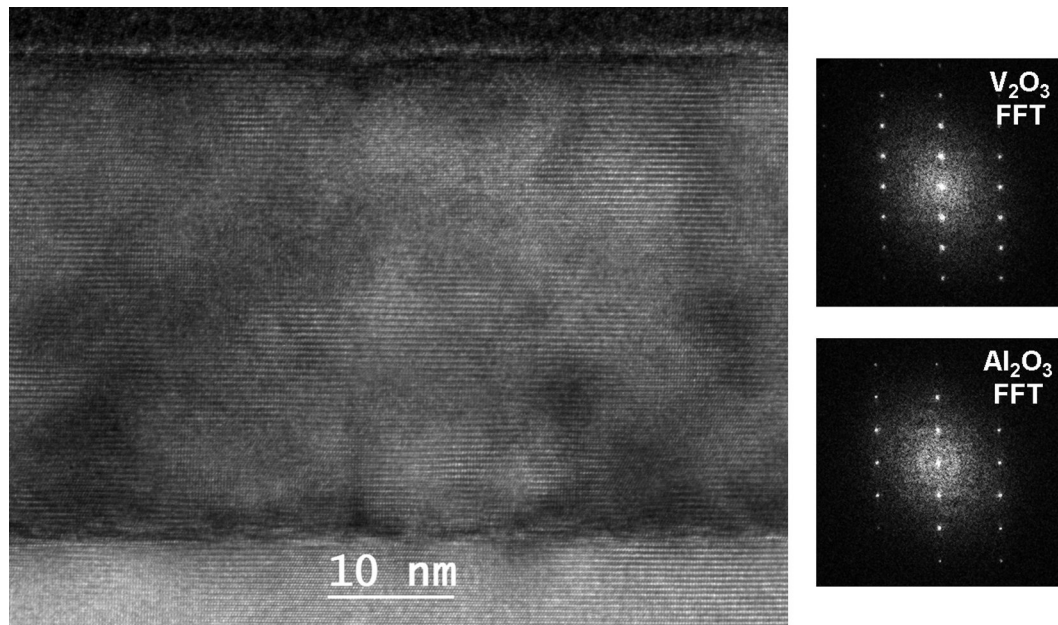


Fig. 4.3 A TEM image of a 38 nm V_2O_3 film deposited at 850 °C along with selected-area fast Fourier transforms of the film and substrate, showing that the film grew epitaxially with the relationship $(0001)V_2O_3 // (0001)Al_2O_3$ and $[11\bar{2}0]V_2O_3 // [11\bar{2}0]Al_2O_3$.

A coupled θ - 2θ XRD scan and a reciprocal lattice map of the V_2O_3 and Al_2O_3 ($10\bar{1}10$) peaks collected from a representative optimal V_2O_3 film can be seen in Fig. 4.4. The symmetric θ - 2θ scans confirmed the single-phase nature of these films, at least to within the noise level of our diffractometry equipment, by revealing only $(000l)$ Al_2O_3 and V_2O_3 peaks. These films all displayed $d_{(0006)}$ spacings approximately 0.4% smaller than the value for bulk V_2O_3 . The reciprocal lattice map shows that the 0.4% out-of-plane compression was accompanied by an in-plane expansion of roughly the same magnitude. As an aside, the $(10\bar{1}10)$ peak is the most intense asymmetric peak that is measurable. The directionality of this unit cell distortion is opposite to what would be expected for the -4.1% isotropic in-plane strain at the V_2O_3 - Al_2O_3 interface. Previous work[99] conjectures that this residual strain arises from the roughly 1%/(400 K) thermal expansion difference between Al_2O_3 and V_2O_3 as the film is cooled from the growth temperature to room-temperature.

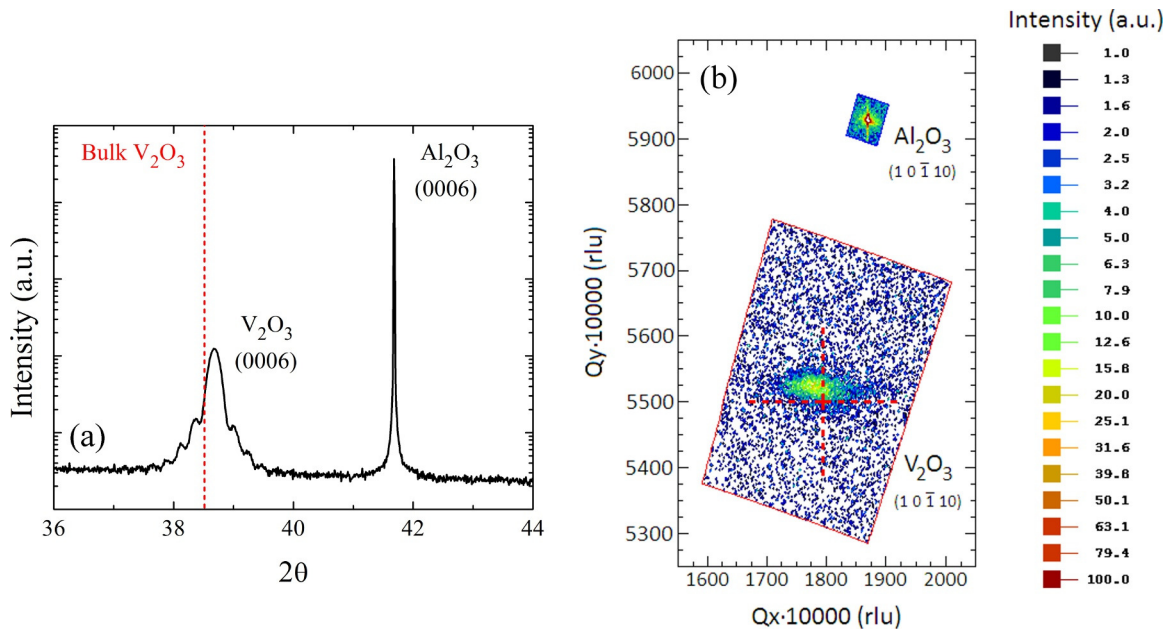


Fig. 4.4 Coupled θ - 2θ X-ray diffraction scan. Reciprocal lattice of the $(10\bar{1}10)$ V_2O_3 and Al_2O_3 Bragg peaks. Thickness fringes were only visible in roughly half of the grown films, and especially those grown in higher oxygen pressures.

4.3.1 Chemical Characterization (RBS, XPS)

When we began this project, the original practice of the lab was to use gold as a substrate back-coating to improve and stabilize the substrates thermal absorption properties during deposition, as mentioned previously. Gold has a good emissivity and it was readily available in our deposition systems. Initial samples of V_2O_5 , however, showed a small contamination of a heavy metal at a level of approximately 0.01% as observed by Rutherford backscattering. Furthermore, the mass of this contamination was consistent with gold. Because of this, we switched to using silicon substrates to provide a backing to the samples during deposition. The RBS spectra of a V_2O_5 film deposited on a gold-backed sapphire substrate and a silicon-backed sapphire substrate can be seen in Fig. 4.5. Neither the gold backing nor the sample mounting technique was observed to affect the metal-insulator properties of the V_2O_5 films.

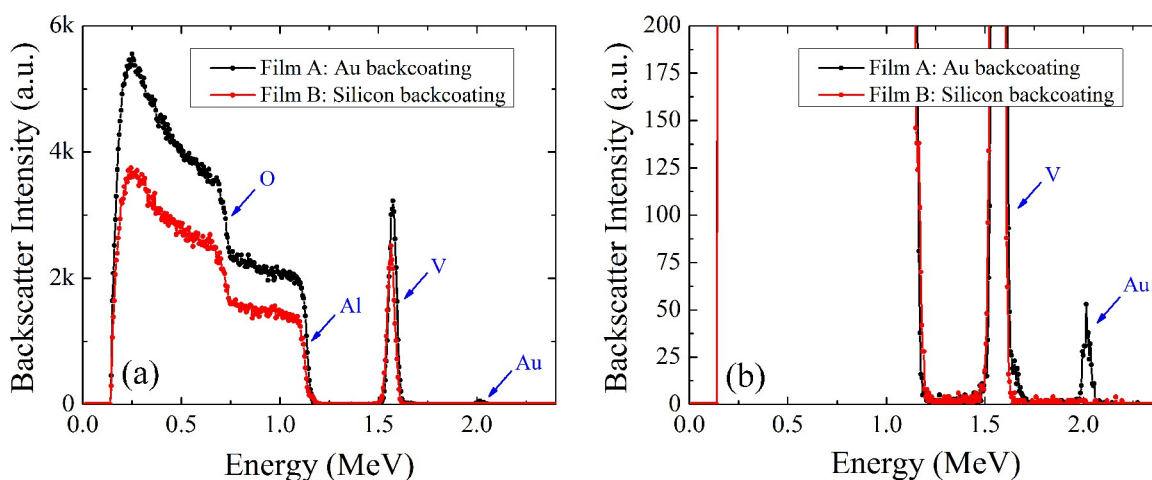


Fig. 4.5 (a) RBS data showing the effect of using a gold backcoating to provide thermal absorption stability during deposition. (b) The same plot rescaled to show the gold contamination level.

Gold was not the only sample contamination issue we encountered. The very first V_2O_5 film we attempted to deposit were made with Knudsen cells lined with Al_2O_3 crucibles. The RBS result for this film showed signs of both alumina and tantalum contamination. Based on this, we concluded that the Al_2O_3 must be sublimating at the high temperatures needed for vanadium evaporation. Furthermore, dark metallic stains

formed on the outside of the Al_2O_3 crucibles that were confirmed by RBS to be tantalum, evidence of some kind of reaction between Al_2O_3 and tantalum. To correct these issues we continued the project with new crucibles cut from the refractory metal molybdenum and placed into the tantalum-based Knudsen cells. After this, we saw no further signs of aluminum or tantalum contamination.

We also performed XPS measurements, displayed in Fig. 4.6, to confirm the phase of the V_2O_3 films and confirm the elemental purity. Fig. 4.6(a) shows a survey spectrum of V_2O_3 that only shows only V and O peaks. No sign of carbon contamination exists because the experiment was performed *in situ*, or without exposing the sample to air.

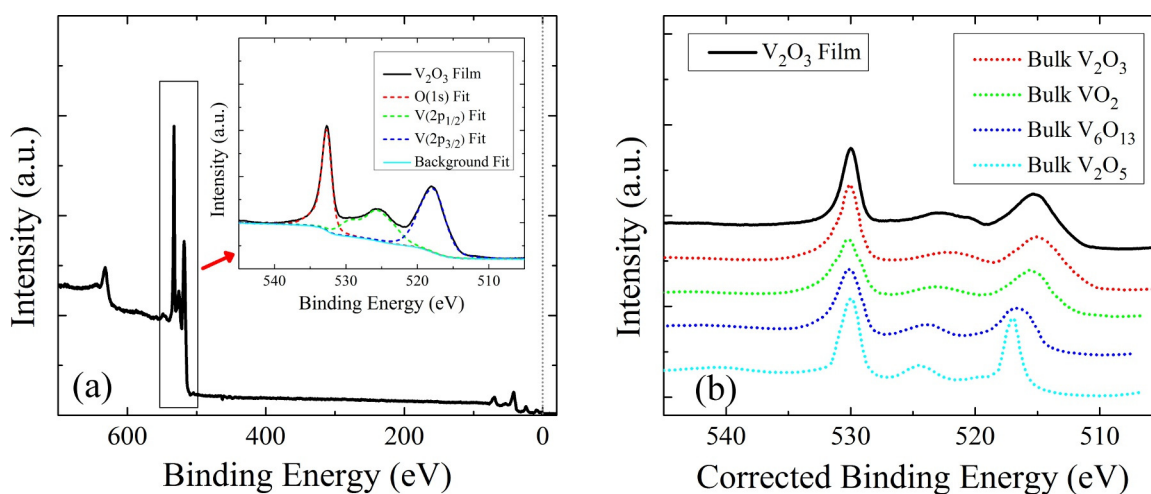


Fig. 4.6 (a) A satellite-subtracted XPS spectrum for a nominally 40 nm thick film of V_2O_3 deposited on unannealed *c*-plane sapphire at 700 °C. The inset shows fits to the $\text{O}(1s)$ and $\text{V}(2p)$ peaks that are used for a rough calculation of stoichiometry. (b) A comparison of our V_2O_3 spectrum with various known spectra from previous work[104].

Previous photoelectron spectroscopy investigations[104-107] of the most stable phases of vanadium oxide allows us to classify the phase of the films we have deposited based on the shapes and binding energies of the $\text{O}(1s)$ and $\text{V}(2p)$ peaks, as seen in Fig. 4.6(b). Table 4.2 shows the binding energies of these peaks and the characteristic energy difference Δ between the $\text{O}(1s)$ peak and the $\text{V}(2p_{3/2})$ peak, which is also a fingerprint of phase. These data allow us to rule out the formation of V_2O_5 or V_6O_{13} , but it is

particularly difficult to use this method to distinguish between VO_2 and V_2O_3 because they have very similar peak shapes and values of Δ .

| Phase | O:V Ratio | BE of O(1s) (eV) | BE of V(2p _{3/2}) (eV) | Δ (eV) |
|-----------------------------------|-----------|---------------------|-------------------------------------|---------------|
| Bulk V_2O_3 | 1.5 | 530.0 | 515.15 | 14.84 |
| Bulk VO_2 | 2 | 530.0 | 515.65 | 14.35 |
| Bulk V_6O_{13} | 2.17 | 530.0 | 516.5 | 13.5 |
| Bulk V_4O_9 | 2.25 | 529.8 | 516.75 | 13.05 |
| Bulk V_3O_7 | 2.33 | 529.8 | 516.9 | 12.9 |
| Bulk V_2O_5 | 2.5 | 529.8 | 517.0 | 12.8 |
| 40 nm V_2O_3 Film | ~1.5 | 532.7 | 518.0 | 14.7 |

Table 4.2 A table showing the binding energies for the O(1s) and V(2p_{3/2}) peaks of various different phases of vanadium oxide extracted from Ref[104], along with experimental values from the present work measured by XPS on a 40 nm V_2O_3 film grown by oxygen plasma-assisted thermal evaporation. The energy difference between the peaks, Δ , that we observe is consistent with the previously reported values for bulk samples of V_2O_3 .

By integrating the core-level peak areas, as seen in the inset of Fig. 4.6(a), and then dividing these areas by the atomic sensitivity factors of vanadium and oxygen, we can obtain a more direct estimate of the stoichiometry of our films, as seen in Table 4.3. The result agrees well with the expected atomic percentages of V_2O_3 . This peak integration method gives 59% oxygen content and 41% vanadium content for a representative 40 nm V_2O_3 film grown on unannealed *c*-plane sapphire. The 1% disagreement with the expected 60/40 ratio is easily within the margin of error associated with this method.

| Energy Level | Binding Energy (eV) | Peak Area (cps) | ASF | Atomic % |
|-----------------------|---------------------|-----------------|------|----------|
| V(2s) | 632.0 | | | |
| O(1s) | 532.7 | 499,756 | 0.66 | ~ 59% O |
| V(2p _{1/2}) | 525.9 | | | |
| V(2p _{3/2}) | 518.0 | 695,597 | 1.3 | ~ 41% V |
| V(3s) | 69.9 | | | |
| V(3p) | 42.3 | | | |
| O(2s) | 24.2 | | | |
| O(2p) | 9.3 | | | |
| V(3d) | 2.9 | | | |

Table 4.3 A table showing the binding energies for various XPS peaks from a 40 nm film of V₂O₃. The O(1s) and V(2p_{3/2}) peak areas can be used to obtain a rough estimate of the surface stoichiometry based on atomic sensitivity factors provided in Ref[108].

4.4 Growth Temperature Dependence

Within a growth window of 600 to 750 °C and O₂ pressures greater than approximately 2×10^{-7} Torr, the properties of the MIT and the out-of-plane d-spacing parameter (~ 2.327 Å) were very stable. We presume the films grown in this window correspond to stoichiometric, or even slightly oxygen-rich, V₂O₃. Growth at 850 °C increased the magnitude of the resistance change at the MIT by at least one order of magnitude and increased the d-spacing parameter (2.3315 Å) to within 0.2% of the value for bulk V₂O₃ (2.3356 Å) that is reported in JCPDS file 00-034-0187.

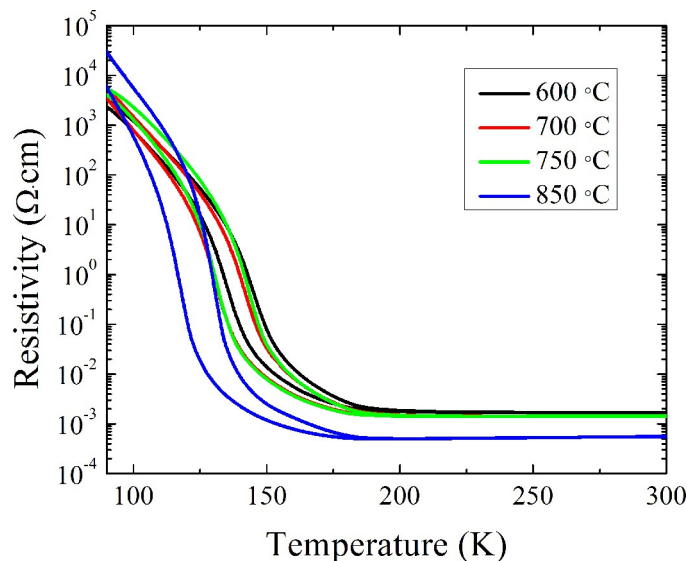


Fig. 4.7 Resistivity versus temperature sweeps for V_2O_3 deposited on unannealed c-plane sapphire at several temperatures between 600 and 850 °C and an oxygen partial pressure greater than 2×10^{-7} Torr. The electrical properties were extremely robust and reproducible within a growth window of 600 to 750 °C.

4.5 Oxygen Pressure Dependence

As mentioned in Chapter 2, titanium doping and vanadium vacancies in bulk samples of $(Ti_xV_{1-x})_2O_3$ and $V_{2(1-y)}O_3$ both decrease T_{MIT} until the insulating phase is fully suppressed for $x > \sim 0.05$ and $y > \sim 0.01$ [36, 58, 59]. Alternately, chromium doping in bulk samples of $(Cr_xV_{1-x})_2O_3$ increases T_{MIT} and creates a paramagnetic insulating state near room temperature for $0.005 < x < 0.018$ [36, 57]. The effect of oxygen vacancies, however, has not been fully explored, likely due to the inherent instability of V_2O_{3-x} . It has been found to be very difficult, for example, to reduce the oxygen content of bulk crystals of V_2O_3 by annealing in a controlled atmosphere[109, 110]. Thin film growth techniques, on the other hand, allow for the creation and study of metastable stoichiometries of V_2O_3 not otherwise accessible.

Decreasing the oxygen pressure during the V_2O_3 growth led to higher values of the metal-insulator transition temperature, semiconducting behavior in the high-temperature phase, and a decrease in the resistivity change at the metal-insulator transition, all with very little change in the crystal structure. These trends can be seen in Fig. 4.8.

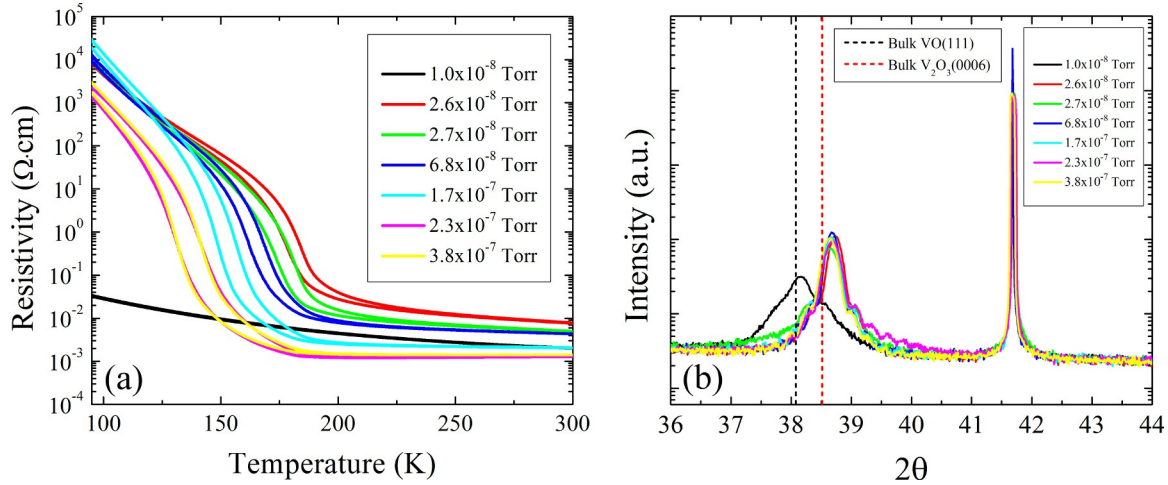


Fig. 4.8 (a) Resistivity versus temperature sweeps, and (b) symmetric θ - 2θ XRD scans collected from V_2O_3 films grown on unannealed c -plane sapphire substrates. The dotted lines indicate the bulk crystal values for $d_{(0006)}$ V_2O_3 and $d_{(111)}$ VO, taken from JCPDS references 00-034-0187 and 03-065-4054, respectively.

As the oxygen pressure supplied during growth was reduced, the RHEED streaks became slightly more spot-like, indicating a rougher and more three-dimensional nature to the surface. In the most oxygen-deficient film grown at a pressure of 1.0×10^{-8} Torr, every 2nd and 3rd streak disappeared, and the spacing between the remaining streaks was comparatively 1.2% smaller. This observation is consistent with the formation of the face-centered cubic phase VO growing in the epitaxial relationship $(111) \text{VO} // (0001) \text{Al}_2\text{O}_3$ and $[110] \text{VO} // [01\bar{1}0] \text{Al}_2\text{O}_3$. A schematic demonstrating how the (111) face of VO can nest within the (0001) face of V_2O_3 or Al_2O_3 is shown in Fig. 4.9. This figure also demonstrates how the lateral periodicity of VO, as seen by a RHEED beam incident along the $[11\bar{2}0]$ direction decreases by a factor of three, which would lead to the disappearance of every 2nd and 3rd RHEED streak in the VO phase.

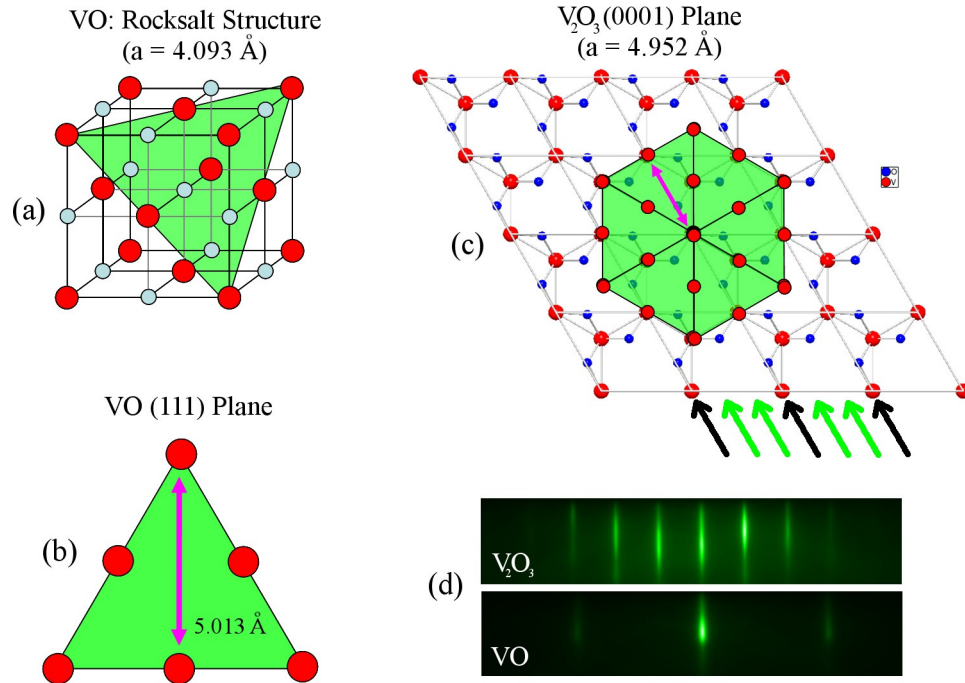


Fig. 4.9 (a) The rocksalt structure of VO, along with a planar cut of one of the (111) planes. (b) A straight-on view showing the triangular lattice of the vanadium atoms in a (111) plane of VO, the base-to-height distance of this particular triangle is 5.013 Å. (c) The VO(111) triangles nested into one monolayer of V_2O_3 , as viewed along V_2O_3 's (0001) axis. (d) A comparison of the RHEED patterns for VO and V_2O_3 , showing the disappearance of every 2nd and 3rd line. The black arrows in (c) show the RHEED beam diffraction spacing for V_2O_3 incident along the $[11\bar{2}0]$ direction. The green arrows in (c) show how this diffraction spacing shrinks by one-third, consistent with the RHEED streak spacing expanding by a factor of three in reciprocal space.

A compilation of the transition temperatures and d -spacing values extracted from coupled θ - 2θ scans is shown in Fig. 4.10. The transition temperature can be seen to systematically increase with decreasing pressures of supplied oxygen. These films all displayed $d_{(0006)}$ spacings approximately 0.4% smaller than the value for bulk V_2O_3 , and the d -spacing of the most oxygen-deficient film matched the value of $d_{(111)}$ for bulk VO to within 0.2%.

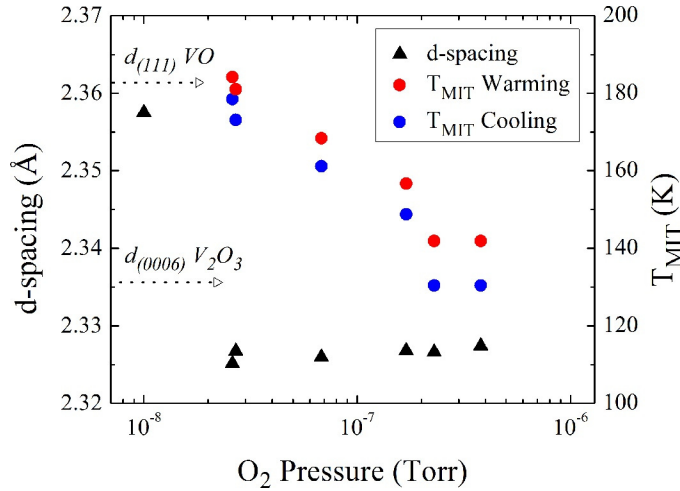


Fig. 4.10 Out-of-plane d -spacing parameters calculated from symmetric θ - 2θ XRD scans, and MIT temperatures extracted from the warming and cooling resistivity versus temperature curves. T_{MIT} is defined as the point of inflection, i.e. the temperature value showing the maximum derivative of $\log(\rho)$ with respect to temperature.

Given that bulk samples of oxygen-rich V_2O_3 are known to have a decreased value of T_{MIT} [58, 59], and that our films grown in reduced oxygen pressures show a systematic increase in the value of T_{MIT} , it is reasonable to assume that the oxygen stoichiometry is controlling T_{MIT} . This is an exciting prospect, given that oxygen-deficient V_2O_{3-x} is difficult to make in bulk crystals. Using the variation of T_{MIT} with x from bulk crystals[59] we can estimate that $\Delta x = 0.006$ in our set of samples based on the 50 K variation in T_{MIT} that we find. This corresponds to a change in oxygen content of 0.2%. We cannot measure such a tiny variation in oxygen content directly, but using T_{MIT} we can reference our films and their associated properties to previous work on non-stoichiometric and doped V_2O_3 . Fig. 4.11(a) shows the activation energies E_σ extracted from Fig. 4.8(a) by fitting the insulating state resistivities to $\rho(T) = \rho_0 e^{E_\sigma/(kT)}$ and compares these values to those for the systems $V_{2(1-y)}O_3$, $(Cr_xV_{1-x})_2O_3$ and $(Ti_xV_{1-x})_2O_3$ which we have extracted from references [59] and [57]. Fig. 4.11(b) compares the room-temperature resistivity (ρ_{RT}) and the insulating state resistivity at the transition temperature (ρ_{MIT}) for these bulk systems with our own films. It is immediately apparent that the films show several key differences in behavior. First, their activation energy is constant or even decreasing with T_{MIT} ; second, ρ_{RT} is increasing at a rate different from

both $V_{2(1-y)}O_3$ and $(Cr_xV_{1-x})_2O_3$; and third, there is no appearance of the high-temperature insulating state near room-temperature as found in $(Cr_xV_{1-x})_2O_3$. Interestingly, the dependence of ρ_{MIT} on T_{MIT} is comparable to that found in $V_{2(1-y)}O_3$, but very different from that found in $(Ti_xV_{1-x})_2O_3$, which shows a dramatic decrease in the magnitude of the resistivity change at lower values of T_{MIT} . This similarity to $V_{2(1-y)}O_3$ suggests that the magnitude of T_{MIT} in our films is determined by their non-stoichiometry, which is controlled by the oxygen pressure during growth.

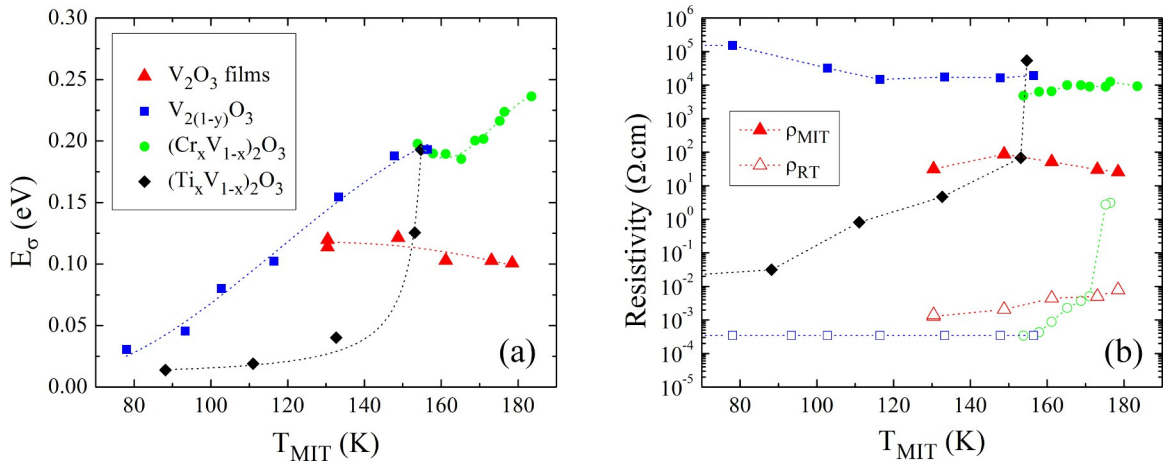


Fig. 4.11 (a) Activation energy and (b) insulating state resistivity ρ_{MIT} at T_{MIT} (filled shapes) and room-temperature resistivity ρ_{RT} (hollow shapes) plotted against T_{MIT} . The non-triangular data points represent data from previous studies on V-deficiencies, Cr-doping and Ti-doping extracted from references[57, 59]. The triangular data points are from the V_2O_3 films in this study, with ρ_{MIT} being the resistivity value at T_{MIT} given by a functional fit to the insulating state, and ρ_{RT} being the resistivity value at 295 K. The ρ_{RT} data for $(Ti_xV_{1-x})_2O_3$ could not be accurately obtained and are omitted. It should be noted that sample doping levels and stoichiometries are implicitly expressed on the x-axis in terms of T_{MIT} .

There is still debate over whether the decrease of T_{MIT} in bulk crystals of $V_{2(1-y)}O_3$ due to the vanadium vacancies is primarily controlled by electron band-width or band filling[4], so either of these mechanisms is potentially responsible for the increase of T_{MIT} seen in our films grown at reduced oxygen pressures. Oxygen vacancies or vanadium interstitials could certainly change the electron counting on V sites and thereby influence the Mott-Hubbard transition of V_2O_3 . However, the semiconducting behavior we observe above T_{MIT} and the increasing values of ρ_{RT} with decreasing oxygen growth pressures

could both suggest greater Anderson localization resulting from higher numbers of defects, which could, in turn, trigger an earlier onset of V_2O_3 's insulating state.

4.6 Thickness Dependence

We present thickness data in the following chapter for V_2O_3 growth on unannealed c -plane sapphire substrates in comparison with data for annealed c -planes sapphire substrates, unannealed a -plane sapphire substrates, and annealed c -plane $LiTaO_3$ substrates.

4.7 Summary

In summary, we have presented conditions for the optimal growth of V_2O_3 films. The films show strong metal-insulator transitions near 140 K when grown in a growth temperature window of 600 °C to 750 °C, and an oxygen pressure window between 2×10^{-7} Torr and 5×10^{-7} Torr. The chemical and structural data for these films is consistent with V_2O_3 , with no sign of the presence of additional phases. In Chapter 7, we will discuss using the electrical measurements of two-terminal nanostructures patterned from films grown under these conditions using the fabrication recipes detailed in Section 3.4.

We also showed that by reducing the amount of oxygen supplied during growth led to a nearly 50 K increase in V_2O_3 's metal-insulator transition temperature to a temperature as high as 184 K. By systematically varying the oxygen pressure, the transition temperature monotonically increased, which was accompanied by a concomitant increase in the room-temperature resistivity. These trends are consistent with a continuous change in the stoichiometry of V_2O_3 .

Chapter 5

GROWTH OF V_2O_3 ON OTHER SUBSTRATES

5.1 Introduction

In this chapter, we explore the growth of V_2O_3 on other substrates, namely, annealed c -plane sapphire, unannealed a -plane sapphire, annealed $LiTaO_3$ substrates, and Cr_2O_3 buffer layers. For example, we show that annealing the c -plane sapphire substrates prior to deposition to produce ultra-smooth terraced surfaces with atomic-scale step heights ultimately degrades the quality of the V_2O_3 films due to a higher level of epitaxy and strain transfer at the interface. Although these films were not used in our switching experiments, we present this work here because we believe it will offer valuable insight for future attempts to produce even higher quality V_2O_3 films and interfaces.

5.2 Growth on Annealed Sapphire(0001)

In this section, we will compare the structural and electronic properties of V_2O_3 thin films deposited by oxygen plasma-assisted molecular beam epitaxy onto annealed and unannealed sapphire substrates. Annealing the substrates before growth to produce ultra-smooth surfaces improved the initial epitaxy of V_2O_3 , according to *in situ* high-energy electron diffraction. Surprisingly, the more coherent interface was accompanied by an island-like film surface, broad X-ray diffraction peaks, and strong localization in V_2O_3 's normally metallic high-temperature phase. We attribute these results to enhanced strain coupling between the substrate and film, highlighting the vulnerability of V_2O_3 's strongly correlated metallic phase to defects and disorder.

As mentioned previously, the reported electronic and structural properties of V_2O_3 films vary widely, particularly for thinner films that should be more strongly influenced by substrate-film interactions. Several authors have reported the growth of various different “types” of V_2O_3 with metal-insulator transitions whose properties can be correlated with film thickness[95, 100] and the level of compressive strain present along the c -axis[91, 93]. Stoichiometry is also an important factor. In studies of bulk crystals of $V_{2(1-y)}O_3$, for example, it is known that a vanadium deficiency corresponding to just $y \sim 0.01$ can completely suppress V_2O_3 's metal-insulator transition[58, 59]. The present authors have also recently demonstrated the inverse effect, in which growing V_2O_3 films in reduced oxygen environments leads to a stabilization of the insulating phase[101].

One further factor, as yet uninvestigated, but which could potentially account for some of the reported variation in V_2O_3 thin films is the morphology of the underlying substrate. The degree of epitaxial coherence at the substrate-film interface can potentially play a very critical role in strain transfer, defect formation, and the evolution of the film surface. These factors are especially important for strongly correlated electron systems like V_2O_3 that are very sensitive to defect-induced localization and strain-induced changes in bandwidth.

Here we present a dramatic dependence of V_2O_3 's structural and electronic properties on the surface morphology of *c*-plane sapphire substrates. Epitaxial thin films of V_2O_3 of varying thicknesses were deposited by oxygen plasma-assisted molecular beam epitaxy onto both unannealed and annealed *c*-plane sapphire substrates, the latter having an ultra-smooth, terraced surface with atomic-scale step heights. The growth conditions used are identical to those previously outlined in this dissertation in Section 3.2 and Chapter 4. Namely, these samples were all held at 700 °C during deposition with a growth oxygen pressure between 2×10^{-7} and 5×10^{-7} Torr as measured by a residual gas analyzer located near the sample. The sample deposition rates all fell between 0.05 and 0.1 Å/s, and the sample thicknesses were determined *ex situ* by a vertical step height profilometer. These films were characterized by *in situ* reflection high-energy electron diffraction (RHEED), atomic force microscopy (AFM), X-ray diffraction (XRD), and 4-point probe resistivity versus temperature measurements.

Films ranging in thickness between 6 nm and 96 nm were deposited onto *c*-plane sapphire substrates subjected to two different preparation recipes. In the first recipe, the substrates received a 30 second dip in a (1:1:150) solution of $H_2O_2/NH_4OH/H_2O$ to remove organics, a 30 second rinse in deionized H_2O , 30 seconds of cleaning in an IPA vapor bath, followed by 5 minutes of drying in hot nitrogen gas. We will refer to these substrates as NA-sapphire, or not-annealed sapphire. In the second recipe, the substrates received an identical treatment followed by a 90 minute anneal in air at 1050 °C in a tube furnace. This step is well-known to produce ultra-smooth surfaces on *c*-plane sapphire substrates[102]. We refer to these substrates as AN-sapphire, or annealed sapphire. One additional difference between the NA-sapphire and AN-sapphire substrates is that the NA-sapphire substrates received a back-coating of gold prior to the chemical cleaning to

improve their thermal absorption characteristics. During this process the front surface was protected by photoresist that was later stripped by acetone. The AN-sapphire substrates received no such back-coating to preclude any diffusion of gold to the front surface at high temperature. These substrates were instead pressed against a silicon wafer during deposition to assist with heat transfer and temperature stability. In separate experiments, we determined that neither the gold back-coating nor the sample mounting technique noticeably altered the MIT properties of V_2O_3 films grown on NA-sapphire.

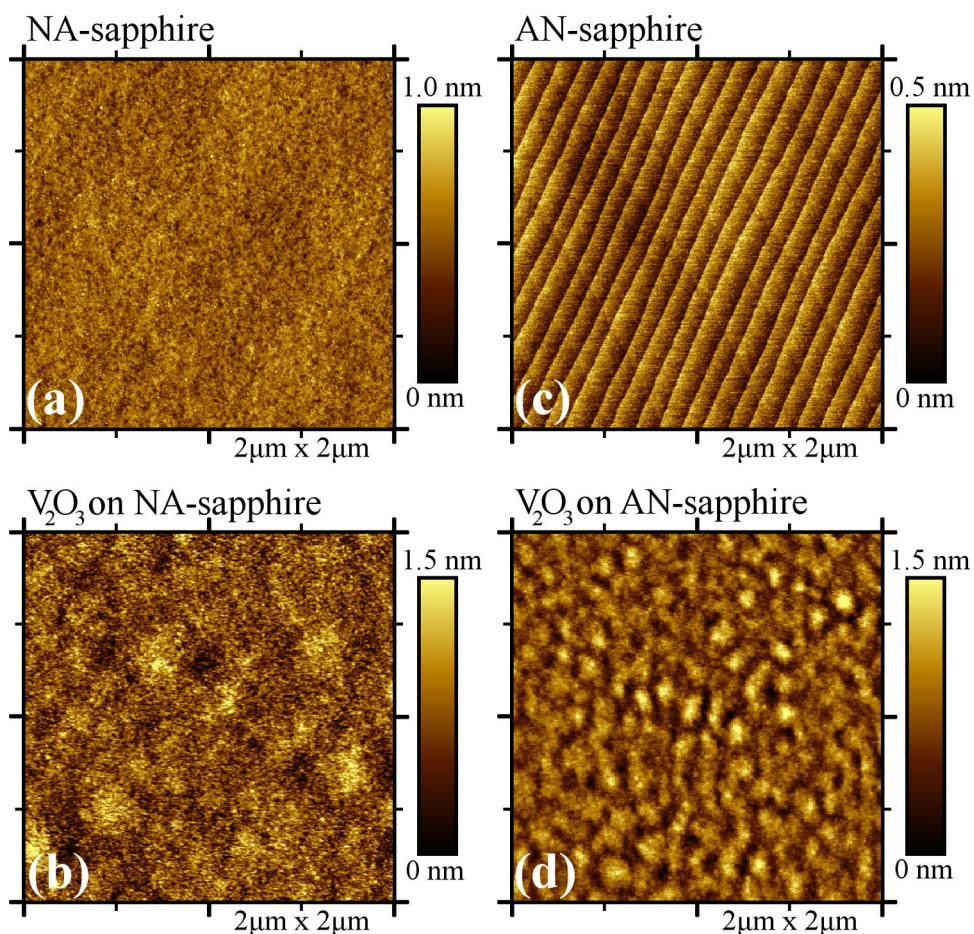


Fig. 5.1 Atomic force microscopy images of (a) a c -plane NA-sapphire substrate, (b) a 38 nm V_2O_3 film grown on NA-sapphire, (c) a c -plane AN-sapphire substrate annealed at 1050 °C for 90 minutes to produce an ultra-smooth surface, and (d) a 43 nm V_2O_3 film grown on AN-sapphire. The root-mean square roughnesses of these four surfaces are 1.2 Å, 2.9 Å, 0.9 Å and 2.4 Å, respectively.

Typical initial substrate and final film surface morphologies are depicted in Fig. 5.1 for each type of sample. The NA-sapphire substrate shows no recognizable features,

while the AN-sapphire substrate shows clear terraces with step edge heights of approximately 2 \AA , which is consistent with the distance between the (0001) planes of the oxygen sublattice in sapphire. Surprisingly, V_2O_3 films deposited onto the smoother annealed substrate always resulted in a more island-like surface. The root-mean-square roughnesses of the films on NA-sapphire and AN-sapphire substrates depicted in Fig. 5.1 are actually very similar (2.9 \AA and 2.4 \AA , respectively), but the striking visual difference of the film deposited on AN-sapphire is due to a smaller characteristic feature size of approximately 100 nm . These film surfaces form during the high-temperature growth process, as verified by *in situ* RHEED analysis seen in Fig. 5.2. Prior to deposition, the atomically flat AN-sapphire substrates produce a very clear and sharp Laue circle, while NA-sapphire substrates show vertical spreading of these spots due to a lateral decoherence of the surface. As the V_2O_3 deposition begins, both types of samples show a degree of initial surface roughness that is indicated by their lateral streak width and a faint underlying spottiness. The films deposited on AN-sapphire, however, have very strong specular spot reflections that oscillate in intensity, as can be seen in Fig. 5.2(g). These oscillations typically fade after between 4 and 20 monolayers of growth, but are nevertheless a sign of good registry between the film and substrate. The RHEED streak spacing for films grown on AN-sapphire relaxes after approximately 2 nm of growth, yet continuously evolves from the substrate to the film, another good indicator of interface coherence. Note that while *c*-plane V_2O_3 has a 4.1% larger in-plane lattice parameter than sapphire at room temperature, the mismatch at a growth temperature of $700 \text{ }^\circ\text{C}$ increases to 5% due to the difference in the thermal expansion coefficients of V_2O_3 and Al_2O_3 . For films on NA-sapphire, the specular spot dies out more quickly, no oscillations are observed, and the streak spacing relaxes more abruptly. By the end of deposition, the RHEED streaks for films deposited on NA-sapphire sharpen significantly, and the spottiness fades. The streaks for V_2O_3 on AN-sapphire, however, remain blurry and faintly retain the spot-like background throughout the growth process. This observation is indicative of a more three-dimensional film surface, consistent with the AFM data.

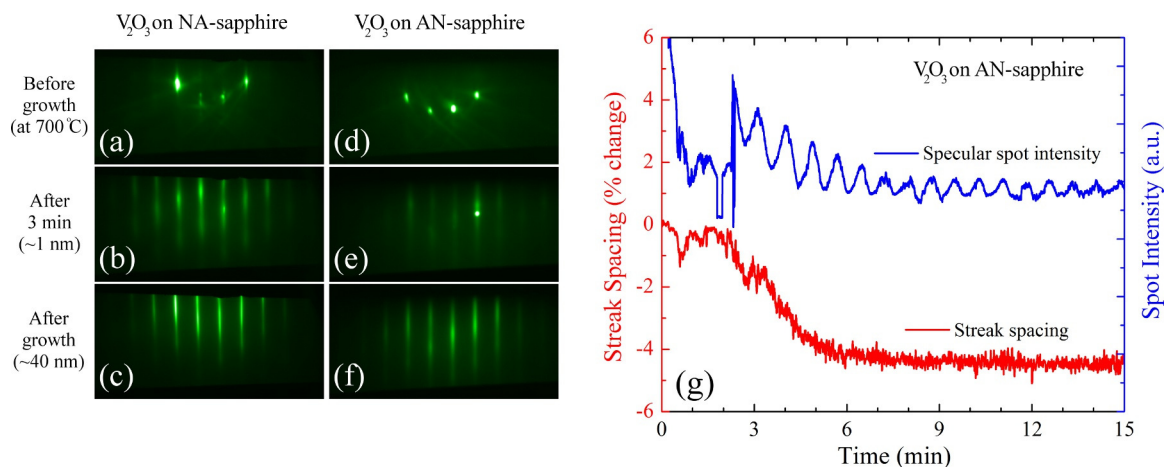


Fig. 5.2 (a,b,c) RHEED patterns taken along the $[11\bar{2}0]$ azimuth before, during, and after deposition of a 38 nm V_2O_3 film onto NA-sapphire. (d,e,f) Equivalent images taken before, during, and after deposition of 43 nm of V_2O_3 onto AN-sapphire. (g) Examples of specular spot intensity oscillations and streak spacing as a function of time for two different V_2O_3 films deposited on AN-sapphire under similar conditions. The discontinuous jumps in the oscillation data between 2 and 3 minutes are due to manual readjustment of the electron beam's grid voltage. The period of oscillation is approximately 48 seconds, corresponding to a deposition rate of 0.05 Å/s, or 0.3 nm/min. No oscillations occurred for films grown on NA-sapphire.

Coupled θ -2 θ XRD scans reveal only (000 l) substrate and film peaks for both types of samples, confirming the epitaxial and single phase nature of V_2O_3 . As shown in Fig. 5.3(a), the peaks for both types of films are shifted away from what would be expected for fully relaxed V_2O_3 . These shifts correspond to a c -axis compression of approximately 0.5% for the film on NA-sapphire and 0.65% for the film on AN-sapphire. This behavior, also observed by other authors[93, 99], is generally attributed to thermally-induced macrostrain.

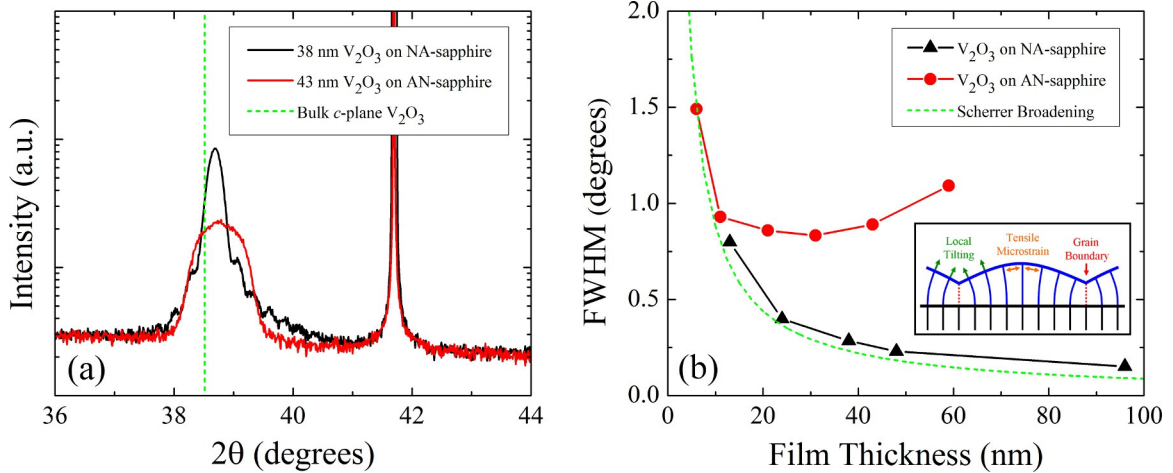


Fig. 5.3 (a) Typical θ - 2θ X-ray diffraction scans showing the (0006) out-of-plane peaks for V_2O_3 films on both NA- and AN-sapphire. The expected peak position for bulk V_2O_3 was taken from JCPDS reference 00-034-0187. (b) A plot versus thickness of the extracted FWHM of V_2O_3 's (0006) peak for films deposited on both NA- and AN-sapphire. Also plotted is the FWHM that would exist purely due to thickness broadening as predicted by the Scherrer equation[111]. The inset cartoon depicts how good epitaxy might lead to island-like growth and various types of peak broadening.

The most striking difference between the XRD data for the films on NA-sapphire and AN-sapphire is the peak width. Fig. 5.3(b) shows a plot of the extracted full width at half maximum (FWHM) values for various thicknesses of V_2O_3 deposited onto both types of substrates. The peaks for the NA-sapphire films are relatively narrow and agree well with the finite thickness broadening predicted by Scherrer's equation[111]:

$$B(2\theta) = \frac{0.94\lambda}{L \cos(\theta)}, \quad (5.1)$$

where $B(2\theta)$ is the FWHM, $\lambda=1.5406 \text{ \AA}$ is the incident X-ray wavelength, and L is the characteristic feature size which in this case is film thickness. This implies that the films grown on NA-sapphire have a very homogeneous and coherent structure. The peaks for the AN-sapphire films, however, show additional symmetric peak broadening, with the width increasing up to beyond one degree for a 59 nm thick film.

One explanation for the broad XRD peaks seen in V_2O_3 films on AN-sapphire is that, assuming good epitaxy, the film might grow in granular islands that bow outward to relieve the compressive stress created at the substrate-film interface. This will lead to three distinct types of peak broadening: 1) mosaicity, or a local tilting of the c -axis, 2) microstrain, causing local variations in the out-of-plane d -spacing parameter, and 3) an increased Scherrer broadening due to a smaller grain size. A depiction of these processes can be seen in the inset of Fig. 5.3(b). Concerning mosaicity, reciprocal lattice maps of the $(10\bar{1}10)$ V_2O_3 peaks collected on both types of films did not show much difference in mosaic spread. Concerning microstrain, the level of d -spacing variation that would have to be present to introduce a FWHM broadening of 1 degree can be estimated at roughly 2.5% using the following equation[112]:

$$\frac{\Delta d}{d_0} = \frac{B(2\theta)\cot(\theta)}{2}. \quad (5.2)$$

This level of d -spacing variation appears unrealistically high, especially considering that, after accounting for the Poisson ratio of V_2O_3 , the in-plane tensile strain would have to be even larger. Concerning the final possibility, namely increased Scherrer broadening, a 1 degree broadening of the FWHM corresponds to a lower bound on crystallite size of 9 nm. This is in reasonable agreement with the 12 nm distance between misfit dislocations that should be expected between V_2O_3 and Al_2O_3 based on their in-plane lattice parameters. Therefore crystallite size appears to be the dominant contributor to the peak broadening observed for the V_2O_3 films on AN-sapphire, but all three mechanisms likely contribute. The films grown on rough, unannealed sapphire substrates perhaps avoid this fate by having a greater number of interface defects that dissipate strain energy and allow the material to grow more two-dimensionally. In support of this hypothesis, we also observed that the XRD peaks for films on NA-sapphire sometimes displayed a global tilt of the V_2O_3 c -axis relative to the sapphire c -axis of up to 0.05 degrees. These tilts did not appear to be correlated with the substrate miscut angle.

A representative selection of the metal-insulator transitions for a number of different thicknesses of V_2O_3 films grown onto NA-sapphire and AN-sapphire substrates

is presented in Fig. 5.4. The films deposited on NA-sapphire show very clear MITs that occur near 140 K and become more pronounced with film thickness. The films deposited on AN-sapphire, however, are much more resistive at room temperature, are semiconducting at all temperatures, and only show a small sign of V_2O_3 's metal-insulator transition which is shifted to a slightly higher onset temperature in the range of 160-170 K. We note that the insulating state resistivities and activation energies of the films grown on both types of substrates are similar, with thicker films generally having a greater low-temperature resistivity.

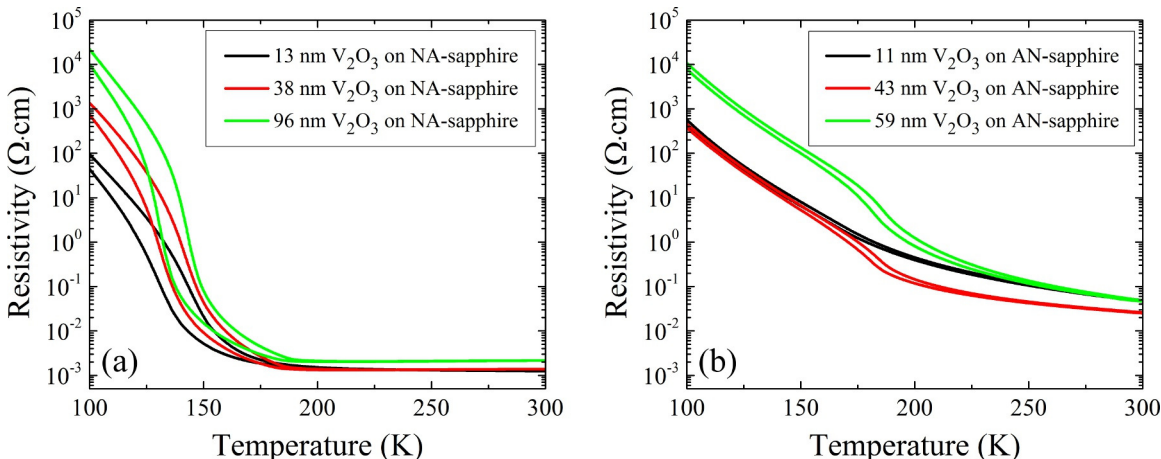


Fig. 5.4 Four-point probe resistivity measurements versus temperature for a representative selection of V_2O_3 film thicknesses deposited onto (a) NA-sapphire and (b) AN-sapphire.

One explanation for the dramatic influence of the V_2O_3 surface morphology on its metal-insulator-transition properties is the slightly increased level of c -axis compression that we observe for the films on AN-sapphire ($\sim 0.65\%$) versus that for films on NA-sapphire ($\sim 0.5\%$). This increased c -axis compression likely arises either from better interface coupling to thermally induced strain or from outwardly-bowing island-like growth. In either case, the result would be a net expansion of the V_2O_3 unit cell, a reduction in electron orbital overlap, and a stabilization of the insulating phase. Also, in Cr-doped V_2O_3 , the insulating phase is known to have a reduced c -axis/ a -axis parameter ratio[36], again consistent with the insulating films grown on AN-sapphire. A second

possible explanation for the suppression of the metallic phase in the films on AN-sapphire could be an increased level of Anderson localization[113] arising from a greater number of substrate-induced defects and a higher level of disorder. Strongly correlated electron systems on the verge of localization are known to be extremely sensitive to defects[4]. A similar effect occurs in Cr-doped V_2O_3 where Cr impurities cause an anomalously large rise in the resistivity of the metallic state prior to the onset of the MIT[114].

To conclude this section, by comparing deposition of V_2O_3 films on annealed and unannealed c -plane sapphire substrates we have demonstrated the surprising degree to which the structural and electronic properties of V_2O_3 depend on the substrate surface morphology and the coherence of the resulting interface. This work reveals a previously unanticipated experimental factor that must be controlled in future studies of V_2O_3 growth, and here we have shown that any attempt to standardize the substrate by a high-temperature anneal will degrade the structural and metal-insulator transition properties of V_2O_3 . It appears that further improvements in the development of ultra-high quality V_2O_3 films will rely on a new substrate material or preparation method. The large mismatch in lattice constants and thermal expansion coefficients introduced by sapphire likely mean that it is not the best choice of substrate for V_2O_3 . Fortunately, the RHEED oscillations we have observed here, combined with the relative smoothness of the films deposited on unannealed substrates, suggests that given an appropriate substrate, V_2O_3 will grow highly two-dimensionally with extremely high quality. Perhaps the commercially available substrate $LiTaO_3$, annealed to have an ultra-smooth surface, combined with a Cr_2O_3 buffer layer is the next most logical choice as a substrate material for V_2O_3 .

5.3 Growth on Unannealed Sapphire(11-20)

We also tested the dependence of growth temperature, oxygen pressure and film thickness for V_2O_3 grown onto a -plane, or $(11\bar{2}0)$ oriented, sapphire substrates. These substrates create a biaxial strain at the interface with V_2O_3 of 4.1% and 7.8%[115]. For

this reason, these films grew more three-dimensionally, as seen in Fig. 5.5. The post-deposition RHEED patterns also showed a very faint 3x1 reconstruction that is perhaps indicative of an additional vanadium oxide phase. These films are therefore much less preferable for voltage-induced switching experiments than those grown on unannealed *c*-plane sapphire substrates. One additional point of interest is that these MBE-grown films appear to have much better electrical properties than PLD-grown films[115].

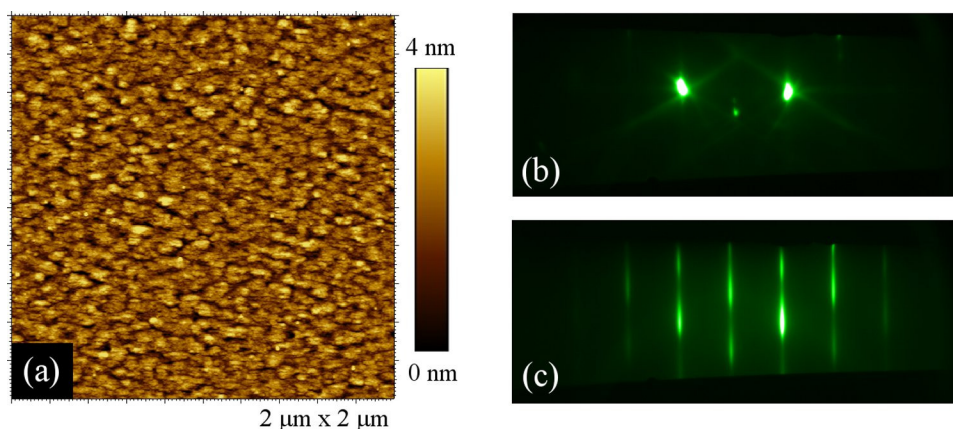


*Fig. 5.5 (a) An AFM image of a nominally 40 nm thick V_2O_3 film on a-plane sapphire grown at 700 °C in the highest O_2 growth pressure tested, 3.8×10^{-7} Torr. The RMS roughness of this film is 7 Å, much higher than for films grown on *c*-plane sapphire. (b,c) Typical RHEED images taken before and near the end of deposition for films on a-plane sapphire. A very faint 3x1 pattern exists in (c), perhaps indicating the formation of a second phase.*

Resistivity versus temperature data and XRD data for a series of roughly 40 nm films grown in different oxygen pressures can be seen in Fig. 5.6(a,b). The same plots for films grown to different thicknesses using an optimized pressure of 4×10^{-8} and 6×10^{-8} can be seen in Fig. 5.6(c,d). These oxygen pressures were chosen from the data in Fig. 5.6(a,b) because they produced the largest metal-insulator transitions near 150 K. From the data in Fig. 5.6(a), it is clear that reducing the oxygen pressure leads to an increase in the metal-insulator transition temperatures, just as previously observed for V_2O_3 films on *c*-plane sapphire substrates. In this case, however, there is a clear co-existence of VO and V_2O_3 in the film with the highest transition temperature that is grown at an oxygen pressure of 1.6×10^{-8} Torr. The film grown at the lowest oxygen pressure of 8.2×10^{-9} Torr appears to be single phase VO. All films have significantly broadened XRD peaks.

From the data in Fig. 5.6(c), it can be seen that increasing the thickness of the V_2O_3 film leads to a sharper metal-insulator transition and an XRD closer to that of bulk V_2O_3 .

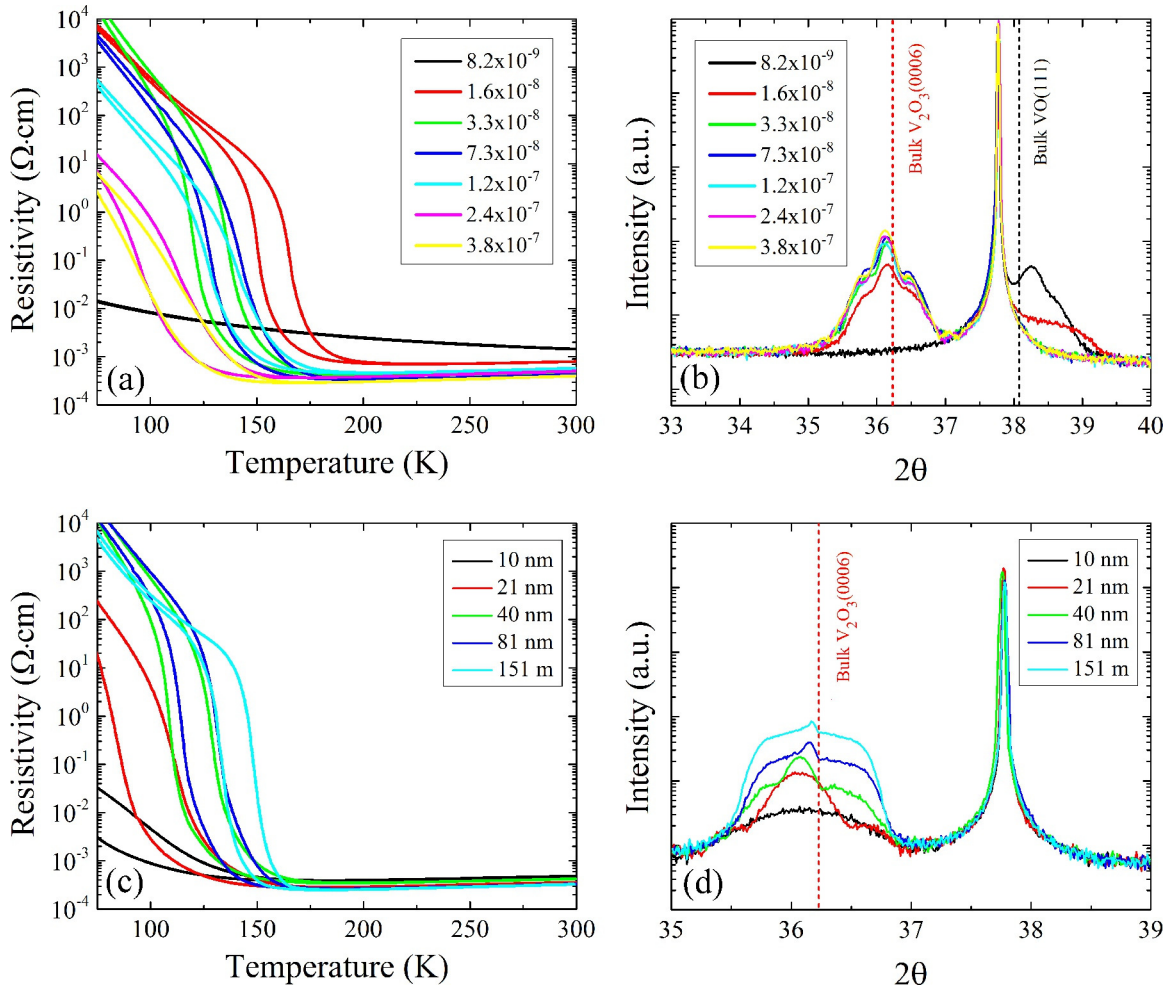


Fig. 5.6 (a,b) Resistivity versus temperature and coupled θ - 2θ XRD scans for V_2O_3 films nominally 40 nm in thickness deposited at 700 °C on a-plane sapphire substrates. (c,d) Resistivity versus temperature and coupled θ - 2θ XRD scans for various thicknesses of V_2O_3 deposited on a-plane sapphire in partial pressures held between 4×10^{-8} and 6×10^{-8} Torr. The V_2O_3 peak positions are consistently shifted to smaller 2θ angles corresponding to a 0.2%-0.4% out-of-plane expansion along the $[11\bar{2}0]$ axis which is generally more pronounced in the thinner films.

As one additional point, all of the 40nm films plotted in Fig. 5.6(a,b) show a 0.2-0.4% out-of-plane d -spacing expansion rather than a contraction, as was observed for the films on c -plane sapphire. This trend can be explained by the observation that the large a -axis thermal expansion coefficient is now directed out-of-plane rather than in-plane, and there is actually a negative thermal expansion coefficient along the c -axis which is now in-plane. These coefficients are summarized for both V_2O_3 and sapphire in Table 5.1. This negative in-plane thermal expansion coefficient along the c -axis of V_2O_3 will lead to a compressive interfacial strain as the film is cooled after deposition. This in-plane compression should then cause the out-of-plane d -spacing to expand as we observe, and it appears to be stronger in thinner films, consistent with an effect arising due to a substrate-film interaction.

| Crystal Axis | Lattice Parameter (Å) | Thermal Expansion Coefficient ($\times 10^{-5} \text{ }^\circ\text{C}^{-1}$) |
|---------------------|------------------------------|--|
| a -axis V_2O_3 | 4.958 | 3.19 |
| c -axis V_2O_3 | 1.3958 | -1.15 |
| a -axis Al_2O_3 | 4.758 | 0.50 |
| c -axis Al_2O_3 | 1.2992 | 0.66 |

Table 5.1 A table, reproduced from Ref[99], showing the thermal expansion coefficients of the a -axes and c -axes of V_2O_3 and Al_2O_3 . The negative c -axis thermal expansion is most likely responsible for the out-of-plane d -spacing expansion we observe for films grown on a -plane sapphire.

To summarize this section, a large biaxial lattice mismatch in V_2O_3 films on a -plane sapphire substrates leads to island-like growth and rough film surfaces. Just as with c -plane substrates, the dominant contributor to strain appears to arise due to thermal stresses. Also, the variation of transition temperature with oxygen pressure that we observed for films on c -plane substrates can be roughly reproduced on a -plane substrates. However, there appears to be a coexistence of V_2O_3 and VO in the film with the highest transition temperature.

5.4 Growth on Annealed LiTaO₃(0001)

In this section we present data for the growth of V₂O₃ on *c*-plane LiTaO₃ substrates. We were originally interested in this substrate because *c*-plane LiTaO₃ has an in-plane lattice parameter of roughly 5.153 Å. At room temperature, this corresponds to a roughly 4% tensile strain at the interface between V₂O₃ and the substrate, opposite to the 4% compressive mismatch provided by *c*-plane sapphire. Additionally, at our chosen growth temperature of 700 °C, the lattice match to sapphire and LiTaO₃ become approximately 5% and 3%, respectively, due to the large *c*-axis thermal expansion coefficient of V₂O₃. V₂O₃ should therefore be able to grow more smoothly and coherently on LiTaO₃ substrates.

We ran into difficulty annealing the substrates to produce ultra-smooth surfaces using a previously reported recipe[103]. Ultimately, we settled on a recipe of etching the substrates in a buffered HF solution for 30 seconds, followed by a 30 second rinse in deionized H₂O, 30 seconds of cleaning in an IPA vapor bath, and 5 minutes of drying in hot nitrogen gas. After this, the substrates were annealed in air at 1100 °C for ten hours. RHEED and AFM characterization of the resulting substrate surface can be seen in Fig. 5.7(a,b). Although atomic terraces are visible, there appears to be some kind of roughness or precipitate forming as well. Annealing at higher temperatures smoothed the surface further, but the atomic steps coalesced into much larger steps multiple atomic layers in height. Annealing at lower temperatures failed to produce any smoothening of the surface at all. Nevertheless, given this starting surfaces, the V₂O₃ films appeared to grow very smoothly and two-dimensionally, as seen in Fig. 5.7(c,d).

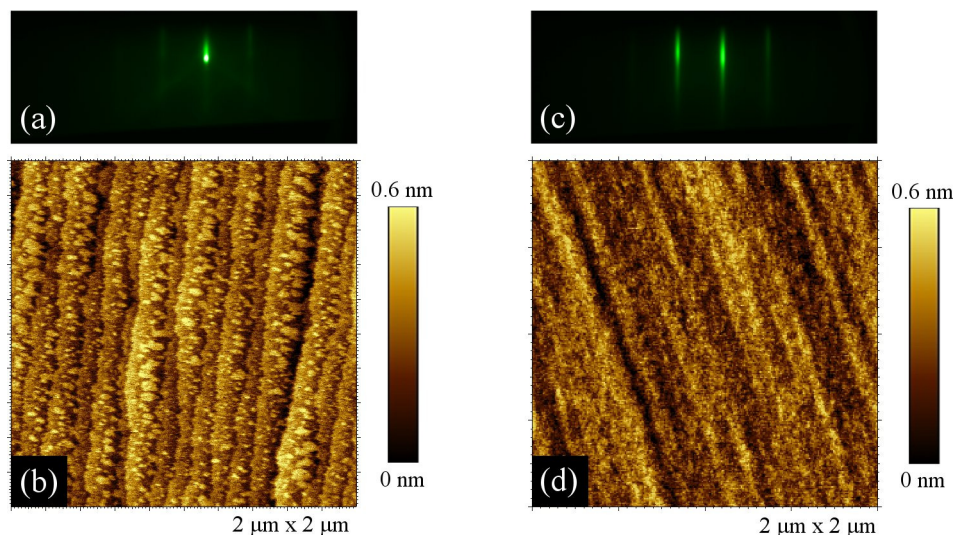


Fig. 5.7 (a,b) RHEED and AFM data for a *c*-plane LiTaO_3 substrate prior to deposition. (c,d) RHEED and AFM data for a nominally 24 nm thick V_2O_3 film on *c*-plane LiTaO_3 . The film appears to grow very two-dimensionally. The RMS roughnesses of images (b) and (d) are 1.3 Å and 1.1 Å, respectively.

We monitored the RHEED streak spacing during growth and noticed that the lattice parameters of V_2O_3 relaxed much more slowly on LiTaO_3 substrates than on sapphire substrates (Fig. 5.8), indicative of better epitaxy. The V_2O_3 films on *c*-plane sapphire fully relaxed in roughly 2 nm, whereas the films on *c*-plane LiTaO_3 fully relaxed in closer to 10 nm. This behavior might arise because of the smaller lattice mismatch provided by LiTaO_3 substrates at 700 °C or simply because the film growth is more accommodating of an interfacial tensile stress than a compressive stress.

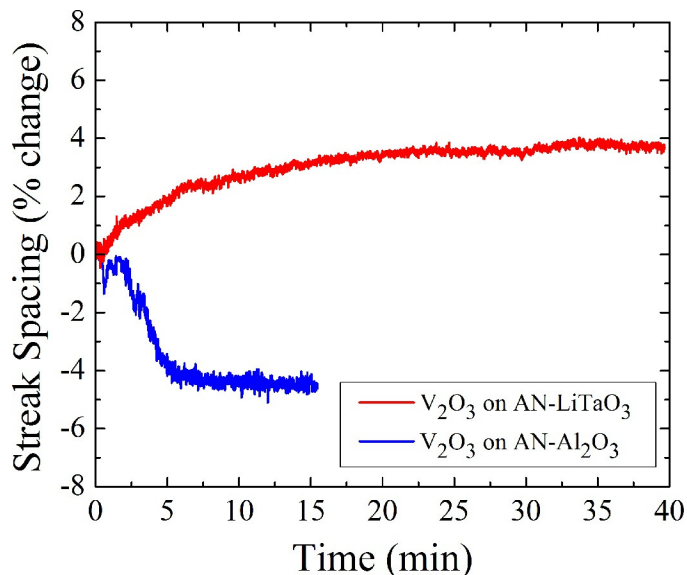


Fig. 5.8 RHEED streak relaxation data for a V_2O_3 film deposited at $700\text{ }^\circ\text{C}$ on an annealed $LiTaO_3$ substrate compared with data for a V_2O_3 film deposited under similar conditions on an annealed c -plane sapphire substrate. 5 minutes of growth corresponds to roughly 2 nm of V_2O_3 thickness. The film on sapphire relaxes in approximately 2 nm. The film on $LiTaO_3$ however, relaxes much more slowly, implying the film is more coherently strained. This could occur either due to the slightly smaller lattice mismatch afforded by $LiTaO_3$ or a greater ability for the film to accommodate tensile strain rather than compressive strain.

In Fig. 5.9 we show resistivity versus temperature data and XRD data for V_2O_3 films of various thicknesses deposited onto annealed c -plane $LiTaO_3$ substrates. The (0006) peak for $LiTaO_3$ is obscured by the (0006) sapphire peak, so we measured the higher-angle (00012) peaks to help differentiate between the film and substrate. These films show a very peculiar dependence of the metal-insulator transition on thickness. Films that were 24 nm in thickness or less showed insulating behavior at all temperatures. Films that were 36 nm in thickness or more showed very nice metal-insulator transitions and a strongly metallic high-temperature state. Correlating this with the XRD data revealed that the insulating behavior in thinner films is accompanied by a contraction of the out-of-plane d -spacing. The magnitude of this d -spacing is difficult to measure due to obstruction from the substrate peak. Thicker films have d -spacing values closer to that of bulk V_2O_3 .

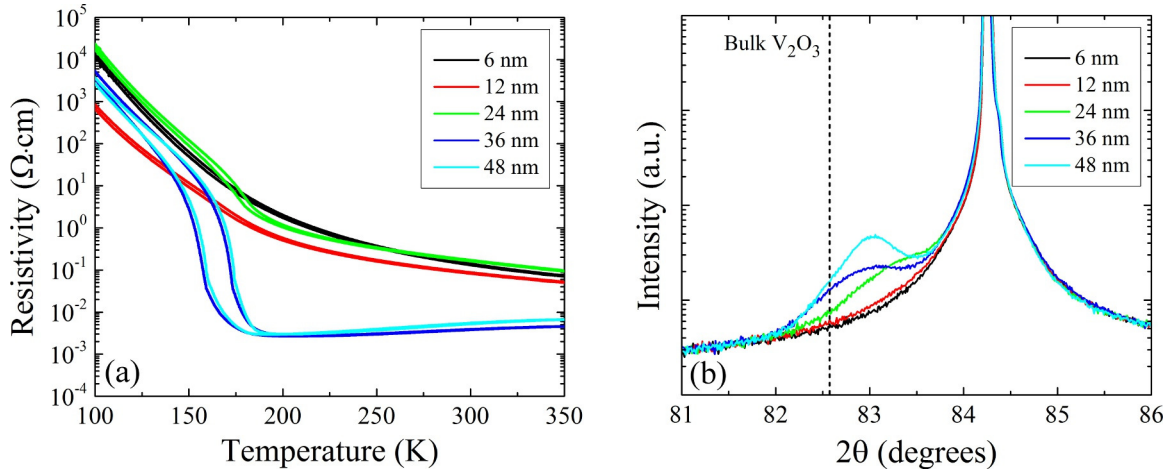


Fig. 5.9 (a) Resistivity versus temperature sweeps, and (b) symmetric θ - 2θ XRD scans collected from V_2O_3 films grown to various thicknesses on annealed c -plane $LiTaO_3$ substrates at $700^\circ C$. The dotted line indicates the bulk crystal value for $d_{(00012)}$ $LiTaO_3$ taken from JCPDS reference 00-029-0836.

Since the RHEED data presented in Fig. 5.8 shows that the V_2O_3 films fully relax in about 10 nm, the residual strain and insulating behavior for the films 24 nm and 36 nm in thickness must arise from thermally induced stress. The greater effect of this stress in these films, as compared to films deposited on unannealed c -plane sapphire, is likely due to better interface coherence, epitaxy and strain transfer.

Although none of these films were used in voltage-induced switching experiments, it appears that V_2O_3 grows extremely two-dimensionally and coherently on $LiTaO_3$. This is an exciting result, and it suggests that extremely high quality V_2O_3 with very nice metal-insulator transition properties could be obtained on $LiTaO_3$ substrates given the right buffer layer. Further work would also need to be done to develop a robust annealing method for the preparation of ultra-smooth $LiTaO_3$ starting surfaces. We believe this would be a promising strategy for future research on the high-quality growth of V_2O_3 .

5.5 Growth on Cr₂O₃-Buffered Sapphire(0001)

In this last section of Chapter 5 we present some initial work we performed on the preparation of Cr₂O₃ buffer layers for the growth of V₂O₃. The *c*-plane surfaces of V₂O₃ and Cr₂O₃ have a nearly perfect lattice match, so we attempted to improve the quality of V₂O₃ growth on annealed *c*-plane sapphire by the use of a thin Cr₂O₃ buffer layer. We will show that this effort was only marginally successful, likely because the residual strain in V₂O₃ is thermal in nature, and not due to the substrate-film lattice mismatch. All V₂O₃ and Cr₂O₃ films were grown in the optimized oxygen pressure range of 2×10^{-7} Torr to 5×10^{-7} Torr, as described in Chapter 4, and all of the *c*-plane sapphire substrates were annealed before growth produce ultra-smooth starting surfaces using the recipe described in Section 5.2.

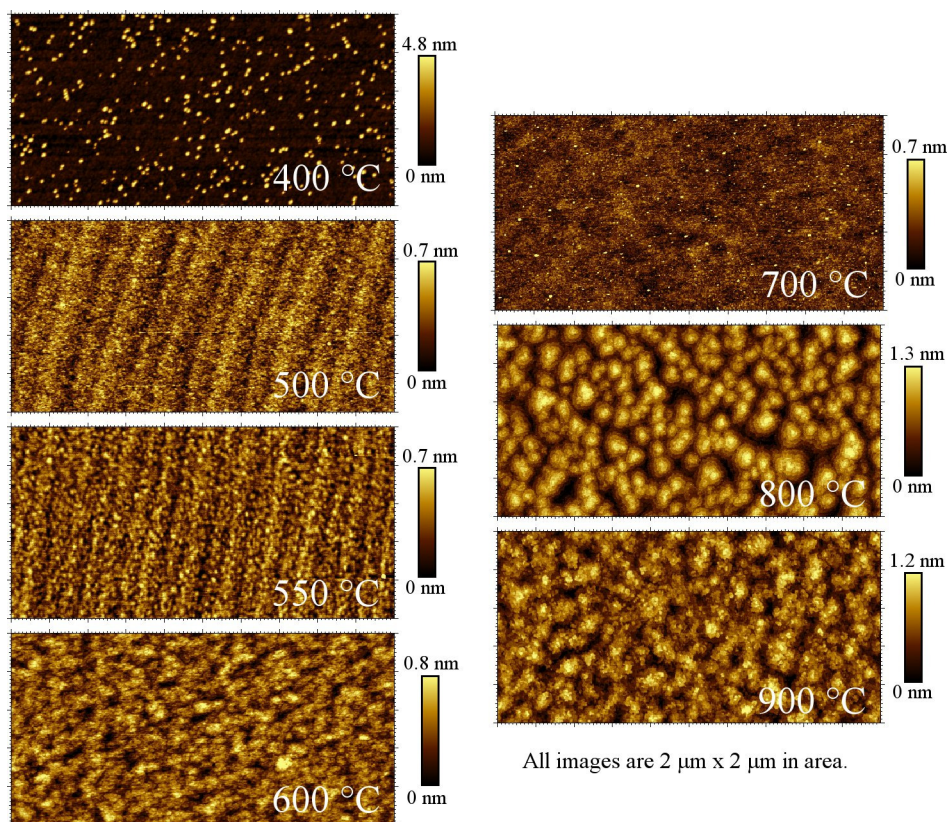


Fig. 5.10 AFM images of the surfaces of Cr₂O₃ buffer layers grown to approximately 40 nm in thickness at growth temperatures ranging between 400 °C and 900 °C.

First, we decided to optimize the growth temperature required for high-quality Cr_2O_3 growth. Fig. 5.10 shows AFM images of approximately 40 nm thick Cr_2O_3 films on annealed *c*-plane sapphire substrates grown at a range of different temperatures between 400 °C and 900 °C. A terraced surface is still faintly visible on the films grown at 500 °C and 550 °C, implying that the growth is the smoothest and most two-dimensional at these temperatures. Fig. 5.11 shows the root-mean-square roughness of these Cr_2O_3 films as a function of growth temperature.

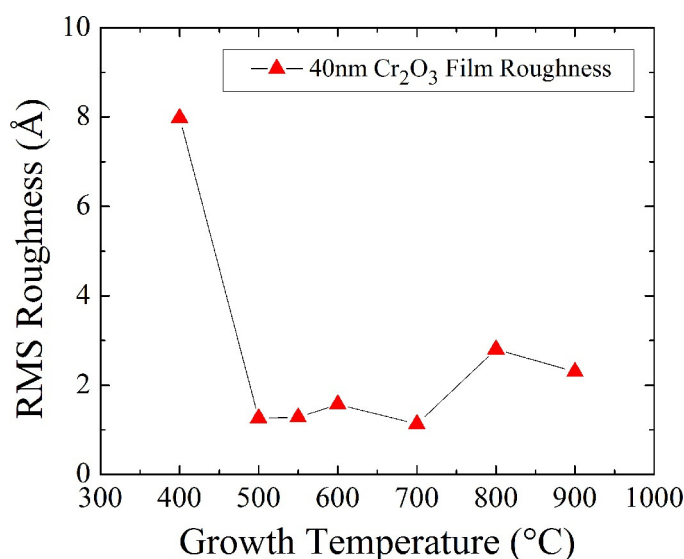


Fig. 5.11 The RMS roughness of Cr_2O_3 buffer layers grown to approximately 40 nm in thickness at a growth temperature of 700 °C.

XRD data collected on these films show a clear connection between the film surface morphology and the out-of-plane *d*-spacing parameter, as seen in Fig. 5.12. The peaks for thicker films deposited at higher temperature typically have a narrower FWHM closer to that of bulk Cr_2O_3 , and the thinner films show significant asymmetric peak broadening likely due to strain relaxation. All films showed only (0001) substrate and film peaks.

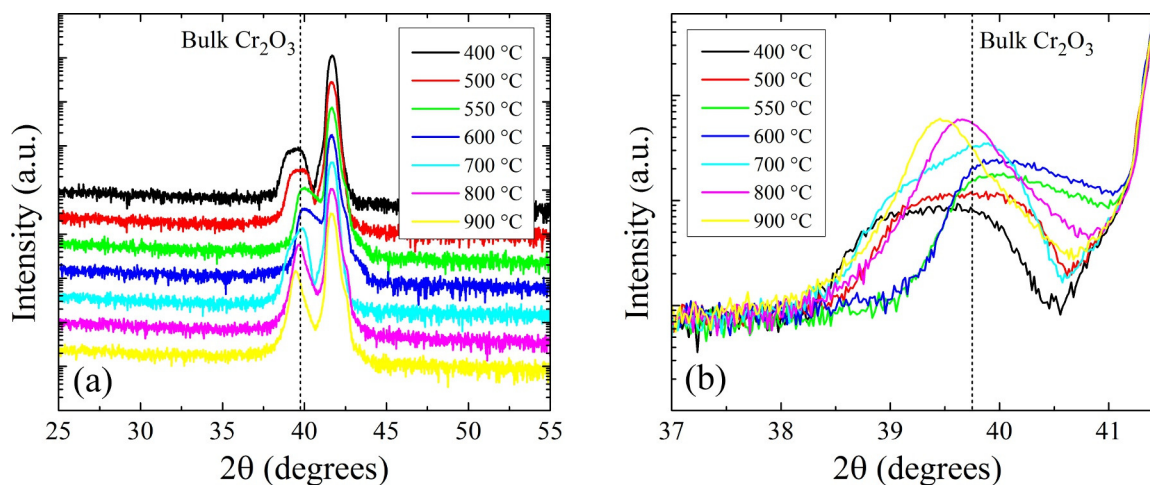


Fig. 5.12 Coupled θ - 2θ XRD scans for nominally 40 nm thick Cr_2O_3 films deposited on annealed c -plane sapphire substrates at various growth temperatures. (Note: these data were collected on a low-resolution general area diffractometer in a coupled-scan mode with no calibration. The spectra were shifted post-measurement to align the substrate peaks to the theoretical bulk values for $\alpha\text{-Al}_2\text{O}_3(0006)$).

Since the Cr_2O_3 at 500 °C appeared to be the smoothest and the Cr_2O_3 at 800 °C appeared to be the roughest, we decided to compare the electrical properties of two very thin 6 nm films of V_2O_3 on thin Cr_2O_3 buffer layers grown at both of these temperatures. Fig. 5.13 shows the metal-insulator transition properties of these films, compared with 6 nm films on annealed c -plane Al_2O_3 and annealed c -plane LiTaO_3 .

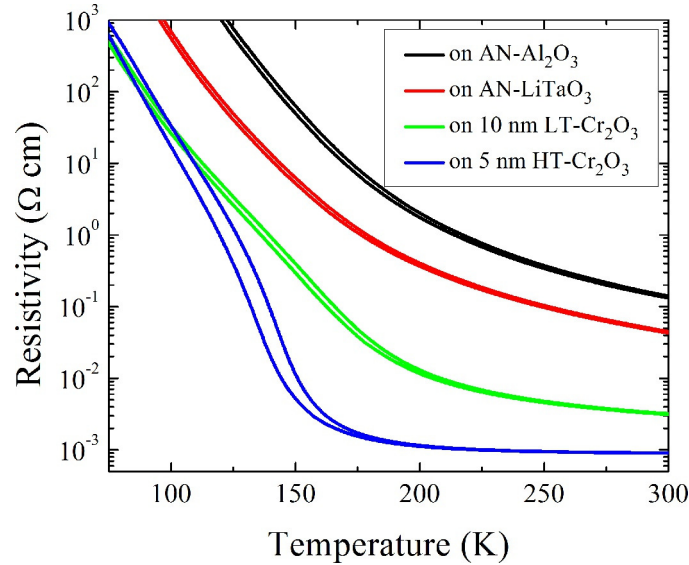


Fig. 5.13 Resistivity versus temperature sweeps for nominally 6 nm thick V_2O_3 thin films deposited at 700 °C onto four different surfaces: AN-sapphire, AN-LiTaO₃, a 10 nm buffer layer of Cr₂O₃ deposited at 500 °C, and a 5 nm buffer layer of Cr₂O₃ deposited at 800 °C.

As we had hoped, the V_2O_3 films deposited on the Cr₂O₃ buffer layers shows an improvement in both the magnitude of the metal-insulator transition and the conductivity of the high-temperature phase. Surprisingly, the V_2O_3 film deposited on the rougher buffer layer that was grown at 800 °C appears to have better properties than the film deposited on the smoother buffer layer deposited at 500 °C. We speculate that, again, this is due to the thermal nature of the residual strain in V_2O_3 films. Strain will transfer more efficiently into films with better registry and coherence to the substrate. The film at 800 °C likely provides a good template for the growth of V_2O_3 while at the same time providing weaker coupling between the lattices of V_2O_3 and Al₂O₃, although further investigation into actual strain levels present in these films would be needed to corroborate this hypothesis.

5.6 Summary

To summarize this chapter, we have presented details of the growth of V_2O_3 on a number of different substrates including annealed c -plane sapphire, unannealed a -plane sapphire, annealed $LiTaO_3$, and Cr_2O_3 -buffered c -plane sapphire. Ultimately, the V_2O_3 films deposited on unannealed c -plane sapphire substrates, which was presented in Chapter 4, proved to have the best structural and electronic properties, and it is those films that we use for the electric field-induced switching experiments discussed in the next chapter. Nevertheless, the work on these other substrates did offer some scientifically interesting results. For example, we showed that annealing the c -plane sapphire substrates prior to deposition to produce ultra-smooth terraced surfaces with atomic-scale step heights ultimately degraded the quality of the V_2O_3 films due to a higher level of epitaxy and strain transfer at the interface. We also showed that V_2O_3 films on a -plane sapphire have an expanded out-of-plane lattice parameter, rather than the contracted one observed for c -plane films. This finding is still consistent with our hypothesis that the stress in V_2O_3 films is predominantly caused by thermal strain. Additionally, the MIT transition temperature of these V_2O_3 films on a -plane sapphire had a dependence on oxygen pressure that was very similar to that which we presented in Chapter 4. Next, we showed how films on annealed c -plane $LiTaO_3$ relax very slowly with thickness and appear to grow very two-dimensionally, leading to a strain-related metal-insulator transition that occurs as a function of film thickness. Finally, we showed that the metal-insulator transition properties of V_2O_3 can be improved by the insertion of a thin Cr_2O_3 buffer layer between the film and substrate. Because a rougher buffer layer yielded a better MIT, it appears that the primary function of this buffer layer is to diminish the strain coupling between the film and substrate rather than to improve the lattice mismatch. We hope all of this work might help to guide future work on the development of a method for producing even higher quality V_2O_3 thin films and interfaces.

Chapter 6

FIELD-EFFECT SWITCHING OF V_2O_3 NANOSTRUCTURES

6.1 Introduction

In this chapter, we present electrical transport measurements performed on V_2O_3 nanostructures at various temperatures ranging from 10 K to 300 K. These experiments consist of direct-current I-V sweeps and time-resolved measurements of the switching time using high-speed pulses. We discuss the DC behavior of the devices in each of three regimes: voltages below threshold, voltages near threshold, and voltages above threshold. Below threshold, we see nonlinear conduction consistent with Poole-Frenkel emission, near threshold we observe voltage-controlled oscillations, and above threshold we see evidence of a hot, conducting filament that expands in size. The high-speed experiments provide a direct measurement of the time required for the V_2O_3 to transform to the conducting state for a given applied electric field above the threshold voltage. The switching is revealed to be a two-stage process consisting of a delay time (or incubation time) before any measurable conduction occurs, followed by an abrupt metallization. Both of these stages occur on the nanosecond timescale. The experimentally measured threshold voltages and incubation times presented in this chapter will be compared in Chapter 7 to predictions from a simple thermal model to evaluate the feasibility of Joule heating as an explanation for the switching process.

6.2 Experimental Setup

Thin films of V_2O_3 approximately 50 nm in thickness were deposited onto *c*-plane sapphire substrates using oxygen plasma-assisted molecular beam epitaxy. The films were grown at a rate of 0.06-0.07 Å/s at a temperature of 700 °C in an oxygen partial pressure of $\sim 3 \times 10^{-7}$ Torr. The deposited films grew epitaxially with the relationship $(0001) V_2O_3 \parallel (0001) Al_2O_3$ and $[11\bar{2}0] V_2O_3 \parallel [11\bar{2}0] Al_2O_3$ as confirmed by RHEED, TEM and XRD analysis. AFM analysis of the film surfaces revealed a root-mean-square roughness less than 2 Å. More details of the film growth process and electrical, structural and chemical characterization of these films can be found in Chapter 4. After deposition, the films were capped *in situ* with 1 nm of Al_2O_3 deposited by magnetron sputtering to help protect the wafer during device fabrication.

Coplanar two-terminal nanogap devices were patterned onto the V_2O_3 films using a combination of electron beam lithography (EBL), optical lithography, argon ion beam etching (IBE), and ion beam deposition (IBD). First, for device isolation and capacitance reduction, IBE was used to carve rectangular V_2O_3 islands 15 μm x 8 μm in size. The areas surrounding the islands were then refilled to a level surface using IBD of Al_2O_3 . Second, 25 nm isolation pads were laid down to isolate the sidewalls of the V_2O_3 mesa structures, which can become damaged during etching. Third, fine contacts of gold (27 nm) on top of a wetting layer of tantalum (3 nm) were laid down using an EBL liftoff process. Lastly, optical lithography was used to define large area contact pads (150 nm) for probing. A ground strip was laid next to the wafer to create a signal-ground transmission geometry. The most useful devices had nominal gap spacings of 75, 125, 175 and 225 nanometers, as measured by a scanning electron microscope. More details of the device fabrication procedure can be found in Section 3.4, and an example of a completed structure can be seen in Fig. 6.1(a).

Patterned devices were measured in a variable-temperature Lakeshore cryogenic probe station equipped with thermally anchored DC-40 GHz probes. An image of one of the high-speed probes landing on the contact pads of a V_2O_3 device can be seen in Fig. 6.1(b). Two different circuitry configurations, depicted in Fig. 6.1(c) were used to perform the high-speed and direct-current measurements. For the DC measurements, a variable load resistance was connected in series with the V_2O_3 device, and a continuous voltage was applied in a staircase sweep using a Keithley 6430 sourcemeter. For the high-speed measurements, the load resistor was removed and a 10300B Picosecond Pulse Labs pulse generator with an intrinsic pulse rise time of 250 ps was used to apply 20 ns long square-wave pulses in a transmission geometry with a digital 12 GHz DSO81204A Agilent oscilloscope to measure the transient response.

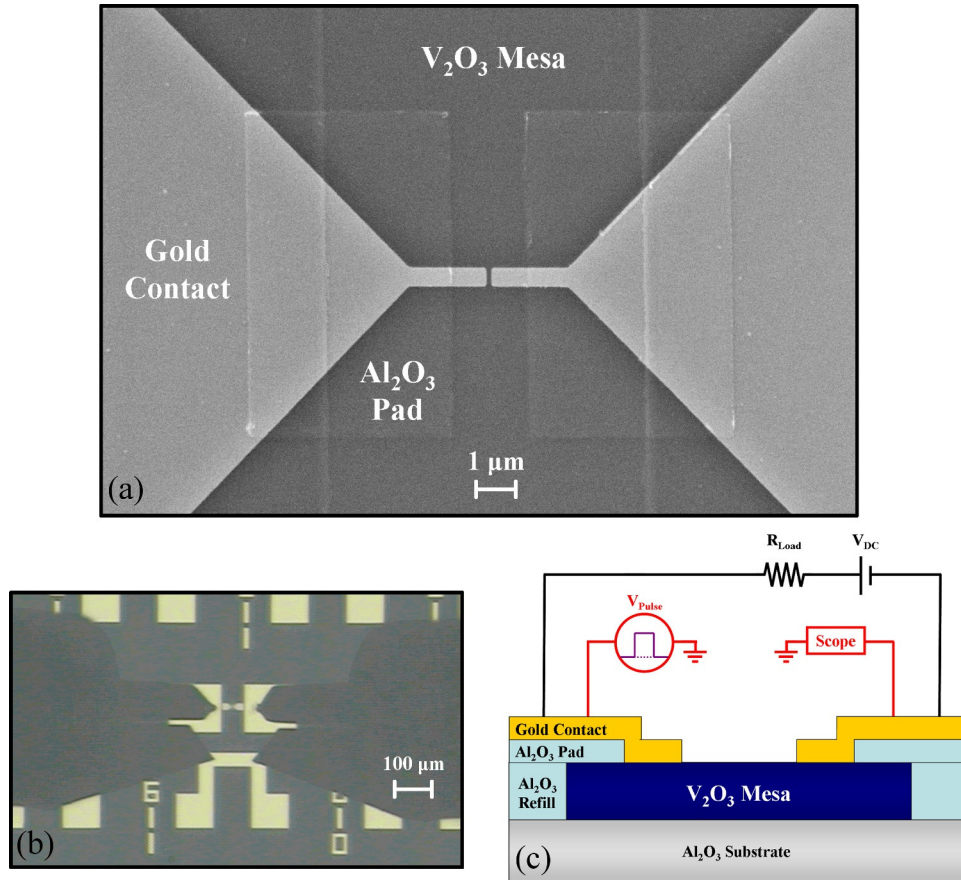


Fig. 6.1 (a) SEM image of a nominally $125\text{ nm} \times 470\text{ nm}$ device. (b) An optical microscope view of two high-speed probes landing on the device and an adjacent grounding strip. (c) A cross-sectional schematic of the V_2O_3 devices showing the two different types of measurements: direct-current and pulsed-voltage.

6.3 Direct Current Switching

Fig. 6.2 shows DC resistance versus temperature data for a nominally $125\text{ nm} \times 470\text{ nm}$ V_2O_3 device taken at various ambient temperatures, along with an inset of the low-bias device resistance as a function of temperature. Above 200 K , the device is fully in the high-temperature metallic state and displays Ohmic conduction. At low temperatures, the V_2O_3 is in the low-temperature insulating state with a resistance far exceeding $1\text{ G}\Omega$ at 10 K . A dramatic voltage-induced switching of the V_2O_3 low-temperature insulating state occurs at a threshold voltage, V_{Th} , which depends on temperature. Also, below V_{Th} and below T_{MIT} , there is a nonlinear dependence of the leakage current on applied voltage. For these DC measurements, a protective load resistance of $10\text{ k}\Omega$ was placed in series, as depicted in Fig. 6.2(a). The purpose of this

load resistance is to limit the current after switching. Experimentally, we apply a circuit voltage ($V_{Circuit}$) and calculate the actual voltage drop across the device (V_{Device}) using Eq. 6.1.

$$V_{Device} = V_{Circuit} - I \cdot R_{Load} \quad (6.1)$$

As the metal-to-insulator transition occurs, some of the voltage drop across the device is transferred to the load resistor, producing the classic S-shaped negative differential resistance curve seen in the low-temperature I-V sweeps of Fig. 6.2(b). In Fig. 6.2(c), we plot the circuit resistance ($R = V_{Circuit}/I$) versus $V_{Circuit}$, and it can be seen that the circuit resistance approaches the load resistance at high bias. Three orders of magnitude change in resistance is observable at V_{Th} for an ambient temperature of 10 K, and it can exceed four orders of magnitude with a lower load resistance. As the temperature is increased, the resistance of the insulating state and the magnitude of V_{Th} decrease, until around 160 K when the V_2O_3 goes through the temperature-driven MIT. For most of our DC experiments, we limited the current and voltage to minimize any potential damage to the often fragile devices. However, if the load resistance is reduced, the hysteresis in the I-V sweeps becomes much more pronounced, presumably due to increased Joule heating and input power $P = IV_{Device}$ being applied after the material has transformed into the metallic phase. The observation of Joule heating contributions after the switching has occurred, however, does not imply that the transition itself is triggered by Joule heating. Most devices were stable at a single temperature for dozens, and even thousands of sweeps, although a combination of changing the ambient temperature and performing voltage sweeps occasionally produced irreversible resistance changes in some devices. Additionally, some devices also displayed a forming voltage, meaning that the first switching event required a threshold voltage 10-20% larger than subsequent switching events. This effect occurred more commonly on 175 nm and 225 nm devices, and less frequently on 75 nm and 125 nm devices. Interestingly, the need for a forming voltage could be restored by warming the device up to room-temperature and then cooling it back down again to low temperature. The 125 nm gap device plotted in Fig. 6.2 was selected for further study because it showed little sign of a forming voltage, and

it was also very stable over many DC and high-speed measurements as a function of temperature.

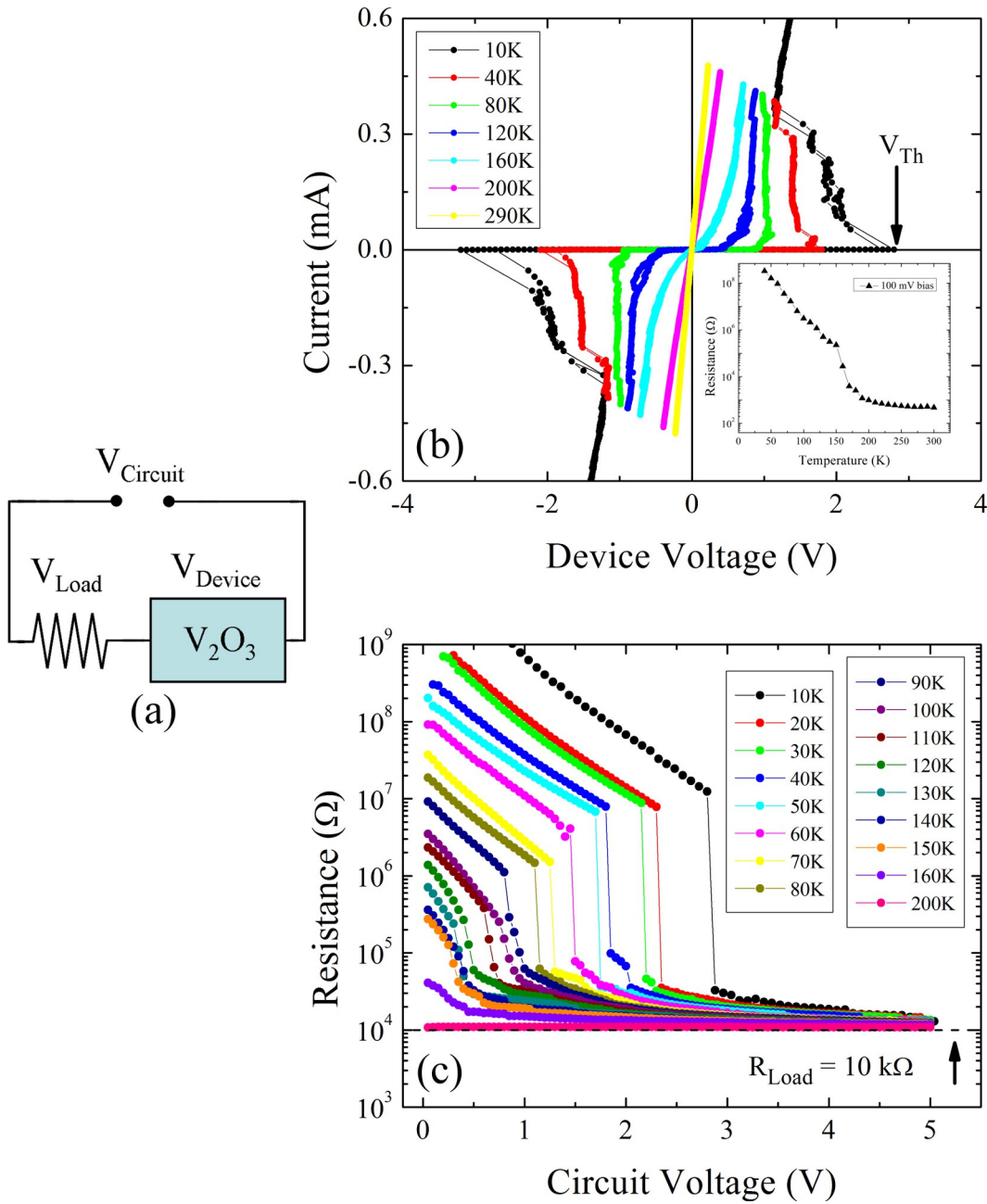


Fig. 6.2 (a) A simple circuit diagram showing the difference between the circuit voltage and the device voltage. Circuit voltages were experimentally measured and converted to device voltages by subtracting the voltage drop across the known external load resistance. (b) Current-voltage sweeps with a 10 k Ω load resistance from a nominally 125 nm x 470 nm device at a range of different temperatures between 10 K and 290 K. (c) Selected sweeps from same device plotted in terms of resistance versus voltage.

Fig. 6.3 shows the threshold device voltages, currents, and input powers for the 125 nm x 470 nm device shown in Fig. 6.2. The threshold is defined to be the highest-bias data point that does not significantly deviate away from the Poole-Frenkel emission behavior that we will discuss in the next section. Each data point and error bar represents the mean and standard deviation from six repeated sweeps. The variation of the threshold voltage from sweep to sweep for a single device typically fell in the range of 10 to 100 mV and was the largest at lower temperature. The threshold current is observed to decrease with temperature, while the threshold current increases. The total input power, however, which is the product of these two quantities, has no clear trend and always stays between roughly 0.5 μW and 2 μW . Previous studies of voltage-induced switching experiments in correlated insulators have claimed this type of data is direct evidence of an electronic mechanism, based on the idea that a thermal switching mechanism should have an input power that decreases with temperature. However, we caution the reader that the threshold powers plotted in Fig. 6.3(c) are only the incipient powers needed to start the switching process. The leakage current and power will both increase as the switching process occurs. It is even conceivable that the observed threshold powers would actually decrease at lower temperatures due to a greater thermal conductivity or a more inhomogeneous defect-activated leakage current.

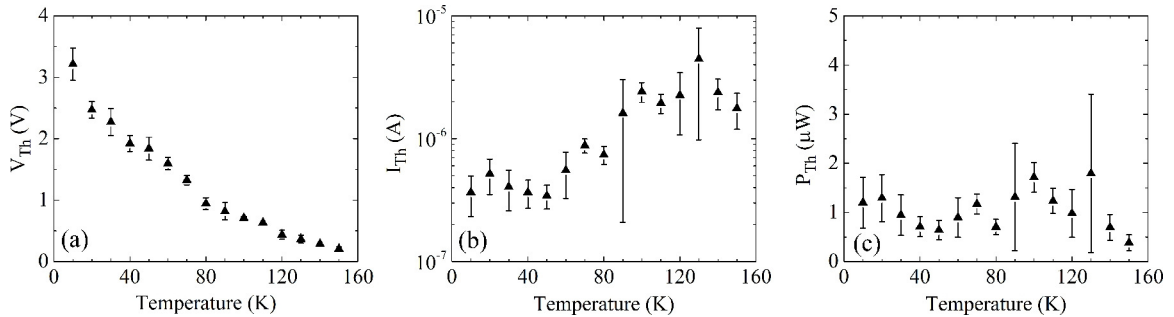


Fig. 6.3 (a) Threshold voltage, (b) threshold current, and (c) threshold power plotted against temperature for a 125 nm x 470 nm device. The data points and error bars represent mean and standard deviations taken from six repeated measurements at each temperature.

To further explore the nature the switching process, we studied the dependence of threshold voltage on gap size for V_2O_3 nanostructures at 10 K. Fig. 6.4 shows threshold voltage data collected from many devices with gap sizes of 75 nm, 125 nm, 175 nm and 225 nm. Each data point and error bar represents the mean and standard deviation extracted from a sample of five devices. A least-squares linear fit to this data passes almost directly through the origin. The slope of this fit gives a threshold electric field at 10 K of 1.9×10^7 V/m. Contact resistances and heat dissipation through the contacts would cause a deviation from this linearity, so we conclude these effects do not play a major role. We also studied the threshold voltage dependence on contact line width for devices 170 nm, 270 nm, 470 nm, and 870 nm wide, but observed no clear trend.

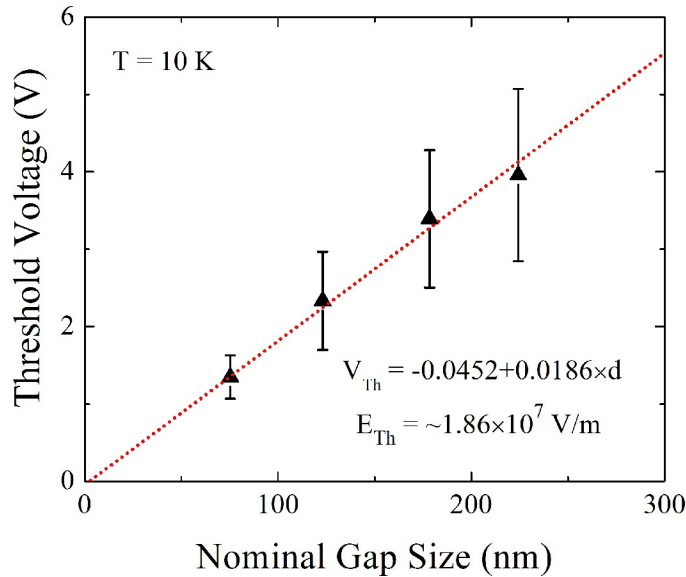


Fig. 6.4 Threshold switching voltages versus nominal gap size extracted from I-V staircase sweeps on V_2O_3 nanostructures at an ambient temperature of 10 K. The data and error bars represent mean and standard deviations from a sample of five different devices at each gap size of 75 nm, 125 nm, 175 nm, and 225 nm. The linear behavior suggests a threshold electric field of approximately 1.9×10^7 V/m at 10 K.

The I-V sweeps pictured in Fig. 6.2(b) can be broken up into three distinct regimes. These regimes are labeled in Fig. 6.5 as A, B and C for an I-V sweep collected at an ambient temperature of 10 K. In A, there is the low-temperature insulating state of

V_2O_3 in which the current has a nonlinear dependence on the applied voltage. In *B*, there is an unstable circuit in which, as we will show, the device oscillates between an insulating state and a conducting state. And in *C*, there is a high-conductance state. In the next three sections, we will look at each of these regimes in more detail.

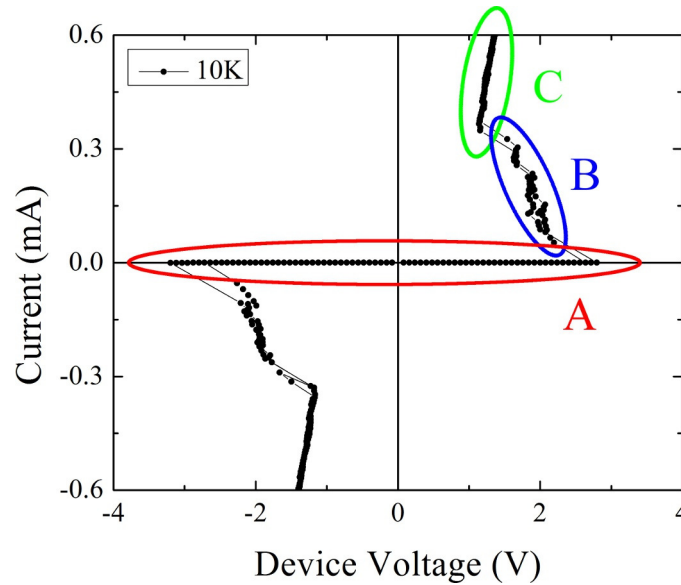


Fig. 6.5 The three different regimes of device behavior. *A*) The low-temperature and low-bias insulating state, *B*) unstable circuit behavior near the threshold voltage, and *C*) the high-temperature and high-bias conducting state. These data were collected on a 125 nm gap V_2O_3 nanostructure at an ambient temperature of 10 K with a series load resistance of 10 k Ω .

6.3.1 $V < V_{Th}$: Nonlinear Conduction

Fig. 6.6 shows a plot of leakage current versus the square root of the device voltage, for the same device presented in Fig. 6.2. Below the threshold voltage, the resulting curves are all very linear at all temperatures below T_{MIT} . The relationship between leakage current and applied voltage is therefore $\ln(I) \propto \sqrt{E}$. This behavior is strongly indicative of Poole-Frenkel emission[81, 82] which has previously been used to describe low-temperature I-V data on VO_2 devices[84-86]. An introduction to this phenomenon is provided as background material in Section 2.5. This behavior allows us to conclude that the device temperature is relatively constant along the I-V sweeps until

the threshold voltage is reached, because any change in temperature would lead to a deviation from this trend. Using this assumption of a nominally constant temperature, we can explicitly parameterize the leakage current $I(V,T)$ as a function of voltage and temperature. This function will be an important component of the Joule heating model we present in Chapter 7.

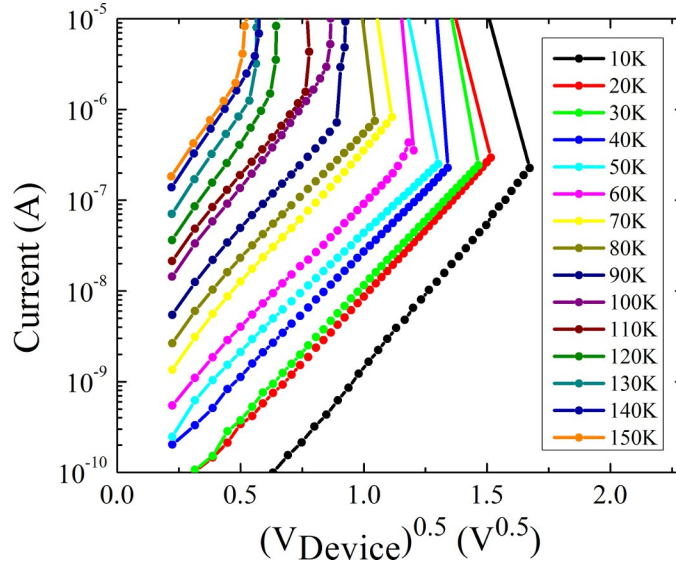


Fig. 6.6 Current plotted against the square root of the device voltage. The resulting linear behavior is a strong indication of a Poole-Frenkel type conduction mechanism with a relatively constant device temperature. The data are from a 125 nm x 470 nm device.

As an aside, one theoretical study[32] of electric field-induced switching in correlated insulators has predicted that the relationship between current and voltage should be described by Eq. 6.2.

$$I(V) = aVe^{\frac{-V_c}{V}} \quad (6.2)$$

We note that our data on these V_2O_3 devices do not follow this trend. However, this does not rule out the possibility of Mott-assisted switching of a different nature.

6.3.2 $V \sim V_{Th}$: Voltage-Induced Oscillations

To investigate the circuit instabilities near V_{Th} , we connected a 1 M Ω high-impedance adapter to our oscilloscope and used it to measure the time-dependence of the voltage drop across the load resistor, as seen in an inset diagram in Fig. 6.7. This configuration is preferable to measuring the voltage drop across the device itself. At low temperatures the device is more resistive than 1 M Ω , and most of the current would be shunted through the oscilloscope.

Fig. 6.7 shows the current in a 75 nm gap V_2O_3 device at 10 K as a function of both circuit voltage and device voltage. Also seen are four different traces for various points along the I-V sweep. The red data point is completely in the insulating state, and the yellow data point is completely in the conducting state. The green and red data points show the device oscillating back and forth between the insulating and the conducting state, and the frequency of oscillation changes with applied voltage. This is the first report of electrical oscillations in V_2O_3 , although oscillations of this type are not a new phenomenon. They have been previously reported in multiple studies of room-temperature VO_2 devices[116-120].

Fig. 6.8(a) shows a map of the circuit behavior as a function of load resistance and applied voltage. Below the threshold voltage, the system is, of course, insulating. And for very large voltages and low load resistances the system is conducting. The region in which oscillations occur falls in between these two conditions. In between the regimes of oscillations and the stable metallic phase, we also observe an unstable phase where the oscillations are intermittent, and perhaps triggered by line noise. Fig. 6.8(b) shows oscilloscope traces from this phase diagram corresponding to load resistances of 50 k Ω . The frequency of the oscillation is clearly seen to increase with time up to 8 V, above which the oscillations become irregular. Fig. 6.8(c) shows how we extracted frequencies from these traces using fast Fourier transforms, and Fig. 6.9(d) shows a plot of these frequencies versus applied voltage for a load resistance of 50 k Ω . The oscillation frequency is tunable over roughly a decade, from 30 kHz to 300 kHz.

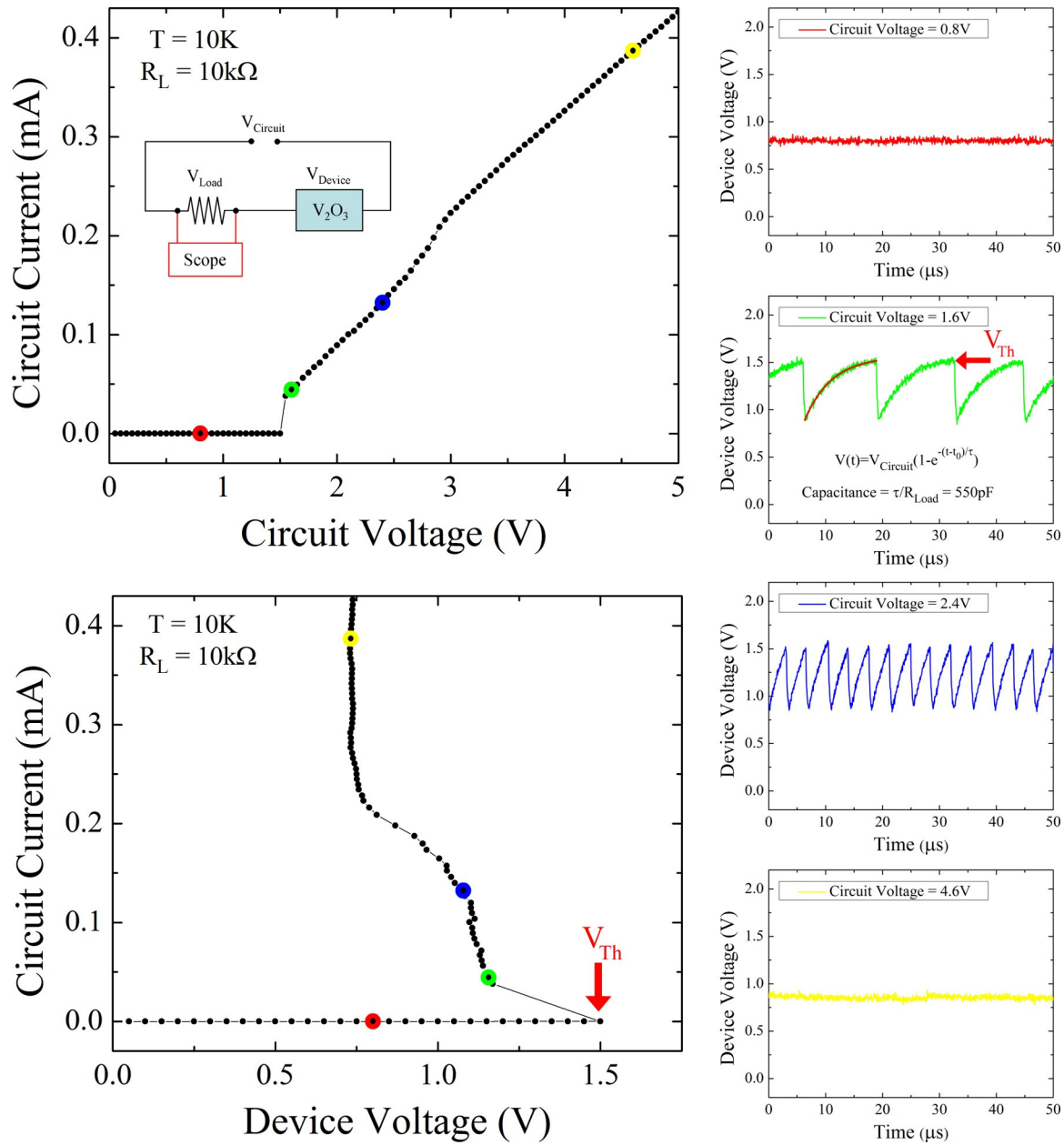


Fig. 6.7 Voltage-controlled oscillations in a $75 \text{ nm} \times 870 \text{ nm}$ device at 10 K . The plots on the left show the current-voltage data as measured by a Keithley source-measure unit, and the plots on the right show the time-dependence of the voltage drop across the V_2O_3 device, deduced from oscilloscope measurements of the voltage drop across the load resistance.

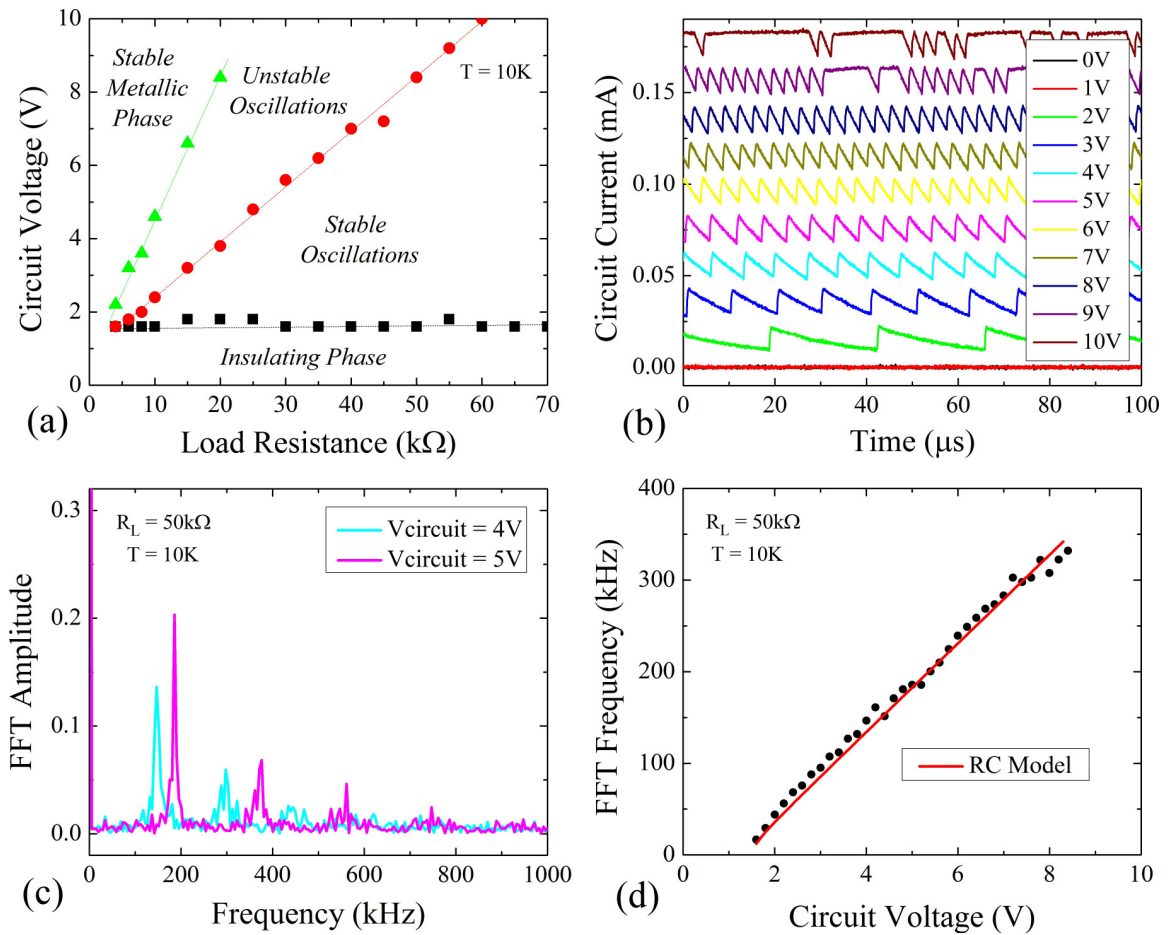


Fig. 6.8 (a) A phase diagram showing the load resistances and voltages required to induce oscillations in the circuit. (b) Oscilloscope traces for a $50 k\Omega$ load resistance. (c) FFTs of the traces at 4V and 5V, demonstrating how we extracted the frequency of oscillation. (d) The frequency of oscillation plotted against circuit voltage for a $50 k\Omega$ load, along with the predicted fit from a simple capacitive charging model.

Our interpretation of the oscillation phenomenon is similar to what happens when a large voltage is applied across an air-gap capacitor. The capacitor plates charge up to the applied voltage until the threshold electric field for ionic breakdown in air is reached. At this point, the air becomes very conducting and the voltage drop across the plates quickly discharges. It turns out that this simple model can be very successfully applied to our V_2O_3 data. Eq. 6.3 describes how the voltage drop across the V_2O_3 should increase

with time in this resistor-capacitor model, and Eq. 6.4 shows the time Δt that can be found by solving for the time it takes for the circuit to charge from some initial voltage to the threshold voltage.

$$V(t - t_0) = V_{circuit} \left(1 - e^{-(t-t_0)/RC}\right) \quad (6.3)$$

$$\Delta t(V_i \rightarrow V_{Th}) = RC \ln \left(\frac{V_{circuit} - V_i}{V_{circuit} - V_{Th}} \right) \quad (6.4)$$

The RC model prediction plotted in Fig. 6.8(d) use the parameters $R = 50 \text{ k}\Omega$, $C = 610 \text{ picofarads}$, $V_{Th} = 1.55 \text{ V}$, and $V_i = 0.87 \text{ V}$. V_{Th} and V_i were determined from the oscilloscope traces in Fig. 6.7. This capacitance value is a realistic number for the self-capacitance of the metallic conductor between the load resistance (which is outside the cryogenic test chamber) and the device. A typical BNC cable, for example, has a self-capacitance of roughly 100 picofarads/m , and the variable resistor we used as a load resistance will contribute as well. The device itself on the other hand should have an extremely small capacitance, which can be approximated by Eq. 6.5.

$$C = \epsilon_r \epsilon_0 \frac{A}{d} \quad (6.5)$$

Taking $\epsilon_r = 100$, $A = 870 \text{ nm} \times 50 \text{ nm}$, and $d = 75 \text{ nm}$, we arrive at a value $C = 5 \times 10^{-16}$ farads, more than a million times smaller than that used in the RC model. The frequency of oscillation therefore appears to be due primarily to the capacitance of the circuitry used to make contact to the V_2O_3 device. It might therefore be exciting to build VO_2 or V_2O_3 oscillators with an on-chip load resistor very close to the switching element. This would greatly reduce the capacitive charging times and might allow the circuit to operate at megahertz frequencies.

6.3.3 $V > V_{Th}$: Filamentary Behavior

Far above the voltage threshold, the device enters a stable metallic state that must correspond to V_2O_3 's high-temperature phase, given the high level of electrical power being input into the device. The conductivity of this metallic state is observed to change in discrete jumps. This behavior is shown in Fig. 6.9 for a 75 nm gap V_2O_3 device at 10 K in series with a load resistance of 2 k Ω . Interestingly, these jumps in conductivity stop occurring when the device resistance reaches the room-temperature resistance. This is strong, albeit indirect, evidence that the jumps in conductivity are due to abrupt expansions of a hot conducting filament. This type of filamentary behavior is expected and has been directly observed previously in larger devices of VO_2 [41, 121, 122].

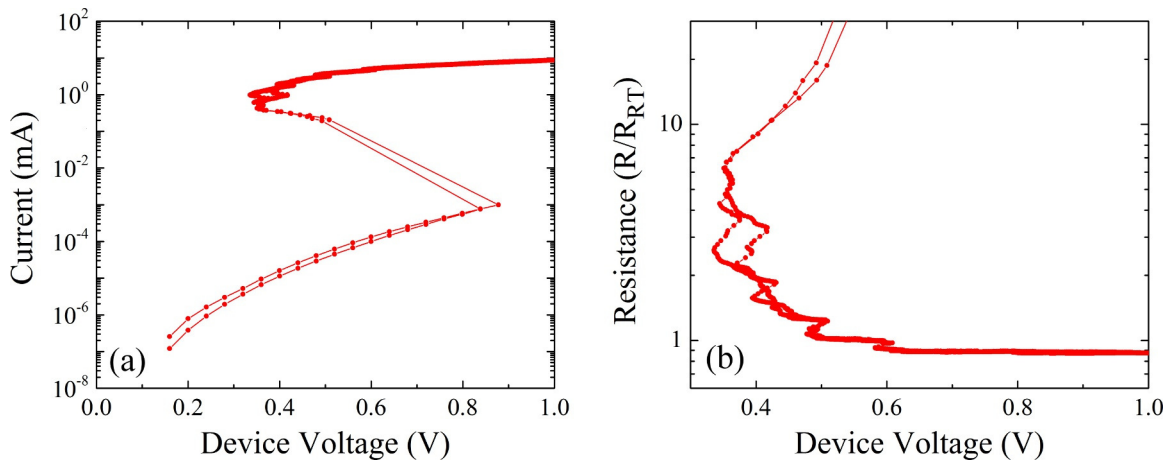


Fig. 6.9 (a) A current-voltage sweep, plotted on a log scale, for a nominally 75 nm x 470 nm device. (b) The same data plotted in terms of resistance, which has been normalized to the room-temperature resistance of the device. In the high-voltage state, increasing voltages cause discrete jumps in resistance that cease to occur once the device has a resistance roughly equal to its high-temperature resistance. This is strong evidence for expansion of a hot conducting filament.

6.4 High-Speed Switching

To measure the speed with which the electric field-induced metallization occurs, we used a high-speed pulse generator and digital oscilloscope to collect transmission measurements of 20 nanosecond square-wave voltage pulses applied to the devices. For these experiments, we removed the series load resistance and used shielded SMA cables, 40 GHz high-speed probes, and a grounding strip adjacent to the V_2O_3 device. The circuitry and a picture of two high-speed probes making contact to a V_2O_3 device in the transmission geometry can be seen in Fig. 6.1(b,c). The band-width of the system was such that a square wave pulse with a 250 ns rise time applied to a shorted device was measured to have a 390 ns rise time. In Fig. 6.10, we present high-speed data for the device of Fig. 6.2. Raw data oscilloscope traces taken at 40 K for 20 ns pulses applied to the V_2O_3 device can be seen in Fig. 6.10(a,b), and Fig. 6.10(c) shows a summary of the incubation times for various temperatures and applied voltages. Note that we have plotted the incubation time versus double the applied voltage. This is because our pulse generator has an output impedance of 50Ω and it is calibrated to produce voltage drops across a 50Ω load. Therefore, as a function of load resistance, the voltage drop across the load increases according to Eq. 6.6. In the limit of large load resistances, as we have for our V_2O_3 devices at low temperature, $V_{Applied} = 2 \cdot V_{Pulse}$.

$$V_{Applied} = \frac{2 \cdot V_{Pulse}}{R_{Load} + 50 \Omega} R_{Load} \quad (6.6)$$

At higher voltages and temperatures, the incubation time appears to be determined primarily by the intrinsic ~390 picosecond pulse rise time of our circuitry. At 80 K and below, the pulse rise times are 1 nanosecond or longer near V_{Th} , meaning these data cannot be attributed to high-frequency losses in the circuitry.

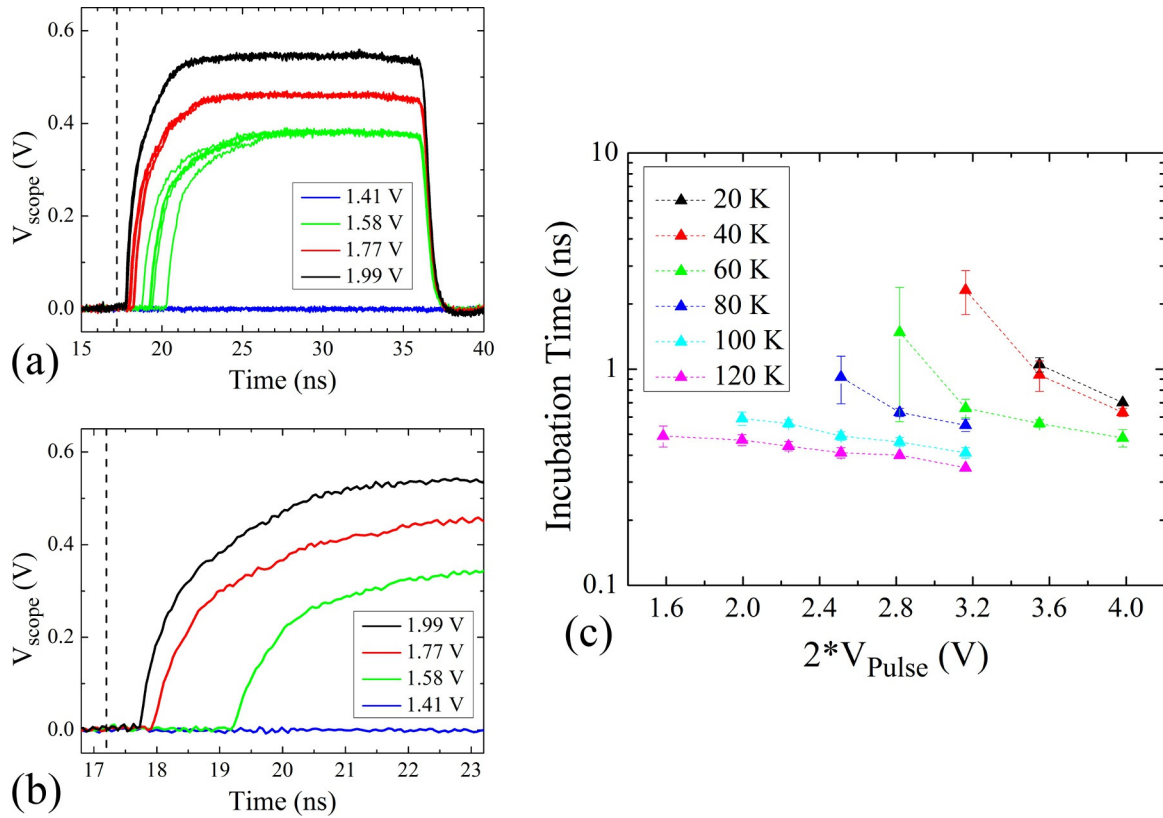


Fig. 6.10 (a,b) High-speed oscilloscope traces taken at 40 K, and (b) experimentally measured incubation times extracted from many of these types of traces at various temperatures. The data points and error bars correspond to mean and standard deviations taken from a sample of five repeated measurements at each temperature.

6.5 Summary

In this chapter we have presented data on the low-temperature electric field-induced switching of V_2O_3 nanostructures. The I-V sweeps consist of three different regimes: *A*) a low-temperature, low-bias insulating state in which the current has a nonlinear dependence on the applied voltage, *B*) voltage-controlled phase oscillations that occur near V_{Th} , and *C*) a high-bias metallic state that appears to be due to a high-temperature conducting filament. Studying the dependence of V_{Th} on device size revealed that switching occurs, on average, at a threshold electric field of 1.9×10^7 V/m. Below V_{Th} , the logarithm of the leakage current is proportional to the square root of the applied voltage, consistent with a Poole-Frenkel-type conduction mechanism. From these fits, we deduced that below V_{Th} the device temperature does not significantly change with applied bias, as this would cause deviations away from the Poole-Frenkel relationship. In the next chapter, this realization will help us to parameterize the effects of electric field and ambient temperature on the leakage current. Finally, high-speed measurements revealed that the switching occurs in a two-stage process consisting of an incubation time and a metallization time, both of which occur on the nanosecond timescale. The experimentally measured threshold voltages and incubation times presented here are important quantities that we will use in the next chapter to evaluate the feasibility of Joule heating as an explanation for the switching process.

Chapter 7

THERMAL MODELING AND COMPARISON TO EXPERIMENT

7.1 Introduction

In this chapter, we hypothesize that a simple thermal model might account for the observed experimental data collected on the electric field-induced switching process in V_2O_3 . We compare models calculated from various different starting assumptions and conclude that, when the effects of positive feedback, heat dissipation, and Poole-Frenkel conductivity enhancements are all properly taken into account, the estimated switching voltages and incubation times match experimental data extremely well. In other words, we find no evidence to support discarding a Joule heating hypothesis, and we conclude that a feedback-enhanced change in device temperature is the most likely triggering mechanism for the observed field-induced switching of the V_2O_3 low-temperature insulating state.

7.2 Failure of a Simple Model

To illustrate how easy it is to underestimate the effect of Joule heating, let us first consider a very simple model in which we calculate the time required for a power equal to the threshold power to uniformly heat a V_2O_3 device from some ambient temperature to a metal-insulator transition temperature of 160 K. For the moment, let us also ignore heat dissipation. To do this, we should solve Eq. 7.1.

$$\Delta t = \int_{T_{Amb}}^{T_{MIT}} \frac{c(T)\rho_m\Omega}{P_{Th}} dT \quad (7.1)$$

We use this model to make predictions for the same device presented in Fig. 6.2. The threshold power, P_{Th} , is therefore 2 μ W, the device volume, Ω , is (50 nm)x(125 nm)x(470 nm), the mass density, ρ_m , is 4870 kg/m³[123], the temperature-dependent specific heat, $c(T)$, is determined from a representative Debye temperature of 600 K supported by previous measurements on bulk samples[124], and we are solving for the incubation time, Δt , required to heat the device from the ambient temperature, T_{Amb} , to

$T_{MIT} = 160$ K. Once the device reaches T_{MIT} , the metallization process will start to occur as further electrical energy is provided for the V_2O_3 latent heat of transformation. Thus, we should not include the latent heat of transformation when calculating just the duration of the incubation time stage of the switching process. The temperature-dependent specific heat we do use is plotted in Fig. 7.1, and it was determined from the classic Debye formula listed below using $T_{Debye} = 600$ K.

$$c_V = 9\alpha k_B \left(\frac{T}{T_{Debye}} \right)^3 \int_0^{T_D/T} x^4 e^x / (e^x - 1)^2 dx \quad [JK^{-1}kg^{-1}] \quad (7.2)$$

$$\alpha = N_{Avogadro} \cdot \left(\frac{5}{0.14988} \right) \quad [kg^{-1}]. \quad (7.3)$$

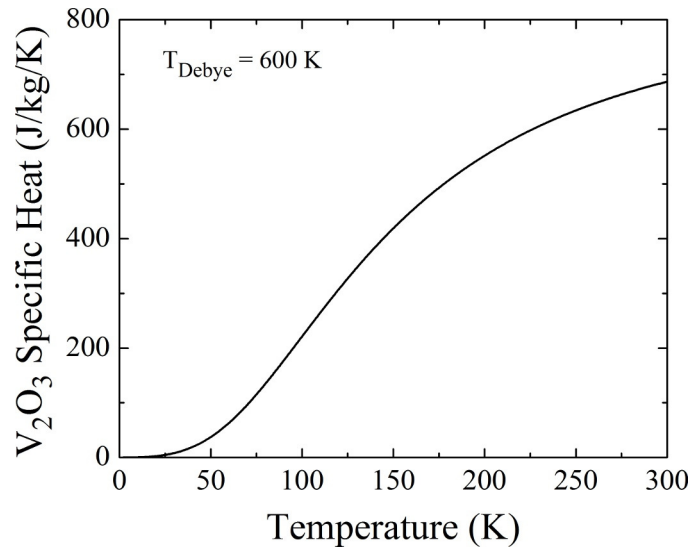


Fig. 7.1 A plot of V_2O_3 's specific heat versus temperature calculated from the Debye equation for a characteristic Debye temperature of 600 K.

The switching time estimates obtained from a numerical integration of Eq. 7.1 are shown in Fig. 7.2 for a range of different ambient temperatures. The predicted incubation times are between 50 and 200 nanoseconds, whereas the experimental incubation times fall between 0.4 and 2 nanoseconds (Fig. 6.10). This is a very large disagreement. Also, it is tempting to argue that this disagreement should be even larger because we neglected heat dissipation, which will slow down the heating process. However, the most important shortcoming of this model is that P_{Th} is not the true total power involved in the switching process. As we discussed in Chapter 6, the threshold power is an underestimate of the total switching power because it does not include any feedback-related increases in leakage current. P_{Th} is the incipient power needed to start the breakdown process. The true input power should therefore be much larger. To improve this model, it is necessary to incorporate the effects of both feedback and heat dissipation.

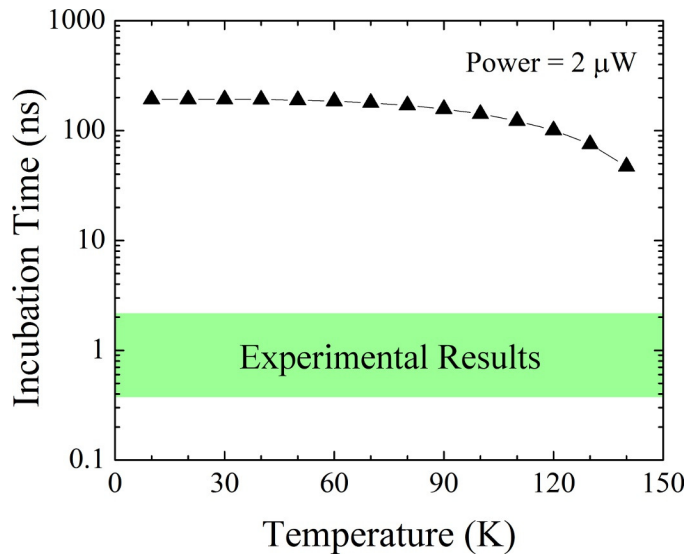


Fig. 7.2 The incubation times predicted from a simple model for the 125 nm x 470 nm device presented in Chapter 7. A constant threshold power of 2 μW was used to calculate the time to heat a V_2O_3 volume of $\Omega = (50\text{nm}) \times (125\text{nm}) \times (470\text{nm})$ from various starting ambient temperatures to V_2O_3 's metal-insulator transition temperature of 160 K. This model includes V_2O_3 's temperature-dependent specific heat, but ignores Poole-Frenkel-type conductivity enhancements, temperature-related feedback effects, and also heat dissipation.

7.3 Incorporating Feedback and Heat Dissipation

To incorporate feedback and heat dissipation we need to use a model with a heating power and a cooling power that can vary with time. To do this, we will use a heating power given by $P_{Heating}(V, T) = I(V, T)V$ and a Newton's law-type cooling power given by $P_{Cooling}(T) = \lambda(T - T_{amb})$, where $I(V, T)$ is determined from a parameterization of the sub-threshold current-voltage relationship plotted in Fig. 6.6. Eq. 7.4 is a differential equation derived from a balance of thermal energy. The energy deposited by Joule heating minus the energy dissipated to the cryostat is equal to the increased thermal energy of the active volume of V_2O_3 .

$$\frac{dT}{dt} = \frac{I(V, T)V - \lambda(T - T_{Amb})}{\rho_m \Omega c(T)} \quad (7.4)$$

In this model, the leakage current and heating power will continuously update throughout the switching process as the device temperature changes, enabling feedback-related heating to occur. One further consideration we include is that the voltage does not turn on instantly, but rather ramps up to the applied voltage sigmoidally with a rise time of 390 ps. We experimentally measured this rise time by applying voltage pulses through a real device with a shorted nanogap. We define the time $t = 0$ to be the 10% level of the sigmoidal voltage ramping function.

To determine the appropriate function for $I(V, T)$, we used Eq. 7.5 to perform a linear fit to six repeated sweeps of the data in Fig. 6.6, which was taken on our 125 nm x 470 nm device.

$$\ln(I(V, T)) = \gamma(T) + \eta(T)\sqrt{V} \quad (7.5)$$

The resulting mean and standard deviations of the constants γ and η , as a function of temperature, can be seen in Fig. 7.3.

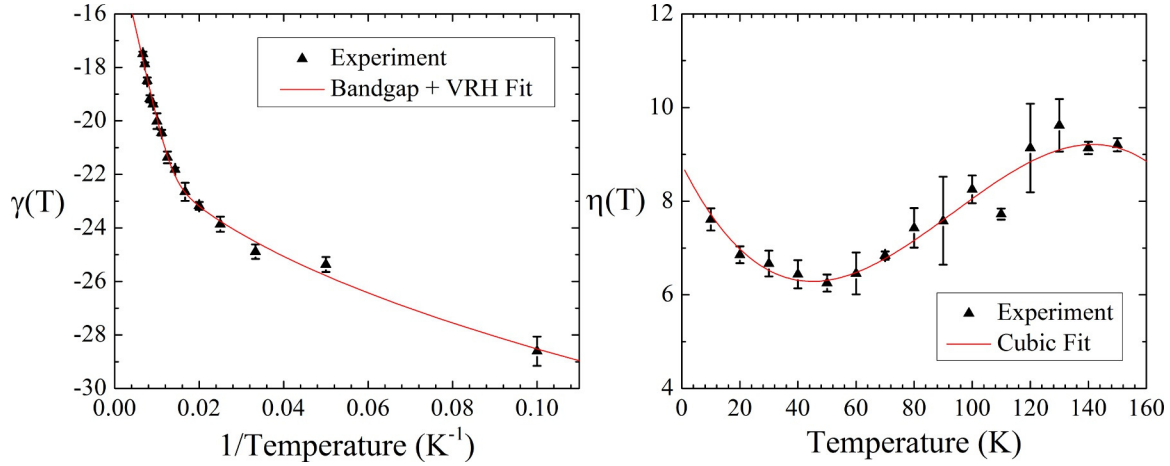


Fig. 7.3 Plots of the current-voltage fitting parameters γ and η , as a function of temperature, extracted from a fit of the equation $\ln(I(V,T)) = \gamma(T) + \eta(T)\sqrt{V}$ to experimental data. The data correspond to the mean and standard deviation of γ and η values extracted from six independent staircase sweeps. The red curves are fits, as described in the text, to be used for smoothly parameterizing these data for use in a numerical Joule heating model.

We would like a continuous functional form for $\gamma(T)$ and $\eta(T)$. So, for the γ data, we chose to fit the data to a sum of a bandgap-like contribution at high temperatures and a variable-range hopping[3] contribution at low temperatures (Eq. 7.6). For the η data, we chose to fit the data with a simple cubic polynomial (Eq. 7.7). The extracted fitting parameters are presented in Table 7.1. The parameterization equation for the current is therefore given by Eq. 7.8.

$$e^{\gamma(T)} = A_1 e^{-\frac{\Delta_B}{k_B T}} + A_2 e^{-\left(\frac{T_0}{T}\right)^p} \quad (7.6)$$

$$\eta(T) = c_1 T^3 + c_2 T^2 + c_3 T + c_4 \quad (7.7)$$

$$I(V,T) = \left(A_1 e^{-\frac{\Delta_B}{k_B T}} + A_2 e^{-\left(\frac{T_0}{T}\right)^p} \right) e^{(c_1 T^3 + c_2 T^2 + c_3 T + c_4)\sqrt{V}} \quad (7.8)$$

| Fitting Results for $\gamma(T)$ | | Fitting Results for $\eta(T)$ | |
|---------------------------------|-----------------------|-------------------------------|------------------------|
| A1 | 2.08×10^{-6} | c1 | -6.50×10^{-6} |
| A2 | 1.87×10^{-8} | c2 | 1.82×10^{-3} |
| Δ_B | 0.06 (eV) | c3 | -0.124 |
| T_0 | 2655 (K) | c4 | 8.79 |
| p | 0.425 | | |

Table. 7.1 Fitting parameters extracted from a least-squares fit of $\gamma(T)$ and $\eta(T)$ based on Eq. 7.6 and Eq. 7.7.

We are reluctant to read too much into the physical significance of the fitting parameters because the fundamental applicability of these conduction models to our devices can easily be questioned. Furthermore it is not well known how the dielectric constant of V_2O_3 varies with temperature, and this quantity makes an appearance in the equation for Poole-Frenkel emission. Our main purpose in establishing this fit is to produce an explicit function for $I(V,T)$ that provides a *good estimate* of the leakage current flowing through the device at a given temperature and voltage. This function can then be used to numerically integrate Eq. 7.4. The final parameterized function for $I(V,T)$, compared to the real experimental data, can be seen in Fig. 7.4.

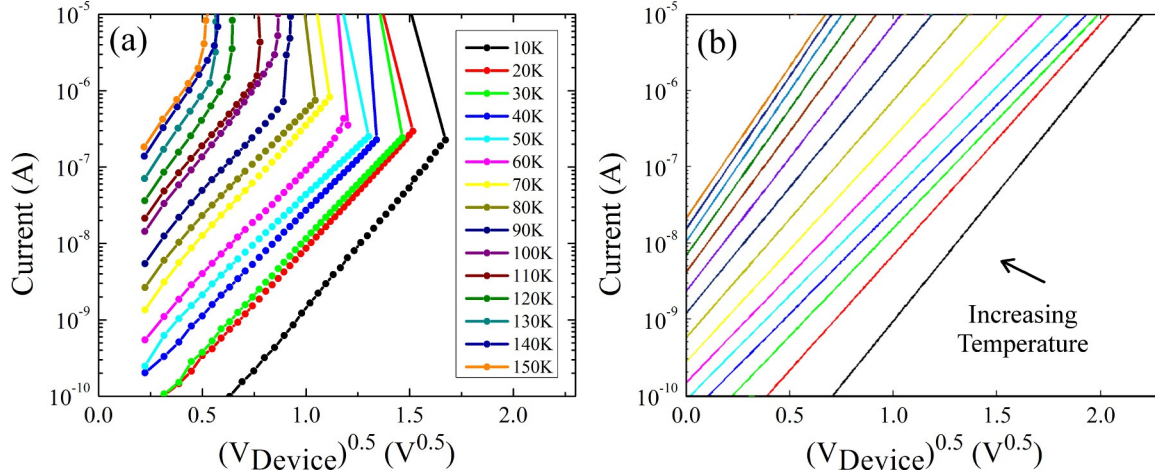


Fig. 7.4 (a) The current-voltage data for a 125 nm x 470 nm device presented in Chapter 7, and (b) our parameterized fit for $I(V,T)$.

Concerning the heat dissipation value λ , we have experimentally determined an upper bound on this quantity of $\lambda = 2.8 \times 10^{-6}$ W/K. This value corresponds to the heat dissipation necessary to maintain a stable temperature $T > T_{MIT}$ in the high-bias metallic state, i.e. $\lambda \leq I^* V^* / (T_{MIT} - T_{Ambient})$ where I^* and V^* are the minimum current and voltages needed to maintain the stable high-conductance state. The current and voltage used for this calculation can be seen in Fig. 7.5. We have chosen this empirical method of estimating the heat dissipation because any *ab initio* calculation would require knowing the thermal resistivity the V_2O_3 thin film and also the interfacial resistivity between the V_2O_3 and the substrate and the contacts. All of these parameters are very difficult to accurately estimate. We would also like to note that, for simplicity, we have assumed that the heat dissipation parameter λ is not temperature-dependent. In general, this will not be true, but any deviations in the heat dissipation parameter should not dramatically change the result of the calculation.

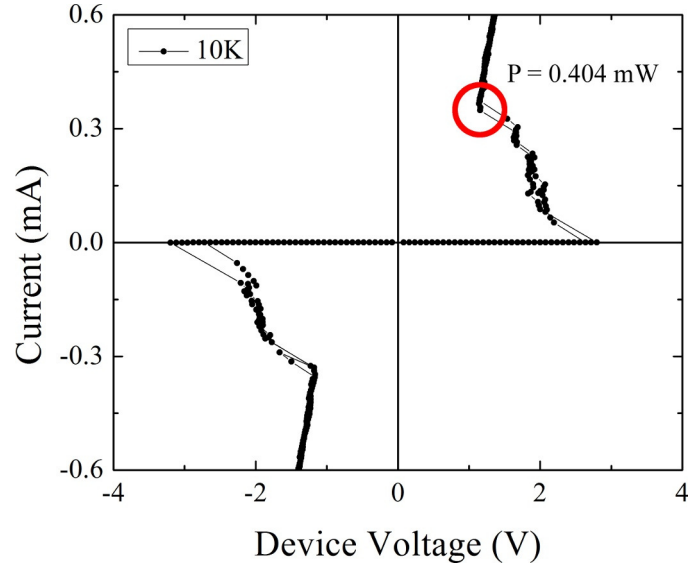


Fig. 7.5 A current-voltage sweep for the 125 nm x 470 nm device presented in chapter 7, showing the condition used to calculate the heat dissipation parameter λ . At the circled point, it is assumed that the device has a temperature $T > 160$ K. The observed input power of 0.404 mW then corresponds to a maximum possible heat dissipation parameter of $\lambda = 2.82 \times 10^{-6}$ W/K.

7.4 Results

Solving Equation 7.4 numerically for $T(t=0) = T_{amb}$ gives solutions for the steady-state device temperature as a function of voltage and the real-time device temperature as a function of time. We made these predictions using various different values of the heat dissipation strength λ for our 125 nm x 470 nm device. Fig. 7.6(a) shows steady-state device temperatures versus voltage for a range of different ambient temperatures, and Fig. 7.6(b) shows device temperatures versus time for a device starting at 20 K under various different applied voltages. The λ value used for these calculations was 2.0×10^{-7} W/K. From these curves we can immediately extract the two experimentally testable parameters of the threshold voltage and the incubation time. Note how the incorporation of the 390 picosecond sigmoidal rise time of the applied voltage pulse leads to a brief dead-time in which very little change in device temperature occurs near $t = 0$.

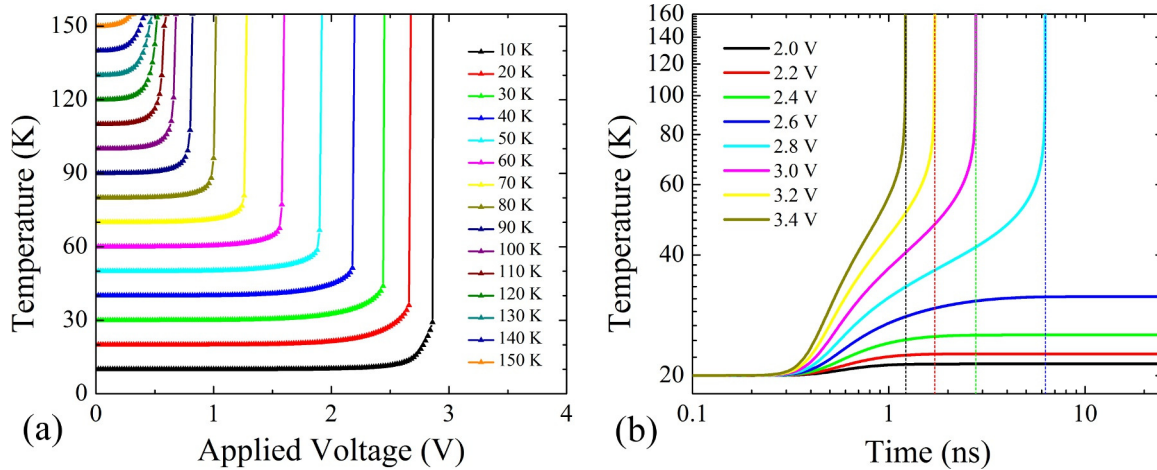


Fig. 7.6 Joule heating simulation results for the $125 \text{ nm} \times 470 \text{ nm}$ device presented in chapter 7: (a) The steady-state device temperature reached for voltages below threshold, and (b) device temperature versus time predictions for voltages near the threshold voltage. These two types of plots allow us to generate threshold voltage and switching time predictions as a function of temperature to compare to experimental data. These curves were generated using a heat dissipation parameter of $\lambda=2.00 \times 10^{-7} \text{ W/K}$. Also, note the effect of the 390 ps pulse rise time in plot (b).

The device temperatures are seen to be nominally constant for voltages below 90% of V_{Th} . This important observation validates the self-consistency of our original assumption that the device temperatures were nominally constant along the Poole-Frenkel emission curves in Fig. 6.6 where $\ln(I) \propto \sqrt{E}$. So temperature-wise, not much changes in the device until the applied voltage gets very close to V_{Th} . When the device temperature finally does change by just a few degrees, a thermal instability develops and the device simultaneously becomes hotter, more conducting, and has more power being deposited into it via Joule heating. As a function of time, the fastest rates of change of the temperature are observed to be near the end of the switching process as the device temperature is approaching T_{MIT} . This is somewhat counterintuitive because the specific heat is greater higher temperatures. However, the increase in specific heat is more than compensated by the dramatic increase in leakage current and input power associated with a higher device temperature.

Fig. 7.7 shows some predictions from our model compared with experimentally measured threshold voltages and incubation times. We have plotted the predictions from

our Joule-heating model for two different representative values of λ . The value $\lambda_{\max} = 2.82 \times 10^{-6}$ W/K corresponds to the maximum possible heat dissipation that can be present in our devices, as discussed previously, and the value $\lambda = 2.00 \times 10^{-7}$ W/K is a number that provides excellent agreement to the experimental data. Even assuming the maximum possible heat dissipation constant of λ_{\max} , we should expect thermally induced switching at a voltage value just 50% greater than that which we observe experimentally. This does not leave much room for a Mott-assisted electric field switching process to occur. Furthermore, if an electronic mechanism is somehow still responsible for the switching process, thermal effects must be playing a significant role as well. More telling is that by decreasing the value of λ to 2.00×10^{-7} , we can very accurately recapture the observed trends in threshold voltage and incubation time, as shown in Fig. 7.7.

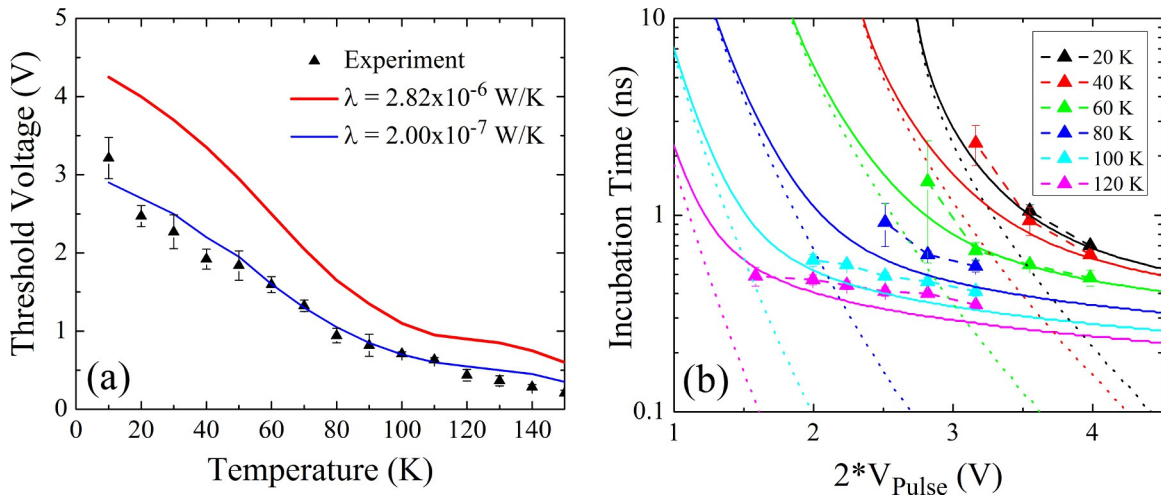


Fig. 7.7 (a) Experimental threshold voltage data compared with predictions from our numerical modeling for two different values of λ . (b) Experimental switching time data compared with predictions from our numerical modeling for a heat dissipation value of $\lambda = 2.0 \times 10^{-7}$. The dotted lines in (b) correspond to an instantaneously fast voltage pulse, and the solid lines correspond to a voltage pulse that turns on with a rise time of 390 picoseconds.

It should be noted that the incubation time values near 390 picoseconds are primarily due to the pulse rise time. The most meaningful incubation time data are the larger ones near 1 nanosecond and above. This does mean that given the right circuitry and a sufficiently large driving voltage, switching times down to 100 picoseconds and

possibly faster should be attainable, even if a thermal mechanism is responsible for the process.

7.5 Summary

In this chapter, we have shown that a relatively straightforward Joule heating model that properly accounts for both temperature-related feedback effects and heat dissipation agrees remarkably well with the observed threshold voltage and incubation time switching data for our V_2O_3 nanostructures. This analysis would imply that Joule heating is the dominant, if not sole, mechanism responsible for the electric field-induced switching of V_2O_3 's low-temperature insulating state. In other words, we find no clear evidence of an electronic or Mott-assisted switching phenomenon.

One potential criticism of our model is that we ignore spatial inhomogeneities and model the entire device channel as having a completely uniform temperature at any given time. However, for a given input power, incorporating a spatially nonuniform temperature profile in the channel will only cause the temperature of some part of the device to be hotter and reach T_{MIT} even faster. In this sense, our method is somewhat conservative and should overestimate the threshold voltages and switching times.

A second possible criticism of our model is that our estimate for the maximum possible heat dissipation parameter is based on an assumption that the entire volume of the device has switched at the lowest voltage values above V_{Th} that correspond to a stable metallic phase (at the values indicated by the red circle in Fig. 7.5). However, in Chapter 6 we made the point that the switching process is filamentary in this regime. If perhaps only 10% of the volume of the device has switched at this point, then the resulting heat dissipation parameter would be an inaccurate representation of the pre-switching heat dissipation parameter. This shortcoming is noted, and we emphasize how well the Joule-heating model recaptures the threshold voltage trends. Extraordinary claims require extraordinary evidence, and any discovery of Mott-assisted electric field-induced switching phenomena will require much stronger evidence than that which we report here.

Chapter 8

CONCLUSIONS AND SUGGESTIONS FOR FUTURE RESEARCH

8.1 Conclusions

In this dissertation, we set out to explore the phenomenon of electric field-induced conductivity switching in two-terminal V_2O_3 nanostructures. This work involved the deposition of high-quality V_2O_3 films, the fabrication of nano-scale contacts onto the surface of these films, and the testing of the electrical response of these devices to both DC and high-frequency voltage pulses. We observed that a threshold electric field of approximately 2×10^7 V/m triggered an abrupt, nanosecond-timescale metallization of V_2O_3 's low-temperature Mott insulating in a manner qualitatively similar to previous reported experimental results on VO_2 [22] and Fe_3O_4 [29]. The most important finding of our work was that the magnitude of the observed threshold voltages and the speed at which the switching occurred were both consistent with a simple Joule heating model that properly accounted for temperature-related feedback and Poole-Frenkel-type conductivity enhancements. This strongly suggests that carrier density-related Mott switching effects do not play a significant role in the field-induced switching process of V_2O_3 , as has been previously conjectured for VO_2 and Fe_3O_4 . Originally, we had anticipated that the existence of Mott-related switching effects would be clearer in V_2O_3 than in these other materials, due to the high resistance and low level of leakage current provided by the insulating state of V_2O_3 .

Our conclusion that Joule heating plays an important role in the electric field-induced switching of V_2O_3 has three important implications. First, it implies that no voltage-induced switching would occur without the temperature-driven metal-insulator phase transition in V_2O_3 . Without the temperature-driven MIT, the devices would still experience a threshold voltage-triggered thermal runaway, but the lack of a stable high-conductance state to transform into means they would break upon switching. Sadly, this dims the prospect of searching for electric field-induced switching in Mott insulators that do not display temperature-driven transitions. Second, it means that the switching process will likely have a limited durability due to cracking and stress associated with the V_2O_3 structural phase transition. Third, it suggests that the switching process will never be ultra-fast. Even ignoring the specific heat and latent heat of transformation in V_2O_3 , the switching process would be limited by the timescale of electron-phonon interactions, whereas a purely electronic process could potentially happen much faster and be of great

scientific interest. Nevertheless, our modeling suggests that, given the appropriate high-speed circuitry, V_2O_3 devices should be thermally switchable in less than 100 picoseconds. If these switching speeds are also achievable in VO_2 at room temperature, it would still be fast enough for integration into today's logic and memory applications, perhaps as an access device for reducing off-state leakage currents.

Although the ultimate goal of this research was to explore the origin of electric field-induced switching, along the way we stumbled across a number of scientifically interesting findings. We showed in Chapter 4 that by decreasing the oxygen pressure supplied during the growth of V_2O_3 , we could systematically increase the metal-insulator transition temperature up to approximately 180 K. We attributed this effect to a continuous change in stoichiometry, consistent with the trend of decreased metal-insulator transition temperatures previously reported for bulk crystals of vanadium-deficient $V_{2(1-x)}O_3$. In Chapter 5, we also demonstrated a very surprising disorder-induced localization effect when V_2O_3 was grown on *c*-plane sapphire annealed prior to growth to have an ultra-smooth surface. We attributed this behavior to increased strain transfer due to a more coherent substrate-film interface. Lastly, in Chapter 6, we reported the first observation of voltage-controlled oscillations in V_2O_3 nanostructures, and found that the circuit dynamics matched very well with predictions for a simple resistor-capacitor model.

8.2 Suggestions for Future Research

We would like to caution that our results do not mean Mott-related switching effects are completely absent in V_2O_3 . There are several possible ways in which an electric field effect might still exist, and they all offer exciting avenues for further research.

First, we have only explored field strengths below roughly 4×10^7 V/m. We have no knowledge of how V_2O_3 might respond at higher fields. These dynamics could perhaps be measured using an optical pump-probe technique, similar to that previously explored in VO_2 [33, 34], to study the response of V_2O_3 on a timescale faster than that over which Joule heating occurs.

Second, we explored only a two-terminal configuration. In a three-terminal, gated structure there would ideally be no Joule heating, allowing for a more direct investigation of the effect of electrostatic doping on the transport properties of V_2O_3 . V_2O_3 could perhaps even serve as an archetypal example of a strongly correlated electron material for these types of experiments because it displays such a dramatic metal-insulator transition. Such a project, however, will be very challenging. The method has previously been attempted on VO_2 devices with little success. In one report[125], HfO_2 was used as a gate dielectric and only a 6% change in conductivity was observed with an applied gate voltage. Furthermore, the changes in conductivity were hysteretic, an indication that they might ultimately be due to electrochemical reactions and changes in phase or oxidation state at the oxide- VO_2 interface.

Finally, it is possible that the leakage currents we observed are due to defects and impurities introduced during the thin film growth process, and perhaps the effect of Joule heating could be reduced in higher quality samples, allowing Mott-related switching behavior to be more easily detectable. Field-induced switching aside, the growth of ultra-high quality V_2O_3 films would be worthy of future research in its own right simply because so much remains to be learned about the effect of strain on the metal-insulator transition in V_2O_3 . To date almost all V_2O_3 films are grown on *c*-plane sapphire, and they structurally relax after just a few monolayers due to the large 4% in-plane lattice mismatch between *c*-plane V_2O_3 and sapphire. In fact, most of the strain present in a typical V_2O_3 film arises upon cooling the film back to room temperature due to the difference in thermal expansion coefficients of V_2O_3 and sapphire. In our work, we have shown that substrate $LiTaO_3$ appears to be a much better choice for V_2O_3 since the lattice spacing for V_2O_3 films on $LiTaO_3$ relaxes much more slowly, as seen in Fig. 5.8. Thicker films on $LiTaO_3$ also had a more metallic high-temperature state, as seen in Fig. 5.9, suggestive of fewer localization-inducing defects. We therefore believe it would be a worthwhile venture to attempt to grow coherent and nearly strain-free V_2O_3 on top of Cr_2O_3 -buffered $LiTaO_3$ substrates. Many new discoveries first start with extremely high quality materials.

REFERENCES:

- [1] G. E. Moore, "Cramming More Components onto Integrated Circuits," *Electronics*, IEEE **38** (1965).
- [2] R. H. Dennard *et al.*, "Design of ion-implanted MOSFET's with very small physical dimensions," *Solid-State Circuits* **9** (1974).
- [3] N. F. Mott, *Metal-Insulator Transitions* (Taylor & Francis, London, 1990).
- [4] M. Imada, A. Fujimori, and Y. Tokura, "Metal-insulator transitions," *Rev. Mod. Phys.* **70** (1998).
- [5] C. Zhou *et al.*, "A field effect transistor based on the Mott transition in a molecular layer," *Appl. Phys. Lett.* **70** (1997).
- [6] D. M. Newns *et al.*, "Mott transition field effect transistor," *Appl. Phys. Lett.* **73** (1998).
- [7] J. G. Bednorz, and K. A. Müller, "Possible High T_c Superconductivity in the Ba-La-Cu-O System," *Zeitschrift für Physik B Condens. Matt.* **64** (1986).
- [8] Y. Kamihara *et al.*, "Iron-Based Layered Superconductor $\text{La}[\text{O}_{1-x}\text{F}_x]\text{FeAs}$ ($x = 0.05\text{--}0.12$) with $T_c = 26$ K," *J. Amer. Chem. Soc.* **130** (2008).
- [9] R. E. Cohen, "Origin of ferroelectricity in perovskite oxides," *Nature* **358** (1992).
- [10] J. H. Park *et al.*, "Direct evidence for a half-metallic ferromagnet," *Nature* **392** (1998).
- [11] Y. Tokura, and Y. Tomioka, "Colossal magnetoresistive manganites," *J. Magnetism and Magnetic Mater.* **200** (1999).
- [12] C. H. Ahn, J. M. Triscone, and J. Mannhart, "Electric field effect in correlated oxide systems," *Nature* **424** (2003).
- [13] C. H. Ahn *et al.*, "Electrostatic modification of novel materials," *Rev. Mod. Phys.* **78** (2006).
- [14] A. Ohtomo, and H. Y. Hwang, "A high-mobility electron gas at the $\text{LaAlO}_3/\text{SrTiO}_3$ heterointerface," *Nature* **427** (2004).
- [15] S. Thiel *et al.*, "Tunable Quasi-Two-Dimensional Electron Gases in Oxide Heterostructures," *Science* **313** (2006).
- [16] H. Shimotani *et al.*, "Insulator-to-metal transition in ZnO by electric double layer gating," *Appl. Phys. Lett.* **91** (2007).

- [17] K. Ueno *et al.*, "Electric-field-induced superconductivity in an insulator," *Nat. Mater.* **7** (2008).
- [18] J. T. Ye *et al.*, "Liquid-gated interface superconductivity on an atomically flat film," *Nat. Mater.* **9** (2010).
- [19] Y. Yamada *et al.*, "Electrically Induced Ferromagnetism at Room Temperature in Cobalt-Doped Titanium Dioxide," *Science* **332** (2011).
- [20] R. Kötz, and M. Carlen, "Principles and applications of electrochemical capacitors," *Electrochimica Acta* **45** (2000).
- [21] J. C. Duchene *et al.*, "Initiation of switching in VO₂ Coplanar devices," *Electron Devices, IEEE Trans.* **18** (1971).
- [22] G. Stefanovich, A. Pergament, and D. Stefanovich, "Electrical switching and Mott transition in VO₂," *J. Phys.: Condens. Matt.* **12** (2000).
- [23] H. T. Kim *et al.*, "Mechanism and observation of Mott transition in VO₂-based two- and three-terminal devices," *New J. Phys.* **6** (2004).
- [24] V. N. Andreev, A. G. Aronov, and F. A. Chudnovski, "The Phase Transformation in V₂O₃ in an Electric Field," *Sov. Phys. Uspekhi* **14** (1972).
- [25] F. A. Chudnovskii *et al.*, "Switching phenomena in chromium-doped vanadium sesquioxide," *J. Appl. Phys.* **84** (1998).
- [26] A. Asamitsu *et al.*, "Current switching of resistive states in magnetoresistive manganites," *Nature* **388** (1997).
- [27] S. Yamanouchi, Y. Taguchi, and Y. Tokura, "Dielectric Breakdown of the Insulating Charge-Ordered State in La_{2-x}Sr_xNiO₄," *Phys. Rev. Lett.* **83** (1999).
- [28] Y. Taguchi, T. Matsumoto, and Y. Tokura, "Dielectric breakdown of one-dimensional Mott insulators Sr₂CuO₃ and SrCuO₂," *Phys. Rev. B* **62** (2000).
- [29] S. Lee *et al.*, "Electrically driven phase transition in magnetite nanostructures," *Nat. Mater.* **7** (2008).
- [30] N. Sugimoto, S. Onoda, and N. Nagaosa, "Field-induced metal-insulator transition and switching phenomenon in correlated insulators," *Phys. Rev. B* **78** (2008).
- [31] M. Eckstein, T. Oka, and P. Werner, "Dielectric Breakdown of Mott Insulators in Dynamical Mean-Field Theory," *Phys. Rev. Lett.* **105** (2010).

- [32] F. Heidrich-Meisner *et al.*, "Nonequilibrium electronic transport in a one-dimensional Mott insulator," *Phys. Rev. B* **82** (2010).
- [33] A. Cavalleri *et al.*, "Femtosecond Structural Dynamics in VO₂ During an Ultrafast Solid-Solid Phase Transition," *Phys. Rev. Lett.* **87** (2001).
- [34] A. Cavalleri *et al.*, "Evidence for a structurally-driven insulator-to-metal transition in VO₂: A view from the ultrafast timescale," *Phys. Rev. B* **70** (2004).
- [35] P. D. Dernier, and M. Marezio, "Crystal Structure of the Low-Temperature Antiferromagnetic Phase of V₂O₃," *Phys. Rev. B* **2** (1970).
- [36] D. B. McWhan *et al.*, "Metal-Insulator Transitions in Pure and Doped V₂O₃," *Phys. Rev. B* **7** (1973).
- [37] T. Oka, and H. Aoki, edited by B. K. Chakrabarti, K. K. Bardhan, and A. K. Sen (Springer Berlin / Heidelberg, 2009).
- [38] J. Zaanen, G. A. Sawatzky, and J. W. Allen, "Band gaps and electronic structure of transition-metal compounds," *Phys. Rev. Lett.* **55** (1985).
- [39] J. B. Torrance *et al.*, "Systematic study of insulator-metal transitions in perovskites RNiO₃ (R=Pr,Nd,Sm,Eu) due to closing of charge-transfer gap," *Phys. Rev. B* **45** (1992).
- [40] A. E. Bocquet *et al.*, "Electronic structure of early 3d-transition-metal oxides by analysis of the 2p core-level photoemission spectra," *Phys. Rev. B* **53** (1996).
- [41] C. N. Berglund, "Thermal Filaments in Vanadium Dioxide," *Electron Devices, IEEE Trans.* **16** (1969).
- [42] G. B. Adam, and J. C. Duchene, "Electro Thermal Initiation of Switching in Sandwich Structures," *Solid State Comm.* **9** (1971).
- [43] G. B. Adam, and J. C. Duchene, "Pulse Investigation of Switching Delays in VO₂ Coplanar Devices," *Electron Devices, IEEE Trans.* **19** (1972).
- [44] A. Mansingh, and R. Singh, "The mechanism of electrical threshold switching in VO₂ crystals," *J. Phys. C: Solid State Phys.* **13** (1980).
- [45] A. Mansingh, R. Singh, and S. B. Krupanidhi, "Electrical Switching in Single Crystal VO₂," *Solid-State Elec.* **23** (1980).
- [46] S. R. Ovshinsky, "Reversible Electrical Switching Phenomena in Disordered Structures," *Phys. Rev. Lett.* **21** (1968).

- [47] M. P. Shaw, "Thermal Instability - The Precursor to Switching in Inhomogeneous Thin Films," *Electron Devices, IEEE Trans.* **26** (1979).
- [48] D. Adler, H. K. Henisch, and S. N. Mott, "The mechanism of threshold switching in amorphous alloys," *Rev. Mod. Phys.* **50** (1978).
- [49] H.-T. Kim *et al.*, "Raman study of electric-field-induced first-order metal-insulator transition in VO₂-based devices," *Appl. Phys. Lett.* **86** (2005).
- [50] B.-G. Chae *et al.*, "Abrupt metal-insulator transition observed in VO₂ thin films induced by a switching voltage pulse," *Physica B: Condens. Matt.* **369** (2005).
- [51] K. Okimura, and J. Sakai, "Time-dependent Characteristics of Electric Field-induced Metal-Insulator Transition of Planer VO₂/c-Al₂O₃ Structure," *Jpn J. Appl. Phys.* **46** (2007).
- [52] J. Cao *et al.*, "Constant threshold resistivity in the metal-insulator transition of VO₂," *Phys. Rev. B* **82** (2010).
- [53] X. Zhong *et al.*, "Avalanche breakdown in microscale VO₂ structures," *J. Appl. Phys.* **110** (2011).
- [54] G. Gopalakrishnan, D. Ruzmetov, and S. Ramanathan, "On the triggering mechanism for the metal-insulator transition in thin film VO₂ devices: electric field versus thermal effects," *J. Mater. Science* (2009).
- [55] T. Oka, R. Arita, and H. Aoki, "Breakdown of a Mott Insulator: A Nonadiabatic Tunneling Mechanism," *Phys. Rev. Lett.* **91** (2003).
- [56] T. Oka, R. Arita, and H. Aoki, "Nonlinear transport in a one-dimensional Mott insulator in strong electric fields," *Physica B: Condens. Matt.* **359-361** (2005).
- [57] H. Kuwamoto, J. M. Honig, and J. Appel, "Electrical properties of the (V_{1-x}Cr_x)₂O₃ system," *Phys. Rev. B* **22** (1980).
- [58] Y. Ueda, K. Kosuge, and S. Kachi, "Phase Diagram and Some Physical Properties of V₂O_{3+x}," *J. Solid State Chem.* **31** (1980).
- [59] S. A. Shivashankar, and J. M. Honig, "Metal-antiferromagnetic insulator transition in V₂O₃ alloys," *Phys. Rev. B* **28** (1983).
- [60] P. Pfalzer *et al.*, "Structural precursor to the metal-insulator transition in V₂O₃," *Phys. Rev. B* **73** (2006).

- [61] M. S. Laad, L. Craco, and E. Müller-Hartmann, "Orbital-selective insulator-metal transition in V_2O_3 under external pressure," *Phys. Rev. B* **73** (2006).
- [62] F. Rodolakis *et al.*, "Inequivalent Routes across the Mott Transition in V_2O_3 Explored by X-Ray Absorption," *Phys. Rev. Lett.* **104** (2010).
- [63] D. B. McWhan, and J. P. Remeika, "Metal-Insulator Transition in $(V_{1-x}Cr_x)_2O_3$," *Phys. Rev. B* **2** (1970).
- [64] S. Y. Ezhov *et al.*, "Orbital Occupation, Local Spin, and Exchange Interactions in V_2O_3 ," *Phys. Rev. Lett.* **83** (1999).
- [65] K. Held *et al.*, "Mott-Hubbard Metal-Insulator Transition in Paramagnetic V_2O_3 : An LDA+DMFT(QMC) Study," *Phys. Rev. Lett.* **86** (2001).
- [66] M. J. Rozenberg *et al.*, "Optical Conductivity in Mott-Hubbard Systems," *Phys. Rev. Lett.* **75** (1995).
- [67] C. Castellani, C. R. Natoli, and J. Ranninger, "Magnetic structure of V_2O_3 in the insulating phase," *Phys. Rev. B* **18** (1978).
- [68] C. Castellani, C. R. Natoli, and J. Ranninger, "Insulating phase of V_2O_3 : An attempt at a realistic calculation," *Phys. Rev. B* **18** (1978).
- [69] C. Castellani, C. R. Natoli, and J. Ranninger, "Metal-insulator transition in pure and Cr-doped V_2O_3 ," *Phys. Rev. B* **18** (1978).
- [70] W. Bao *et al.*, "Dramatic Switching of Magnetic Exchange in a Classic Transition Metal Oxide: Evidence for Orbital Ordering," *Phys. Rev. Lett.* **78** (1997).
- [71] P. Pfalzer *et al.*, "Local symmetry breaking in paramagnetic insulating $(Al,V)_2O_3$," *Phys. Rev. B* **66** (2002).
- [72] I. Balberg, "Empirical band scheme for rhombohedral V_2O_3 ," *Phys. Lett. A* **43** (1973).
- [73] J. B. Goodenough, "Metallic oxides," *Prog. in Solid State Chem.* **5** (1971).
- [74] J. M. Honig *et al.*, "Study of V_2O_3 by X-Ray Photoelectron Spectroscopy," *Phys. Rev. B* **6** (1972).
- [75] F. J. Morin, "Oxides Which Show a Metal-to-Insulator Transition at the Neel Temperature," *Phys. Rev. Lett.* **3** (1959).
- [76] U. Schwingenschlögl, and V. Eyert, "The vanadium Magnéli phases V_nO_{2n-1} ," *Annalen der Physik* **13** (2004).

- [77] H. A. Wriedt, "V-O Phase Diagram," ASM Alloy Phase Diagrams Center (1990).
- [78] J. Schwinger, "On Gauge Invariance and Vacuum Polarization," *Phys. Rev.* **82** (1951).
- [79] C. Zener, "A Theory of the Electrical Breakdown of Solid Dielectrics," *Proc. of the Royal Soc. of London. Series A* **145** (1934).
- [80] S. D. Ganichev *et al.*, "Distinction between the Poole-Frenkel and tunneling models of electric-field-stimulated carrier emission from deep levels in semiconductors," *Phys. Rev. B* **61** (2000).
- [81] J. Frenkel, "On Pre-Breakdown Phenomena in Insulators and Electronic Semiconductors," *Phys. Rev.* **54** (1938).
- [82] A. K. Jonscher, "Electronic Properties of Amorphous Dielectric Films," *Thin Solid Films* **1** (1967).
- [83] R. B. Hall, "The Poole-Frenkel Effect," *Thin Solid Films* **8** (1971).
- [84] P. Boriskov *et al.*, "The Effect of Electric Field on Metal-Insulator Phase Transition in Vanadium Dioxide," *Tech. Phys. Lett.* **28** (2002).
- [85] G. Golan *et al.*, "Investigation of Phase Transition Mechanism in Vanadium Oxide Thin Films," *J. of Opto. and Adv. Mat.* **6** (2004).
- [86] C. Ko, and S. Ramanathan, "Observation of electric field-assisted phase transition in thin film vanadium oxide in a metal-oxide-semiconductor device geometry," *Appl. Phys. Lett.* **93** (2008).
- [87] G. Dearnaley, A. M. Stoneham, and D. V. Morgan, "Electrical phenomena in amorphous oxide films," *Rep. on Prog. in Phys.* **33** (1970).
- [88] K. D. Rogers, J. A. Coath, and M. C. Lovell, "Characterization of epitaxially grown films of vanadium oxides," *J. Appl. Phys.* **70** (1991).
- [89] B. Sass *et al.*, "Structural and electronic properties of epitaxial V₂O₃ thin films," *J. Phys.: Condens. Matt.* **16** (2004).
- [90] F. C. Case, "A novel deposition technique for switchable vanadium sesquioxide (V₂O₃) thin films," *J. Vac. Sci. Technol. A* **9** (1991).
- [91] H. Schuler *et al.*, "Influence of strain on the electronic properties of epitaxial V₂O₃ thin films," *Thin Solid Films* **299** (1997).

- [92] H. Niehus *et al.*, "Atomically resolved interface structure of a vanadium sesquioxide(0001) film grown on Cu₃Au(001)," *Surf. Sci.* **602** (2008).
- [93] L. Dillemans *et al.*, "Correlation between strain and the metal–insulator transition in epitaxial V₂O₃ thin films grown by Molecular Beam Epitaxy," *Thin Solid Films* (2011).
- [94] Q. Guo *et al.*, "Ordered binary oxide films of V₂O₃(0001) on Al₂O₃," *J. Vac. Sci. Technol. A* **17** (1999).
- [95] Q. Luo, Q. L. Guo, and E. G. Wang, "Thickness-dependent metal–insulator transition in V₂O₃ ultrathin films," *Appl. Phys. Lett.* **84** (2004).
- [96] P. A. Metcalf *et al.*, "Electrical, structural, and optical properties of Cr-doped and non-stoichiometric V₂O₃ thin films," *Thin Solid Films* **515** (2007).
- [97] S. Autier-Laurent *et al.*, "Strain-induced pressure effect in pulsed laser deposited thin films of the strongly correlated oxide V₂O₃," *Phys. Rev. B* **74** (2006).
- [98] C. Grygiel *et al.*, "Thickness dependence of the electronic properties in V₂O₃ thin films," *Appl. Phys. Lett.* **91** (2007).
- [99] B. S. Allimi *et al.*, "Growth of V₂O₃ thin films on a-plane (110) and c-plane (001) sapphire via pulsed-laser deposition," *J. Mater. Research* **22** (2007).
- [100] B. S. Allimi, M. Aindow, and S. P. Alpay, "Thickness dependence of electronic phase transitions in epitaxial V₂O₃ films on (0001) LiTaO₃," *Appl. Phys. Lett.* **93** (2008).
- [101] J. Brockman *et al.*, "Increased metal-insulator transition temperatures in epitaxial thin films of V₂O₃ prepared in reduced oxygen environments," *Appl. Phys. Lett.* **98** (2011).
- [102] M. Yoshimoto *et al.*, "Atomic-scale formation of ultrasmooth surfaces on sapphire substrates for high-quality thin-film fabrication," *Appl. Phys. Lett.* **67** (1995).
- [103] G. Lee, "Realization of ultrasmooth surface with atomic scale step structure on LiNbO₃ and LiTaO₃ substrates," *Optics Exp.* **10** (2002).
- [104] J. Mendialdua, R. Casanova, and Y. Barbaux, "XPS studies of V₂O₅, V₆O₁₃, VO₂ and V₂O₃," *J. Elec. Spectroscopy* **71** (1995).
- [105] G. A. Sawatzky, and D. Post, "X-ray photoelectron and Auger spectroscopy study of some vanadium oxides," *Phys. Rev. B* **20** (1979).

- [106] R. L. Kurtz, and V. E. Henrich, "Surface electronic structure and chemisorption on corundum transition-metal oxides: V_2O_3 ," *Phys. Rev. B* **28** (1983).
- [107] S. Shin *et al.*, "Vacuum-ultraviolet reflectance and photoemission study of the metal-insulator phase transitions in VO_2 , V_6O_{13} , and V_2O_3 ," *Phys. Rev. B* **41** (1990).
- [108] C. D. Wagner *et al.*, "Empirical atomic sensitivity factors for quantitative analysis by electron spectroscopy for chemical analysis," *Surf. and Interface Anal.* **3** (1981).
- [109] T. Katsura, and M. Hasegawa, "Equilibria in the V_2O_3 - VO_2 System at 1600° K," *Bull. Chem. Soc. Jpn* **40** (1967).
- [110] S. Kachi, K. Kosuge, and H. Okinaka, "Metal-Insulator Transition in V_nO_{2n-1} ," *J. Solid State Chem.* **6** (1973).
- [111] B. E. Warren, *X-Ray Diffraction* (Dover Publications, 1969).
- [112] M. Birkholz, P. F. Fewster, and C. Genzel, *Thin Film Analysis By X-Ray Scattering* (Wiley-VCH, 2006).
- [113] P. W. Anderson, "Absence of Diffusion in Certain Random Lattices," *Phys. Rev.* **109** (1958).
- [114] T. M. Rice, and W. F. Brinkman, "Effects of Impurities on the Metal-Insulator Transition," *Phys. Rev. B* **5** (1972).
- [115] B. S. Allimi *et al.*, "Resistivity of V_2O_3 thin films deposited on a-plane (110) and c-plane (001) sapphire by pulsed laser deposition," *Appl. Phys. Lett.* **92** (2008).
- [116] Y. Taketa *et al.*, "New oscillation phenomena in VO_2 crystals," *Appl. Phys. Lett.* **27** (1975).
- [117] B. Fisher, "Voltage oscillations in switching VO_2 needles," *J. Appl. Phys.* **49** (1978).
- [118] J. Sakai, "High-efficiency voltage oscillation in VO_2 planer-journal article junctions with infinite negative differential resistance," *J. Appl. Phys.* **103** (2008).
- [119] Y. W. Lee *et al.*, "Metal-insulator transition-induced electrical oscillation in vanadium dioxide thin film," *Appl. Phys. Lett.* **92** (2008).
- [120] H.-T. Kim *et al.*, "Electrical oscillations induced by the metal-insulator transition in VO_2 ," *J. Appl. Phys.* **107** (2010).
- [121] J. C. Duchene *et al.*, "Filamentary Conduction in VO_2 Coplanar Thin-Film Devices," *Appl. Phys. Lett.* **19** (1971).

- [122] J. Sakai, and M. Kurisu, "Effect of pressure on the electric-field-induced resistance switching of VO₂ planar-type junctions," *Phys. Rev. B* **78** (2008).
- [123] G. V. Samsonov, *The Oxide Handbook* (IFI/Plenum, New York, 1982).
- [124] L. E. Wenger, and P. H. Keesom, "Low temperature specific heat of (V_{1-x}Cr_x)₂O₃ and (V_{1-x}Al_x)₂O₃," *Phys. Rev. B* **12** (1975).
- [125] S. Sengupta *et al.*, "Field-effect modulation of conductance in VO₂ nanobeam transistors with HfO₂ as the gate dielectric," *Appl. Phys. Lett.* **99** (2011).

APPENDIX A: LIST OF ABBREVIATIONS

| | |
|--------|---|
| AFM | Atomic Force Microscopy |
| BC-MIT | Band-Width-Controlled MIT |
| CMOS | Complementary Metal-Oxide Semiconductor |
| CT | Charge Transfer |
| DC | Direct Current |
| EXAFS | Extended X-Ray Absorption Fine Structure |
| EELS | Electron Energy Loss Spectroscopy |
| FC-MIT | Filling-Controlled MIT |
| FWHM | Full Width at Half Maximum |
| IBD | Ion Beam Deposition |
| IBE | Ion Beam Etching |
| I-V | Current-Voltage |
| JCPDS | Joint Committee on Powder Diffraction Standards |
| MBE | Molecular Beam Epitaxy |
| MH | Mott-Hubbard |
| MOSFET | Metal-Oxide-Semiconductor Field-Effect Transistor |
| RHEED | Reflection High-Energy Electron Diffraction |
| RBS | Rutherford Backscattering Spectroscopy |
| RMS | Root-Mean-Square |
| RF | Radio-Frequency |
| SEM | Scanning Electron Microscopy |
| SIMS | Secondary Ion Mass Spectrometry |
| TEM | Transmission Electron Microscopy |
| UHV | Ultra-High Vacuum |
| XPS | X-Ray Photoelectron Spectroscopy |
| XRD | X-Ray Diffraction |

APPENDIX B: SAMPLE NUMBER REFERENCE

This section is meant to assist with the location of samples and raw data associated with any of the figures presented in this dissertation. All material, both physical and digital, is stored in Stuart Parkin's laboratory at the IBM Almaden Research Center.

Fig. 3.6 – Finished Device: XT452, XT456

Fig. 3.7 – Electrical Comparison of Device and Film: XT346, XT452

Fig. 3.8 – Yield Issues: XT452

Fig. 4.1 – Typical Resistivity versus Temperature: XT329

Fig. 4.2 – Typical RHEED and AFM: XT329

Fig. 4.3 – TEM: XT344

Fig. 4.4 – XRD Fringes and RLM: XT372

Fig. 4.5 – RBS: XT317, XT379

Fig. 4.6 – XPS: XT530

Fig. 4.7 – Growth Temp Dependence: XT344, XT345, XT346, XT347

Fig. 4.8 – O₂ Pressure Dependence: XT326, XT329, XT331, XT332, XT330, XT346, XT372

Fig. 4.9 – Epitaxy of VO: XT329, XT331

Fig. 4.10 – Transition Temperature vs O₂ Pressure: XT326, XT329, XT332, XT330, XT346, XT372

Fig. 4.11 – V₂O_{3-x} Comparison: XT326, XT329, XT332, XT330, XT346, XT372

Fig. 5.1 – NA-Sapphire versus AN-Sapphire AFM: XT329, XT426,

Fig. 5.2 – NA-Sapphire versus AN-Sapphire RHEED: XT329, XT426, XT388, XT437

Fig. 5.3 – NA-Sapphire versus AN-Sapphire XRD: XT329, XT360, XT361, XT362, XT363, XT388, XT423, XT424, XT425, XT426, XT427

Fig. 5.4 – NA-Sapphire versus AN-Sapphire Resistivities: XT329, XT360, XT362, XT388, XT424, XT426

- Fig. 5.5 – *a*-Plane Sapphire AFM and RHEED: XT316, XT317
- Fig. 5.6ab – *a*-Plane Sapphire O₂ Dependence: XT314, XT315, XT316, XT334, XT335, XT336, XT337
- Fig. 5.6cd – *a*-Plane Sapphire Thickness Dependence: XT350, XT354, XT355, XT356, XT359
- Fig. 5.7 – LiTaO₃ AFM and RHEED: XT418
- Fig. 5.8 – LiTaO₃ and Al₂O₃ RHEED Streak Comparison: XT418, XT437
- Fig. 5.9 – LiTaO₃ Resistivity and XRD Thickness Dependence: XT418, XT419, XT420, XT421, XT422
- Fig. 5.10 – Cr₂O₃ AFM: XT402, XT403, XT404, XT407, XT408, XT409, XT412
- Fig. 5.11 – Cr₂O₃ Roughness: XT402, XT403, XT404, XT407, XT408, XT409, XT412
- Fig. 5.12 – Cr₂O₃ XRD: XT402, XT403, XT404, XT407, XT408, XT409, XT412
- Fig. 5.13 – V₂O₃ on Cr₂O₃ Resistivities: XT410, XT411, XT420, XT425
-
- Fig. 6.1 – Circuit Diagram: XT456_615.0
- Fig. 6.2 – Switching Curves: XT452_609.0
- Fig. 6.3 – Threshold Behavior: XT452_609.0
- Fig. 6.4 – Gap Size Dependence: XT456 Wafer Survey
- Fig. 6.5 – I-V Partition: XT452_609.0
- Fig. 6.6 – Poole-Frenkel Data: XT452_609.0
- Fig. 6.7 – Voltage-Controlled Oscillations 1: XT456_421.1
- Fig. 6.8 – Voltage-Controlled Oscillations 2: XT456_421.1
- Fig. 6.9 – Filamentary Behavior: XT456_416.0
- Fig. 6.10 – High-Speed Data: XT456_609.0
-
- Fig. 7.3 – Poole-Frenkel Fitting: XT456_609.0
- Fig. 7.4 – Current Parameterization: XT456_609.0
- Fig. 7.5 – Heat Dissipation: XT456_609.0
- Fig. 7.7 – Comparison between Model and Experiment: XT456_609.0